PROPERTIES AND APPLICATIONS OF SELF-ASSEMBLED BIOMOLECULES IN NANOSTRUCTURED BIOMIMETIC INTERFACES

By

ANGELINES A. CASTRO FORERO

A DISSERTATION

Submitted to
Michigan State University
in partial fulfillment of the requirements
for the degree of

DOCTOR OF PHILOSOPHY

Chemical Engineering

2011

ABSTRACT

PROPERTIES AND APPLICATIONS OF SELF-ASSEMBLED BIOMOLECULES IN NANOSTRUCTURED BIOMIMETIC INTERFACES

By

ANGELINES A. CASTRO FORERO

Living cells are able to synthesize a wide range of biomolecules whose precisely controlled size, shape, charge, linkage, molecular weight, functional groups, and binding affinity enable self-assembly. These molecular building blocks, including amino acids, carbohydrates, lipids, and nucleic acids, form macromolecular structures whose functional properties often cannot be matched by man-made materials. To harness the advantages of biomolecules in the design of new materials, controlled methods of fabrication are needed. This dissertation focuses on advancing the understanding of the fabrication process of two biomaterials – phospholipids and self-organizing peptides.

Phospholipids, the most abundant components of cell membranes, spontaneously form lipid bilayers in aqueous solutions. Synthetic lipid bilayers in the form of small unilamellar vesicles (SUV) and supported bilayer lipid membranes (sBLM) are widely used to study membrane-mediated processes and to mimic natural membranes in surface-based devices. The two preferred methods to fabricate SUVs are extrusion and sonication. The goal of this study was to evaluate whether the method of SUV fabrication method has any influence on selected key bilayer properties. The results confirmed that the morphology, average size and distribution of SUVs varied with the fabrication method. However, the molecular-scale behavior of the bilayer,

as studied by fluorescence lifetime, anisotropy, and translational diffusion measurements, was independent of the fabrication method.

Some peptides self assemble into biologically important macromolecular structures, and thus represent excellent candidates for bottom-up fabrication of nanostructured biomimetic materials. The objective of this study was to determine whether synthetic analogues of the conductive pili produced by the metal-reducing bacterium *Geobacter sulfurreducens* could be fabricated *in-vitro*. Type IV pili are homopolymers of a pilin subunit (PilA) or pilin that polymerize via hydrophobic interactions to form pili. The resulting synthetic protein nanowires could be potentially used to develop novel nanotechnologies, including nanoelectronic devices. Using genetic engineering and protein expression tools, a method to mass-produce pilA peptides was developed. *In-vitro* assembly of recombinant pilin subunits resulted in the formation of filaments with properties similar to native *G. sulfurreducens* pili, including a similar diameter, tendency to aggregate into tangled bundles, and electrical conductivity. This achievement offers a potential cost-effective method to mass-produce protein nanowires for commercial applications.

Collectively, this research provided important insights into the use of self-assembling biomolecules for bottom-up fabrication of functional and nanostructured biomimetic interfaces. It demonstrated that the liposome preparation method only affects physical properties of the vesicles (average size and distribution) but not the dynamics of rotational and translational diffusion of the bilayers. It also enabled production of recombinant pilin subunits into synthetic nanowires having properties similar to the native pili of *G. sulfurreducens*.

To God, who never forsakes me,

and

To my parents

ACKNOWLEDGEMENTS

Finishing this dissertation would have not been possible without the help and support of many people. To them I would like to convey my gratitude. I would like to thank my advisor Robert Y. Ofoli and co-advisor R. Mark Worden for the opportunity to join their labs and for their help in becoming an independent researcher. I wish to thank Ilsoon Lee for his time and suggestions while serving as a member of my graduate committee.

This dissertation is the result of several collaborative efforts. Therefore, I want to thank the former and current graduate students with whom I worked closely: Aaron Greiner, Monique Lapinski, and Rebecca Steidl. I also want to thank undergraduate students Teresa DeLuca, Ben Kremkow, Rafael Goseer, and Logan Matthews for their help and for sharing the long-standing tradition of ice-cream Friday.

I would like to thank those who helped me with different aspects of my research, Stuart Tessmer and Shannon Demlow for their collaboration with the scanning tunneling microscopy measurements; Alicia Pastor and Carol Flegler for their invaluable help with the electron microscopy techniques; Daniel Jones for training me on the use of mass spectrometry techniques and experimental suggestions; Lee Alexander and William Kittleman for their help with protein expression and purification; Joe Leykam and Sanela Lampa-Pastirk for the research discussions and insights; and Hazel-Ann Hosein for her training and help with the atomic force microscopy.

Special thanks to Gary J. Blanchard for his guidance and support through out my studies. The joy and enthusiasm he has for research was contagious and his upbeat personality made it very enjoyable working with him. I am deeply grateful to Gemma Reguera for her enthusiasm, encouragement, selfless support, and useful advice during my research. Thank you for trusting

me with such an important project, and for the excellent example of a successful woman in science.

Finally, my sincere gratitude goes to my parents, family, and friends for their love, patience, words of encouragement, and prayers during the last couple of years.

TABLE OF CONTENTS

LIST OF TABLES

LIST OF FIGURES

NOMENCLATURE

a	Ronchi ruling stripe periodicity
A	absorbance
A_i	ith pre-exponential factor
D_w	wobbling diffusion coefficient
D	translational diffusion coefficient
$f(t)$	time-dependent post-bleach fluorescence
$I_{II}(t)$	time-dependent light emission intensity polarized parallel to incident beam
$I_{\perp}(t)$	time-dependent light emission intensity polarized perpendicular to incident beam
l	path length of cuvette
m	mobile fraction
$r(0)$	zero time anisotropy
$r(t)$	induced orientational anisotropy
$r(\infty)$	infinite time anisotropy
t	time
τ	fluorescence lifetime
τ_{HR}	reorientation time
θ_0	The semi-angle of the confining cone volume of the chromophore
$[\theta]$	mean residue molar ellipticity

LIST OF ACRONYMS

ATP	adenosine triphosphate
BLM	bilayer lipid membrane
CBD	chitin binding domain
CD	circular dichroism
CFD	constant fraction discriminator
CMC	critical micelle concentration
CP-AFM	conductive probe atomic force microscopy
CV	cyclic voltammetry
DI	deionized
DLS	dynamic light scattering
DOPC	1-palmitoyl-2-hydroxy-*sn*-glycero-3-phosphocholine
DO	dissolved oxygen
DTT	dithiothreitol
EDS	energy dispersive X-ray spectroscopy
EDTA	ethylenediaminetetraacetic acid
FRAPP	fluorescence recovery after pattern photobleaching
GRAVY	grand average of hydropathicity index
HEPES	4-(2-hydroxyethyl)piperazine-1-ethanesulfonic acid
HM	Hagem medium
HOPG	highly oriented pyrolytic graphite
HPLC	high performance liquid chromatography
IMPACT	intein mediated purification with an affinity chitin-binding tag

IPTG	isopropyl-1-thio-D-galactopyranoside
KCl	potassium chloride
LB	Luria Bertani
MALDI	matrix assisted laser desorption ionization
MBP	maltose binding protein
MCP-PMT	microchannel plate photomultiplier tube
$MgSO_4$	magnesium sulfate
MS	mass spectrometry
NaCl	sodium chloride
NBD-PC	1-oleoyl-2-[12-[(7-nitro-2-1,3-benzoxadiazol-4-yl)amino]dodecanoyl]-*sn*-glycero-3-phosphocholine nitro-benzo derivative
NTA	nitrilotriacetic acid
OD	optical density
OG	octyl β-D-glucopyranoside
PCR	polymerase chain reaction
PID	proportional–integral–derivative
PMSF	phenylmethylsulfonyl fluoride
PVDF	polyvinylidene fluoride
QCM	quartz crystal microbalance
SAM	self-assembled monolayer
sBLM	supported bilayer lipid membrane
SDS-PAGE	sodium dodecyl sulfate polyacrylamide gel electrophoresis
SEM	scanning electron microscopy
STM	scanning tunneling microscopy

SUV	small unilamellar vesicles
TAC	time-to-amplitude converter
TBST	Tris-buffered saline solution and Tween 20
TCSPC	time-correlated single photon counting
TEM	transmission electron microscopy
TFA	trifluoroacetic acid
TOF	time of flight

Chapter 1.

INTRODUCTION

1.1. Motivation

Nanotechnology refers to the creation, manipulation and utilization of materials in the submicron range [1, 2]. Even though nanoscale objects have found applications in electronics, materials science and medicine, questions regarding their potential adverse health and environmental effects remain unanswered [2]. An emerging alternative is to look at how nature tackles highly complex problems and apply nature-inspired or biomimetic solutions to nanotechnology applications. The intersection between nanotechnology and biology is sometimes referred to as Bionanotechnology.

The customizable nature of many biological molecules makes them attractive for the manufacturing of nanostructured materials whose properties can be tailored for the desired purpose [3]. Nature uses a relatively small set of molecules to assemble impressive arrays of hierarchical structures with highly specific functions [3, 4]. These nature-derived building blocks include amino acids, carbohydrates, lipids, and nucleic acids [3]. Biological building blocks are synthesized with precise control of sequence, linkage, molecular weight, functionality, size and

shape [5]. In addition, some biomolecules can also self-assemble with nanoscale precision. For example, phospholipids form bilayers with a thickness of 4 to 5 nm and deoxynucleotides polymerize via phosphodiester bonds into DNA strands, with complementary strands using hydrogen bonding to form a double helix with a diameter of 2 nm [5]. These properties cannot easily be duplicated in synthetic materials and still have the added value of enabling sustainable production, biodegradability and low toxicity [6].

On the other hand, nanostructured materials and interfaces can be used as biomimetic model systems to study cellular processes in a controlled and simplified environment void of biological noise. Moreover, such biomimetic interfaces also find applications in biosensor design, drug delivery, and biocatalysis [1, 7]. The key to these applications is the synthesis of the biomaterials, which requires the use of non-disruptive methods that preserve the original biological function, and sufficient understanding of the biomaterial properties so they can be manipulated and further diversified or optimized [3, 5].

1.2. Problem Description

The projects presented in this thesis are focused on two biomaterials: phospholipids and amino acids. Phospholipids have been widely investigated because they readily self-assemble into structures (vesicles, micelles, and bilayers) [5]. Vesicles and bilayers mimic the cell membrane environment and serve as model membranes in the study of cellular processes [8, 9]. In addition, model membranes act as functional elements in a variety of applications including biosensors, drug delivery and screening, and production of biocatalytic interfaces [8, 10]. Amino acids are the building blocks for peptides and proteins. The same set of amino acids is used to build a diverse array of structures including membrane proteins, enzymes and fibrous proteins [4]. Self-organizing peptides and proteins have received attention in recent years because of their

potential for bottom-up fabrication of nanostructured interfaces. In addition, using genetic engineering tools and functionalization, proteins can be tailored to serve specific applications [11].

Inasmuch as the method used to synthesize biomaterials can affect their properties, the first research objective was to evaluate the effect of the method of preparation of small unilamellar vesicles (SUV) on selected bilayer properties. Phospholipids are a class of lipids and the main component of cell membranes [12]. They have a hydrophilic head and two hydrophobic tails. In aqueous solution, most diacyl phospholipids spontaneously form bilayer structures that close themselves into vesicles [12]. The method of lipid dispersion will determine whether the vesicles are unilamellar or multilamellar. When dry lipid is reconstituted in an aqueous solution, multilamellar vesicles (MLV) are usually formed. MLV are onion-like structures of concentric bilayers separated by narrow aqueous channels [13, 14]. Sonication and extrusion are the most common methods to produce small unilamellar vesicles from MLV [13, 15]. Small unilamellar vesicles, also called liposomes, can be used to form supported bilayer lipid membranes (sBLM).

The transition from multilamellar to unilamellar vesicles can be achieved by either sonication or extrusion. Sonication uses acoustic energy, whereas extrusion uses pressure-driven flow through a polycarbonate membrane [13, 16]. It is conceivable that the physical and molecular scale properties of liposomes prepared by the two techniques would be different, making it difficult to directly compare model BLMs reconstituted from sonication and extrusion. In this study, we evaluated how the method of liposome preparation affected the morphology, average size, and size distribution of liposomes. In addition, we studied the rotational and translational diffusion of a tethered chromophore in model membranes reconstituted from vesicles prepared by sonication and extrusion.

The second objective of this research was to exploit the self-organizing properties of some peptides to construct conductive protein nanotubes. Specifically, we focused our investigations on the conductive hair-like protein appendages or pili produced by the metal-reducing bacterium *Geobacter sulfurreducens* [17]. Pili are 5 to 10 nm in diameter, and are proteinaceous appendages anchored in the outer membrane of a wide range of Gram-negative bacteria [18]. Pili are homopolymers of the pilin peptide or PilA, which assemble via hydrophobic interactions to make the pilus filament [19, 20]. The pilus of *G. sulfurreducens* is of special interest for nanotechnology applications because, in addition to its self-assembly capabilities, it is also conductive [17, 21]. The pili of *G. sulfurreducens* function as electrical conduits to transfer metabolically-generated electrons from inside the cell to extracellular electron acceptors such as Fe(III) oxides [17] or other cells in electroactive biofilms [22]. These attractive features, self-assembly and conductivity, make the pili of *G. sulfurreducens* ideal candidates for applications in the design and fabrication of biobased electronic devices.

Key to the application of conductive pili in bioelectronics is a better understanding of how the pilin peptides self-assemble and their mechanism of electron transfer. To accomplish this, we first focused on producing the pilin monomer, or PilA peptide, in sufficient quantities to enable investigation of its assembly. Current methods of pilin production are based on shearing pili filaments from the outer surface of living cells, removal of non-pili outer surface proteins, and depolymerization of the pili into pilins [23]. Production of pilins directly from *Geobacter* cells is a challenging process because it is time consuming, the efficiency is low, and reproducibility of the protocols is difficult. The pilin subunits are also highly hydrophobic, which greatly complicates their depolymerization from the pili [23]. However, the proteinaceous nature of the PilA peptides makes them potentially amenable to genetic engineering. Furthermore,

recombinant protein expression techniques could be used to mass-produce the PilA peptide in heterologous hosts. We hypothesized that a combination of genetic engineering and recombinant expression approaches would enable the production of large quantities of PilA monomers in a controlled environment, thus eliminating the interference of other proteins from *Geobacter* cell envelope.

We investigated several strategies to produce *G. sulfurreducens* pilins as soluble proteins. The native PilA peptide is very hydrophobic, which makes their expression in soluble form challenging. Thus, step-wise reductions in the hydrophobic amino acids at the N-terminus were carried out to prepare truncated versions of the peptide that retained the redox-active amino acids (at the C-terminus). The solubility of the recombinant peptides was increased by engineering *Escherichia coli* strains that express the truncated peptides fused to soluble proteins. These expression systems were also selected to enable the purification and cleavage of the peptide from its carrier protein. Several expression systems, purification, and cleavage conditions were investigated and optimized. The most efficient system that enabled the mass production of pilin peptides carrying the shortest truncation was selected. Prior to developing various assembly strategies, the secondary structure of the recombinant pilin was characterized to confirm that their native structure had been retained, since this is required for self-assembly, Specifically, we studied the *in-vitro* assembly of recombinant pilins in solution and interfaced them with solid substrates.

The results presented here are stepping stones towards using lipid bilayers and self-assembled peptides and proteins as materials for nanotechnology applications. Important questions regarding the methods used to fabricate these biomaterials have been addressed. We have established that the two common methods used to prepare liposomes, sonication and

extrusion, only affect the physical properties of the bilayers (average size and size distribution). The dynamics of rotational and translational diffusion of bilayers are not influenced by the manner in which they were prepared. Consequently, the extensive body of work reported in the literature regarding bilayer diffusion can be directly compared regardless which of the two methods of liposome preparation was used.

We have also developed a method for the mass production of pilin monomers from *G. sulfurreducens*. Using genetic engineering and recombinant protein expression, a soluble truncated version of the pilin peptide PilA was produced. The recombinant pilins were assembled into pili-like filaments that retained their conductive properties. Various strategies for interfacing recombinant pilins and pili with gold substrates were also investigated. Findings from these studies provide novel insights into their biological assembly and their mechanism of conductivity. Furthermore, the possibility of mass-producing and self-assembling recombinant pilins into conductive protein nanotubes is critical for the development of nanostructured interfaces using a bottom-up fabrication approach. In the long term, *in vitro*-assembled pili can be integrated with other redox-active components of *G. sulfurreducens* such as cytochromes to develop biomimetic interfaces. Such interfaces can facilitate the study of the bacterium's complex electron transfer machinery for applications in bioenergy and bioremediation.

1.3. Background

1.3.1. Model Lipid Membranes: Liposomes and Supported Bilayer Lipid Membranes

Cell membranes, which consist of a lipid bilayer containing proteins and other biological species, serve as a boundary between cells and intracellular organelles [24, 25]. Lipids present in biological membranes are usually amphipathic. The hydrophobic moieties form the membrane

core, and the polar head groups interact with the surrounding water. Proteins can be associated with the membrane through electrostatic interactions, or embedded to various degrees in the hydrophobic core of the membrane [26]. Cell membranes provide the surface or interface where many biological reactions and processes take place. They participate in (1) exclusion of toxins and certain molecules from the cell, (2) accumulation of nutrients, (3) energy transduction, (4) cell locomotion, (5) reproduction, (6) signal transduction, and (7) interactions with other cells [24, 26].

Synthetic organic membranes can be used as models to mimic biological membranes in a controlled environment [25, 27]. They have been used to study membrane-mediated processes and to investigate properties and functions of membrane proteins [10]. They are very promising for applications such as diagnostic devices, biosensors, and drug delivery [28]. Vesicles, also known as liposomes, and supported bilayer lipid membranes (sBLMs) are two model systems of biological membranes [8, 29].

Phospholipids are the most abundant lipids in cell membranes. Consequently, they are widely used to prepare model bilayers [25]. When phospholipids are added to aqueous media, they spontaneously form bilayers because their pair of fatty acid chains does not pack well in a micellar structure. Hydration of a phospholipid dry film usually results in formation of multilamellar lipid vesicles (MLVs) [13, 16]. These onion-like structures have concentric bilayers with low volumes of liquid trapped between them [13]. Small unilamellar vesicles (SUVs) can be prepared directly from MLVs by various methods, mainly sonication and extrusion [13, 30]. In sonication, acoustic energy is used to break large multilamellar vesicles into smaller unilamellar ones [16]. The duration of sonication determines the size of the resulting liposome [31]. In extrusion, phospholipids are forced through a polycarbonate membrane.

Extrusion produces liposome populations with lower polydispersities than sonication because the liposome size is determined by the pore size of the membrane used [32].

Supported bilayer lipid membranes (sBMLs) are planar bilayers adsorbed on a suitable solid support [24]. Lipids arranged in a sBLM retain the lateral fluidity observed in living membrane systems. The water layer separating the bilayer from the support provides the lubrication necessary to preserve the lateral fluidity of both lipid leaflets [26]. Supported bilayer lipid membranes are formed essentially by the Langmuir-Blodgett protocols or vesicle fusion. Langmuir-Blodgett techniques deposit each monolayer separately from the liquid-air interface of a trough onto a hydrophilic substrate [24, 33]. Vesicle fusion, first reported by McConnell and coworkers [27, 34], is a simpler and more reproducible one-step way to transform unilamellar vesicles into sBLMs. With this method, vesicles from solution are adsorbed onto a hydrophilic substrate, and then undergo rupture and fusion to form a planar bilayer [27, 34].

1.3.2. Extracellular Electron Transfer in *Geobacter* Bacteria

Members of the *Geobacteraceae* family are anaerobic bacteria that are ubiquitous in subsurface environments [35]. *Geobacter* species gain energy in the form of adenosine triphosphate (ATP) by transferring electrons to extracellular metal while oxidizing organic compounds to CO_2 [36, 37]. Electron acceptors used by these bacteria include soluble metals (e.g. Fe(III) citrate and U(VI)) and insoluble metals (e.g. Fe(III) Mn(IV) oxides) [38]. *Geobacter sulfurreducens* serves as a model for the *Geobacteraceae* because it is available in pure culture, has a sequenced genome and is amenable to genetic manipulation [22, 39].

Geobacter bacteria have attracted interest for their application in bioenergy and bioremediation. Their ability to oxidize aromatic hydrocarbons into environmentally innocuous

CO_2 shows promise for the bioremediation of petroleum contaminants [40, 41]. *Geobacter* bacteria also reductively precipitate metals and radionuclides such as vanadium and uranium, a process that could be harnessed for the environmental restoration of contaminated groundwater and sediments [42-44]. Finally, *Geobacter* can be used to harvest energy as electricity in devices known as microbial fuel cells, which fully oxidize electron donors using only an electrode as electron acceptor and without the addition of electron mediators [41, 45].

1.3.3. *Geobacter* Pili: Structure and Function

G. sulfurreducens produces hair-like proteinaceous filaments called pili (singular: pilus), which emanate from one side of the cell. The pili of *G. sulfurreduces* are classified as type IV, which reflects the conservation of the N-terminal amino acid sequence of the pilin monomer involved in secretion and assembly [17, 46]. Type IV pili are 5 to 10 nm in diameter and can reach several microns in length. They are helical polymers composed mainly of a single peptide subunit known as the pilin (PilA) [17, 20]. Type IV pili are classified together on the basis of common features shared by the pilins subunits. Type IV pilins are usually ~ 150 amino acids-long 15-20 kDa proteins [47, 48]. They comprise a conserved hydrophobic N-terminal region that adopts an α-helical structure and a variable C-terminus. The first 25 residues of the N-terminal region carry a conserved N-terminal segment with an N-methylated phenyalanine in the first position, whereas the variable C-terminus contains a conserved disulphide bond [19, 47]. The *G. sulfurreducens* pilin contains the N-terminus segment and methylated phenalanine characteristic of type IV pilins but is shorter (61 amino acids-long) and lacks the variable C-terminus and disulphide bond [17].

Understanding the mechanism for type IV pilins assembly has proved to be extremely challenging because of the lack of structural data and the large number of proteins involved in

pilus assembly [47]. Crystallization studies have revealed the structures of only two full-length type IV pilin: *Neisseria gonorrhoeae* GC pilin and *Pseudomonas aeroginosa* PAK pilin; and three truncated pilins lacking 28 residues from the hydrophobic N-terminus: PAK pilin, *P. aeruginosa* strain K122-4 pilin and *Vibrio cholerae* TcpA pilin [47]. Structural information of the type IV pilus at atomic resolution is limited due to the thin diameters and smooth surfaces of the filament [47]. To date, structural data of *G. sulfurreducens* pilus and pilin protein are not available. Difficulties in de-polymerizing the filament and the insolubility of the pilin subunits make crystallization and nuclear magnetic resonance (NMR) experiments extremely difficult.

The structural data available have shown that type IV pilins share a similar architecture: the N-terminal end ~ 53 residues which form an extended α-helix, α1; the globular head domain; the αβ-loop located on one side of the globular domain; the anti-parallel β-sheet; and the D-region, which is delineated by conserved cysteines (Figure 1.1) [19, 47]. The assembly of the type IV pilin peptide into a pilus is mediated by interactions between the conserved ~ 53 residues of the N-terminal α-helices of the pilin subunits, which form a hydrophobic helical bundle in the filament core [47, 49].

By contrast, the *Geobacteraceae* pilins are shorter (~ 60 amino acids, ~ 6.5 kDa), narrower in diameter (3-5 nm), and form a distinct phylogenetic line of descent within the bacterial type IV pilins [17]. Homology models of the pilin of *G. sulfurreducens* also show a unique structure among type IV pilins. As shown in Figure 1.1, a structural model of the pilin of *G. sulfurreducens* in reference to the structure of the model pilin from *P. aeruginosa* strain K (or PAK) confirms the presence of the conserved ~ 53 residues N-terminal α-helix and part of the αβ-loop. This conserved hydrophobic helix at the N-terminus controls inner membrane insertion, signal processing and pilin polymerization, and forms the central helical core of the pilus

filament [17, 39]. Therefore, the assembly of *Geobacter* pilins is predicted to be similar to that of other type IV pilins.

The assembly of pilins involves a large number of proteins. At least 10 proteins have been shown to be involved in the assembly of the TcpA pilus of *Vibrio cholerae* and 18 in *P. aeruginosa*. The role of these proteins remains poorly understood [19, 50]. The pilus is polymerized (protrusion) and depolymerized (retraction) using powerful molecular motors that hydrolyze ATP to gain energy for pilin polymerization and depolymerization [19, 51]. Two clusters in the genome of *G. sulfurreducens* are homologous to those encoding components of the pilus apparatus in other Gram-negative bacteria [17]. The first cluster encodes the pilin subunit (PilA), and proteins homologous to PilB (pilin polymerization), PilT (pilus retraction), PilC (cytoplasmic membrane assembly protein), and regulatory proteins modulating pili expression (the PilS sensor and the PilR response regulator) [17]. The second cluster encodes PilQ (the outer membrane pilus secretin), PilP (the PilQ-stabilizing lipoprotein), PilO (pilin glycosylation), and the two assembly proteins PilN and PilM. The gene encoding PilD (prepilin peptidase) is found in an unlinked position in the genome of *G. sulfurreducens* [52].

Regulation of pilin expression and assembly also shares conserved mechanisms with other type IV pili. Pilin expression is under control of the two-component signal transduction system integrated by the PilR (response regulator) and PilS (sensor) proteins [37] whereas pili assembly is growth-regulated [17, 43]. Pili are assembled during growth on insoluble Fe(III) oxides but not on soluble Fe(III) [17]. They are also formed when cells are grown with fumarate as an electron acceptor at suboptimal temperatures (25 ^{o}C), suggesting that suboptimal growth, rather than the presence of Fe(III) oxides, controls the assembly of the pili [17, 45].

The dynamic protrusion and retraction of type IV pili also enables pili-producing cells to translocate on surfaces, a motile behavior termed twitching motility. However, this type of surface motility has never been demonstrated in *G. sulfurreducens* [17]. Furthermore, a mutant in the retraction pilus motor, PilT, had no defect when grown on Fe(III) oxides [17]. Several observations pointed to a possible direct role of *Geobacter* pili in electron transfer to extracellular electron acceptors. First, the pili were required for growth with insoluble Fe(III) and Mn(IV) oxides as sole electron acceptors but not with soluble Fe(III). These results indicated that pili might serve as a conduit between the cell and Fe(III) oxides that are heterogeneously dispersed in the environment [17]. Second, the pili are also required to achieve cell stacking on the anode electrode of microbial fuel cells and maximum power generation [22]. These results indicated that the pili mediate long range electron transfer to extracellular electron acceptors [17] and across anode biofilms [22].

Reguera *et al.* first elucidated the role of *Geobacter* pili in direct electron transfer through conductive measurements [17]. Conductive-probe atomic force microscopy (CP-AFM) was used to probe the conductivity of the pili of *G. sulfurreducens*. Pili and other proteins were mechanically sheared off the outer membrane of *G. sulfurreducens* and deposited on highly ordered pyrolytic graphite (HOPG) [17]. A voltage was applied to the AFM tip to measure the distal conductivity of the proteins in the sample. The pilus filament of *G. sulfurreducens* showed a strong current response to the voltage, whereas non-pilin proteins had no detectable current. The results showed that the pili of *G. sulfurreducens* are highly conductive [17]. This is consistent with the pili being the electrical connection between the cell and the surface of the Fe(III) or Mn(IV) oxides [17].

Recent studies have also provided evidence in support of conductivity along the length of the pili *G. sulfurreducens* [21]. Pili of *G. sulfurreducens* strain KN400 was sheared from the outer surface of living cells and placed between a non-conductive 50 mm gap of two gold electrodes and dried in a desiccator. A control sample was prepared using a KN400 strain where the gene coding the PilA protein was deleted. Networks of wild type pili had a conductivity 10-100 times higher than the control of PilA-deficient mutant or buffer alone. Conductivity was attributed to the pili only because denaturation of cytochromes present in the sample after heat treatment did not affect the results [21]. However, the effect of heat treatment in pili stability and conductivity and the potential doping of the sample with metals released from the denatured cytochromes were never assessed.

1.4. Organization of this Dissertation

1.4.1. Characterization of Liposomes Prepared by Different Techniques: Measurement of Rotational and Translational Diffusion of an Embedded Chromophore

Chapter 2 describes the effect the method of preparation has on selected properties of bilayers. This project was carried out in collaboration with Dr. Gary J. Blanchard, Dr. Monique M. Lapinski (a Ph.D. student in the Department of Chemistry at the time) and Dr. Aaron J. Greiner (a Ph.D. student at the time in the Department of Chemical Engineering and Materials Science at the time). Each of the collaborators made equal contributions to the work, which dealt with the effect of sonication and extrusion on selected properties of reconstituted liposomes and supporter bilayer lipid membranes. Liposome morphology, average size and size distribution were determined by transmission electron microscopy (TEM) and dynamic light scattering (DLS). Fluorescense lifetimes and rotational diffusion coefficients of fluorophores embedded in

liposomes were measured by time-correlated single photon counting (TCSPC). Translational diffusion of sBLMs reconstituted from liposomes was evaluated by fluorescence recovery after pattern photobleaching (FRAPP).

1.4.2. Mass-Production and *In Vitro* Assembly of Protein Nanowires Using Recombinant Pilins From *Geobacter Sulfurreducens*

Chapter 3 describes the heterologous expression of truncated pilins and their assembly into synthetic pili that retained the conductive properties of native pili from *G. sulfurreducens*. This project was done in collaboration with Dr. Gemma Reguera from the Department of Microbiology and Molecular Genetics and her Ph.D. student Rebecca Steidl. Rebecca and I collaborated on the engineering of truncated versions of the pilin peptide. Expression of the recombinant pilin peptide was investigated using the QIAexpressionist system, pMAL system, and IMPACT system. Expression and purification conditions were analyzed using SDS-PAGE, western blot, and MALDI-TOF mass spectrometry. The secondary structure of the recombinant pilin was studied using circular dichroism. The *in-vitro* assembly of truncated pilins was investigated and the resulting fibers imaged by TEM and atomic force microscopy (AFM). Distal conductivity of *in-vitro* pili was assessed using scanning tunneling microscopy (STM). The STM measurements were done in collaboration with Dr. Stuart Tessmer from the Department of Physics and Ph.D student Shannon Demlow from the Department of Electrical and Computer Engineering.

1.4.3. Study of Pilin Modifications to Enable Interfacing with Electrodes

Chapter 4 describes several strategies investigated to interface recombinant pilins with gold electrodes. In one strategy, the effect of interaction of recombinant pilins with a

hydrophobic alkanethiol monolayer was investigated. In another strategy, a cysteine-modified pilin peptide was engineered to facilitate interfacing with gold electrodes. Expression, purification, and assembly of the cysteine-modified monomers were studied. Film thicknesses were measured by ellipsometry. The insulating behavior of monolayers was evaluated using cyclic voltammetry (CV). Real time deposition of cysteine-modified pilins was studied using quartz crystal microbalance (QCM). In-vitro assembly of recombinant pilins was determined by TEM and scanning electron microscopy (SEM).

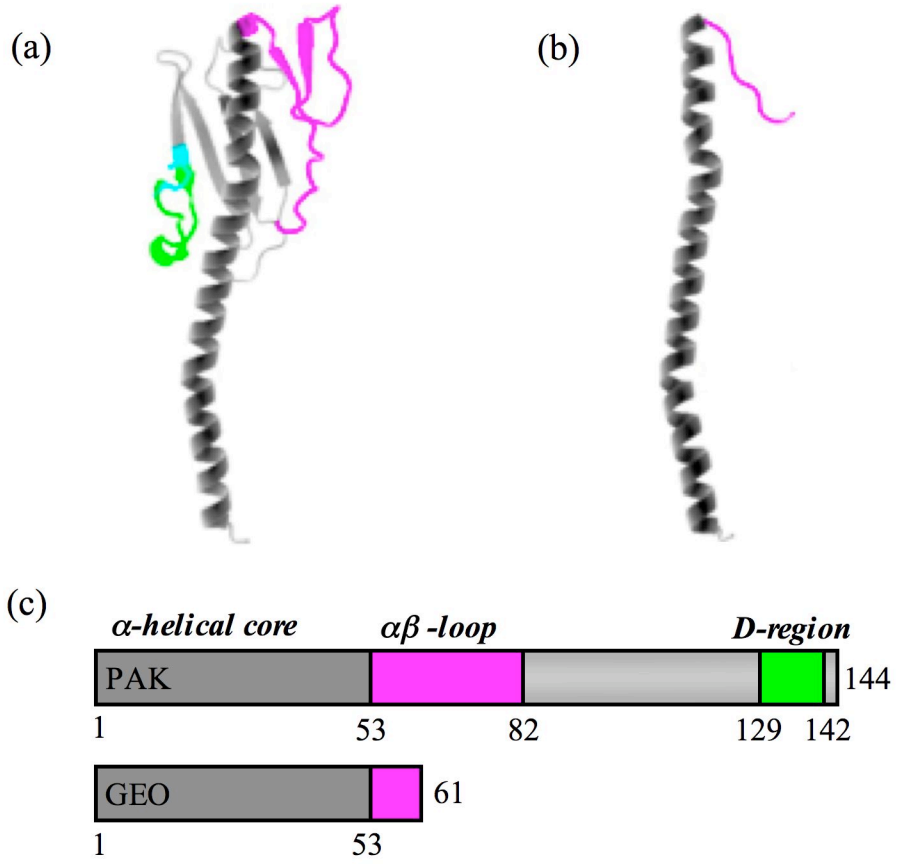

Figure 1.1 Structural comparison of a) *Pseudomonas aeruginosa* PAK pilin and b) *Geobacter* pilin. c) Structural alignment of PAK and Geobacter pilins. The αβ-loop is colored magenta, the D-region is colored green, and the disulphides are colored cyan. The crystal structure of PAK pilin was resolved by Craig *et al.*[49] and is available at the Protein Data Bank. The structure of Geobacter pilin presented here was calculated by a computational model (Gemma Reguera, personal communication, October 7, 2011). For interpretation of the references to color in this and all other figures, the reader is referred to the electronic version of this dissertation.

Chapter 2.

CHARACTERIZATION OF LIPOSOMES PREPARED BY DIFFERENT TECHNIQUES: MEASUREMENT OF ROTATIONAL AND TRANSLATIONAL DIFFUSION OF AN EMBEDDED CHROMOPHORE

2.1. Introduction

Cell membranes comprise a variety of components such as lipids, proteins and carbohydrates embedded into a lipid bilayer. Membranes mediate or participate in various life-sustaining cellular processes such as synthesis of lipids and proteins, energy transference, molecular transport, and enzymatic activity and cell-cell interactions [24, 25]. The use of model systems to emulate the interactions occurring in natural environments is an active area of research. Model bilayers have been used to simplify the study of cell membrane-related functions [10, 53]. Moreover, model bilayers have found applications in electrochemical or optical biosensors, drug screening and delivery, and production of catalytic interfaces [10, 53].

Small unilamellar vesicles (SUV), also known as liposomes, and supported bilayer lipid membranes (sBLM) are two of the most widely used model systems [8, 24]. The two preferred methods for liposome preparation are extrusion and sonication [15]. In extrusion, a lipid suspension is forced through a polycarbonate membrane with a well-defined pore size to produce

vesicles with a characteristic diameter near the pore size of the membrane used in preparing them. The main advantage of extrusion is that it produces liposomes with a reproducible mean vesicle size and narrow size distribution [32]. In sonication, lipid suspensions are mixed using acoustic energy from either a bath or a probe tip sonicator. The induced pressure breaks up the larger multilamellar vesicles in the sample to form smaller unilamellar vesicles. The time over which lipid solutions are sonicated determines the size of the vesicles, with the smallest radius for phospholipid vesicles being in the range of 10.25 ± 0.55 nm, independent of the phospholipid hydrocarbon chain length [54]. Sonication is less time consuming than extrusion, but the mean diameter and size distribution are controlled by the duration of the process, which makes vesicle sizes less reproducible from batch to batch [31, 55].

The objective of this work was to compare small unilamellar vesicles (SUV) prepared by bath sonication and extrusion, to determine if the method of preparation has any effect on selected bilayer properties. This is an important issue because it bears on whether experimental data acquired for bilayer lipid membranes formed by the two methods can be compared directly. We were interested in characterizing the morphology of liposomes, as well as the molecular environment and mesoscopic properties of the lipid bilayers reconstituted from them. Transmission electron microscopy (TEM) was used to study liposome morphology, and to evaluate whether liposomes were unilamellar or multilamellar. The average size and size distribution were determined by dynamic light scattering (DLS). The molecular scale and mesoscopic properties were evaluated by measuring the rotational motion of a chromophore incorporated into the liposomes using time correlated single photon counting (TCSPC). The translational diffusion in a supported planar bilayer formed by liposome fusion was determined by fluorescence recovery after pattern photobleaching (FRAPP). TCSPC experiments were done

in collaboration with Dr. Gary J. Blanchard of the Department of Chemistry.

2.2. Materials and Methods

2.2.1. Preparation of Liposomes by Extrusion

Phospholipids 1,2-dioleoyl-*sn*-glycero-3-phosphocoline (DOPC), 1-oleoyl-2-[12-[(7-nitro-2-1,3-benzoxadiazol-4-yl)amino]dodecanoyl]-*sn*-glycero-3-phosphocoline (18:1-12:0 NBD-PC), and cholesterol were purchased from Avanti Polar Lipids Inc. (Alabaster, AL) and used as received. The composition of the liposomes studied was 1 mM lipid solution containing DOPC and NBD-PC at a ratio 98:2 mol/mol or DOPC/cholesterol/NBD-PC at a ratio 68:30:2 mol/mol/mol. The chloroform solvent was evaporated from the lipid mixture, and the dry film was hydrated using HEPES buffer (Sigma-Aldrich, St. Louis, MO) containing NaCl (Fisher Scientific, Fair Lawn, NJ). The buffer (10 mM HEPES, 150 mM NaCl, pH 7.4) was prepared using purified water from a Milli-Q Plus water purification system (Millipore, Bedford, MA). The mixtures were processed five times through a freeze-thaw-vortex cycle to ensure complete mixing of the sample constituents. Each cycle consisted of immersion in liquid nitrogen for 5 min, followed by immersion in a 60^{o}C water bath for 5 min, and then vortexing the thawed sample for 2 min. After the freeze-thaw-vortex cycles were completed, the solutions were extruded through two 400 nm pore diameter polycarbonate membrane filters using a mini extruder (Avanti Polar Lipids Inc., Alabaster, AL). The pre-extruded suspension was then extruded 11 times through two polycarbonate membranes (Avanti Polar Lipids Inc., Alabaster, AL) with a nominal pore diameter of 100 nm. All extrusions were performed at room temperature.

2.2.2. Preparation of Liposomes by Sonication

Lipid solutions with the same compositions as those used to prepare extruded liposomes were used to form liposomes by sonication. The chloroform-solvated lipid mixtures were dried under nitrogen and placed under vacuum at – 45^{o}C for 3 h. The dried lipid was hydrated in buffer (10 mM HEPES, 150 mM NaCl, pH 7.4) and sonicated for 20 minutes using a bath ultrasonic cleaner (Branson 1510, Branson Ultrasonic Corporation, Danbury, CT). Fresh liposome solutions were prepared prior to every experiment.

2.2.3. Dynamic Light Scattering

The mean diameter and size distributions of liposome mixtures of DOPC/NBD-PC with and without cholesterol were determined by dynamic light scattering (DLS) using a Protein Solutions DynaPro-MS/X system (Wyatt Technology Corporation, Santa Barbara, CA). Liposome solutions were diluted by a factor of 10 with buffer and placed in a polyethylene cuvette for measurement.

2.2.4. Transmission Electron Microscopy

A 10 μL aliquot of each sample was deposited on a Formvar nickel-coated grid and stained with a solution containing 2% uranyl acetate in water. Images were acquired using a transmission electron microscope (TEM, JEOL 100CX, Peabody, MA) operated at an accelerating voltage of 100 kV.

2.2.5. Steady-State Spectroscopy

Steady-state excitation and emission spectra (Figure 2.1) were acquired on vesicle samples for the purpose of characterizing the NBD fluorophore band positions. We used an emission spectrometer (Spex Fluorolog 3, Edinson, NJ) for all measurements, set to a spectral bandpass of 3 nm for both excitation and emission monochromators.

2.2.6. Time Correlated Single Photon Counting

Fluorescence lifetime and rotational diffusion of a tethered NBD chromophore embedded in the liposomes were measured with time correlated single photon counting (TCSPC). The experimental setup for TCSPC has been described in detail elsewhere [56, 57]. A schematic of the TCSPC setup is shown in Figure 2.2. Briefly, it consists of a light source, CW mode-locked Nd:YAG laser (Coherent Antares 76-s, Santa Clara, CA) that produces 1064 nm pulses for 100 ps at a 76 MHz repetition rate. The third harmonic of this light is used to excite a cavity-dumped dye laser (Coherent 702-2, Santa Clara, CA) operated with Stilbene 420 dye (Exciton, Dayton, OH) at 460 nm. The average output of the dye laser is approximately 25 mW, with 5 ps pulses and a 4 MHz repetition rate. The beam is then split into a reference beam and sample beam, which can be frequency-doubled based on the excitation wavelength of the chromophore. The sample beam travels through a set of neutral density filters into a vertical polarizer before reaching the sample. Emitted light is collected at 90^{o} from the incident excitation beam. A Glan-Taylor prism is used to polarize the emitted light 54.7^{o} with respect to the vertical excitation polarization for fluorescence lifetime measurements. Polarizations parallel (0^{o}) and perpendicular (90^{o}) to the vertically polarized incident light are collected for calculating

anisotropy. Sample emission is detected with a microchannel plate photomultiplier tube (MCP-PMT, Hamamatsu R3809U-51, Bridgewater, NJ). The electronics utilized to temporarily resolve the fluorescence transients include a constant fraction discriminator (CFD, Tennelec 454, Oak Ridge, TN) and a time-to-amplitude converter (TAC, Tennelec 864, Oak Ridge, TN). The collection wavelength (545 nm, 10 nm detection bandwith) and polarization were computer controlled using LabVIEW 7.1 code.

2.2.7. Formation of Supported Bilayer Lipid Membranes

The reconstitution of supported bilayer lipid membranes was done by vesicle spreading on fused silica slides. Fused silica microscope slides (75 mm × 25 mm × 1 mm) were purchased from Technical Glass Products, Inc. (Painesville, OH). The substrates were cleaned by bath sonication (Branson 1510, Branson Ultrasonic Corporation, Danbury, CT) in detergent solution for 20 minutes, rinsed with deionized (DI) water, baked at 160^{O}C for 4 h, and plasma treated (Harrick Plasma, Ithaca, NY) with oxygen under vacuum (200 mTorr) for 10 min immediately before bilayer deposition. Supported bilayers were deposited in a custom-made flow cell described elsewhere [58]. The flow cell was initially washed with buffer, followed by 1 h incubation with liposome solution and a final buffer wash to remove any unadsorbed liposomes. All experiments were carried out at room temperature.

2.2.8. Fluorescence Recovery After Pattern Photobleaching

This technique, created by Smith and McConell [59], measures translational mobility of fluorescently labeled lipids or proteins in natural or model supported lipid membranes [60, 61]. An image of alternating bright and dark stripes is projected onto the sample by passing an

expanded laser beam through a Ronchi ruling. A periodic variation of fluorescence intensity as a function of space is created after permanent photobleaching of the fluorescent molecules [59]. Monitoring the subsequent fluorescence recovery provides a measure of lateral transport (diffusion) of unbleached fluorophores into the bleached area [60, 62].

The experimental setup used to perform FRAPP has been described elsewhere and is illustrated in Figure 2.3 [58]. Briefly, it consists of a custom made 1 mL flow cell attached to a double syringe pump (Harvard Apparatus 551382, Holliston, MA), an inverted microscope (Zeiss Axiovert 135M, Carl Zeiss, Thornwood, NY) with a 32X objective lens (Carl Zeiss, Thornwood, NY), an argon ion laser (95, Lexel Laser, Fremont, CA), a side on photomultiplier tube (Hamamatsu R4632, Bridgewater, NJ), a photon counter (SR400, Stanford Research Systems, Sunnyvale, CA), and a fast preamplifier (SR445, Stanford Research Systems, Sunnyvale, CA). The 488 nm laser line was directed through a 5X beam expander (Edmund Optics, Inc. Barrington, NJ). A system of optical flats was used to switch between a low intensity (20 μW) monitoring beam for continuous fluorescence detection and a high intensity (500 mW) beam for photobleaching of fluorophores. A Ronchi ruling (50 lines per inch, Edmund Optics, Inc., Barrington, NJ) placed in the back image plane of the microscope creates a fringe pattern on the sample plane with a periodicity of 25 μm. An aperture placed in the image plane in front of the PMT was used to restrict the observation area and prevent unbleached fluorophores from outside the bleached patterned area from diffusing into the observation region during fluorescence recovery measurements. The illuminated area was 200 μm in diameter, while the observed area was 75 μm.

2.3. Results and Discussion

2.3.1. Liposome Morphology, Mean Diameter, and Size Distribution

Transmission electron microscopy (TEM) images showed that liposomes prepared by bath sonication and extrusion have a unilamellar structure (Figure 2.4). Dynamic light scattering allowed us to determine the average size and size distribution of the liposomes. The mean diameter of liposomes formed by extrusion with or without cholesterol was 112 ± 6 nm (Table 2.1 and Figure 2.5). Thus, cholesterol does not appear to affect the size of liposomes prepared by extrusion. This is not surprising because the size of extruded vesicles should be fairly close to the pore size of the polycarbonate membrane used to prepare them (100 nm). Liposomes prepared by bath sonication had a mean diameter of 28 ± 2 nm without cholesterol and 64 ± 3 nm with cholesterol (Table 2.1), indicating a significant influence of cholesterol on vesicle size. We also observed that liposomes formed by sonication exhibited a bimodal size distribution, with or without cholesterol. Previous reports have shown that liposomes formed by sonication generally have a bimodal distribution [55]. Liposomes formed by extrusion also had a bimodal size distribution that was more pronounced in cholesterol-containing liposomes (Figure 2.5). We were not able to determine if a compositional difference exits between the two populations of cholesterol-containing liposomes. The physical size and distribution information is not necessarily correlated with the molecular scale properties of the bilayer structures.

2.3.2. Fluorescence Lifetimes and Rotational Diffusion in Liposomes

TCSPC permits measurement of time constants from the exponential decay of fluorescent light and the time-resolved orientational anisotropy [63]. Fluorescence lifetime data are related to the local environment experienced by the chromophore [64]. Anisotropy measurements estimate

the confined volume in which a chromophore rotates, as well as the rate of rotation within a volume using a hindered rotor model.

Fluorescence anisotropy decay calculations relate the degree of polarization to the rotational movement of the chromophore. It monitors the time dependence of the transition of a system from a biased to a random orientation [65]. Induced orientational anisotropy *r(t)* is defined as:

$$r(t) = \frac{I_{II}(t) - I_{\perp}(t)}{I_{II}(t) + 2I_{\perp}(t)} \tag{2.1}$$

where $I_{II}(t)$ and $I_{\perp}(t)$ are the emission intensities polarized parallel and perpendicular to the vertically polarized incident excitation pulse, respectively [66, 67].

Kinosita *et al*. and Lipari and Szabo [63, 68] expanded the basic theory of anisotropy decay developed by Wahl to the hindered rotation of fluorophores embedded in membranes [65]. This analysis is known as the hindered rotor model. A fluorophore in solution can assume all possible orientations with equal probability; therefore the infinite-time anisotropy will decay to zero. Since the NBD chromophore was tethered to a lipid in a bilayer lipid membrane, it does not have the structural freedom to fully re-randomize its orientation within its environment following excitation, which gives rise to an infinite time anisotropy [69, 70]. For these systems, the function *r(t)* is given by

$$r(t) = r(\infty) + \left(r(0) - r(\infty)\right)\exp\left(-\frac{t}{\tau_{HR}}\right) \tag{2.2}$$

where $r(\infty)$ is the infinite time anisotropy and *r(0)* is the zero time anisotropy. The value of *r(0)* is determined by the angle between the excited and emitted transition dipole moments of the chromophore, and $r(\infty)$ serves as a gauge for the orientational confinement that the chromophore

experiences. The reorientation time (τ_{HR}) is related to the orientational relaxation of the chromophore within its confined volume, and is approximated by [67]

$$\tau_{HR} = \frac{7\theta_0^2}{24 D_w} \tag{2.3}$$

where D_w is the wobbling or rotational diffusion coefficient. The semi-angle that defines the confined cone volume of the chromophore (θ_0) is related to the zero and infinite time anisotropies by [67]

$$\sqrt{\frac{r(\infty)}{r(0)}} = 0.5\cos\theta_0\left(1+\cos\theta_0\right) \tag{2.4}$$

The liposome systems studied in the present work showed a fluorescent population decay that can be fitted with a two-component exponential mode. The results indicate that NBD experienced at least two environments that do not exchange populations on the time scale of the excited-state relaxation. This behavior has been reported for a chromophore like NBD tethered to phospholipids in a variety of environments. The fluorescence lifetime of NBD is sensitive to the polarity of its immediate environment resulting in a shorter lifetime for NBD chromophores residing in a more polar environment, closer to the polar phospholipid headgroup [71-73]. It has been reported for NBD chromophores attached to an acyl chain that the chromophore can "loop back" to position itself closer to the polar head group of the phospholipids [72].

The observation of two fluorescence lifetimes suggests that the fluorophore existed in two discrete populations during the timescale of the measurement. The proposed environments for NBD are only separated by a few angstroms. However our results showed a difference of more than 4.5 ns between the two fluorescence lifetimes measured, which is consistent with the fluorophore existing in a dielectric gradient that changes substantially over the length scale of the

fluorophore itself. It has been reported that the fluorescence lifetimes of identical molecules can be affected by variations in the local dielectric environment around the molecule [64]. For that reason, we interpreted our results to mean that the fluorophore effectively existed in only one population and experienced one fluorescence lifetime. Since two fluorescence lifetimes were measured experimentally, this is an indication that the fluorophore experienced a dielectric gradient.

The two fluorescent lifetimes were essentially the same for all vesicle systems examined, with $\tau_1 \approx 2$ ns and $\tau_2 \approx 6$ ns (Table 2.2). We note that the relative contributions of the two lifetime components depend to some degree on vesicle composition for the sonicated vesicles (0.05 in the absence of cholesterol versus 0.3 with cholesterol, as opposed to 0.3 for both extruded vesicles; Table 2.2). This likely led to the large differences in the ratio of pre-exponential factors [$A_1/(A_1 + A_2)$ and $A_2/(A_1 + A_2)$] obtained for sonicated vesicles, particularly in the absence of cholesterol. However, owing to the structural complexity of these vesicles and the comparatively limited information contained in the lifetime data, it would be speculative to suggest that either the structure of the vesicle or the positional distribution of the NBD chromophores accounts for the observed differences in pre-exponential factors.

Using the hindered rotor model, we determined the reorientation time (τ_{HR}), the cone angle (θ_0), and the wobbling diffusion coefficient (D_w). The cone angles were the same within experimental uncertainty, regardless of the method of liposome preparation. We noticed that liposomes containing cholesterol, either extruded or sonicated, have a cone angle smaller than liposomes without (~ 40^o versus ~ 60^o). These results are in agreement with previous observations that addition of cholesterol decreases bilayer fluidity [74]. Our data point to a

slightly longer reorientation time (τ_{HR}) and a more restricted volume (θ_0) for the cholesterol-containing system. From these data, we found D_w to be the same for extruded and sonicated lipid bilayers: $D_w \approx 100$ MHz for liposomes without cholesterol and $D_w \approx 45$ MHz with cholesterol. It is interesting to note that there is an apparent difference in τ_{HR} for the cholesterol-containing liposomes. This difference in time constants, while suggestive of a different environment formed by the two methods, cannot be taken simply at face value. The observed time constant is related to both the confining cone angle and the "wobbling" diffusion coefficient, D_w. The cone angles recovered for these two liposomes are the same within experimental uncertainty, and when the fundamental quantity D_w is extracted from the θ_0 and τ_{HR} data, we find that there is no statistically discernible difference for liposomes formed by extrusion versus those by sonication.

It is also important to emphasize that, in all of the anisotropy data, we do not find any measurable differences between the molecular environments of the liposomes formed by extrusion and sonication. While there is a slight difference in the fast component of the NBD fluorescence lifetime for sonicated versus extruded liposomes containing cholesterol, this finding is not reflected in the anisotropy decay dynamics, which are arguably a more sensitive probe of the local environment of the chromophore.

2.3.3. Translational Diffusion in Supported Bilayer Lipid Membranes

Supported bilayer lipid membranes (sBLM) were reconstituted through vesicle adsorption and fusion onto fused silica substrates. A representative fluorescence recovery plot of a DOPC supported bilayer containing NBD-PC as a probe molecule is shown in Figure 2.6. The

translational diffusion coefficients and mobile fractions of fluorophores in sBLMs can be extracted from the recovery data by using the model developed by Starr and Thompson [75]

$$f(t) = f(0) + \frac{m}{2}\left[1 - f(0)\right]\left\{1 - \left(\frac{8}{\pi^2}\right)\exp\left(-\frac{4\pi^2 Dt}{a^2}\right) + \frac{1}{9}\exp\left(-\frac{36\pi^2 Dt}{a^2}\right)\right\} \qquad (2.5)$$

where *f(t)* is the time-dependent post-bleach fluorescence ($t > 0$) normalized with respect to the pre-bleach fluorescence ($t < 0$), with $t = 0$ being the time of the bleach pulse, D the translational diffusion coefficient of the chromophore within the bleached area, m the mobile fraction, and a the stripe periodicity of the Ronchi ruling. This equation assumes one mobile species (fluorophores diffusing in the fluid sBLM) and one immobile species (fluorophores confined in intact, unruptured vesicles adsorbed to the surface). The data were fit with a Levenberg-Marquardt algorithm for non-linear least squares using OriginPro 7.5 software (OriginLab Corporation, Northampton MA).

The data were fit to equation 2.5, and the values for the diffusion coefficient and mobile fraction were determined (Table 2.4). Results indicate that D and m are the same for a given supported bilayer composition, and independent of the method of liposome preparation. Therefore, the differences in the size of liposomes formed by sonication and extrusion do not affect the fluidity of the resulting sBLM. These results are in agreement with a previous quartz crystal microbalance (QCM) study showing that liposomes ranging in size from 25 to 200 nm can form viable bilayer lipid membranes [12]. As expected, the presence of cholesterol in the bilayer served to make the chromophore less mobile (i.e., the BLM is less fluid). This result is fully consistent with the anisotropy decay data presented earlier, as well as previous findings that addition of cholesterol to a phospholipid bilayer decreases the translational diffusion of the phospholipids [76].

2.4. Conclusions

This project focused on comparing selected properties of liposomes prepared by bath sonication and extrusion. The results demonstrated that, while the mean diameter and size distributions of the liposomes depended on the manner by which they were prepared, their molecular and nanoscale organization, studied through fluorescence lifetime, anisotropy decay, and translational diffusion measurements, are independent of the method of preparation. Liposomes formed by the two schemes were characterized in solution and in supported bilayer lipid membranes formed by liposome fusion on a fused silica substrate. The effect of cholesterol on the properties of the liposomes and sBLM was also evaluated. The findings indicate that whether liposomes are formed by sonication or extrusion does not affect the molecular scale organization of these systems. The molecular scale organization of the bilayers is determined by interactions between the constituent species, which themselves do not depend on the manner in which the bilayer is formed. Consequently, all other factors being equal, data on bilayer systems formed by sonication can in fact be compared directly to those on systems formed by extrusion.

Table 2.1 DLS results for extruded and sonicated liposomes for two systems: (1) 98 mol% DOPC and 2 mol% NBD-PC and (2) 68 mol % DOPC, 30 mol% cholesterol, and 2 mol% NBD-PC. Data are means ± SD of three samples.[a]

Composition	Mean diameter extruded vesicles (nm)	Mean diameter sonicated vesicles (nm)
(1) DOPC/NBD-PC	112 ± 6	28 ± 2 and 196 ± 10
(2) DOPC/Cholesterol/NBD-PC	112 ± 6 and 600 ± 30	64 ± 3 and 259 ± 13

[a] Uncertainties in the data are estimated to be ± 5% of the average values.

Table 2.2 Ratio of pre-exponential factors (A_i) and fluorescence lifetimes (τ_i) of NBD-PC fluorophores in sonicated and extruded liposomes comprising (1) 98 mol% DOPC and 2 mol% NBD-PC and (2) 68 mol % DOPC, 30 mol% cholesterol, and 2 mol% NBD-PC.[a] Data represent means ± SD of three liposome solutions.

Composition	$A_1/(A_1 + A_2)$	τ_1 (ns)	$A_2/(A_1 + A_2)$	τ_2 (ns)
(1) Extruded DOPC/NBD-PC	0.44 ± 0.02	1.85 ± 0.10	0.56 ± 0.02	6.01 ± 0.06
1) Sonicated DOPC/NBD-PC	0.06 ± 0.01	1.93 ± 0.26	0.94 ± 0.01	6.10 ± 0.07
(2) Extruded DOPC/Chol/NBD-PC	0.27 ± 0.01	1.67 ± 0.09	0.73 ± 0.01	6.04 ± 0.08
(2) Sonicated DOPC/Chol/NBD-PC	0.31 ± 0.03	2.30 ± 0.18	0.69 ± 0.03	5.91 ± 0.10

[a] Lifetime data are best fit results for the function $f(t) = A_1 \exp(-t/\tau_1) + A_2 \exp(-t/\tau_2)$.

Table 2.3 Reorientation times (τ_{OR}), cone angles (θ_0), and wobbling diffusion coefficients (D_W) of NBD-PC fluorophores in sonicated and extruded liposomes comprising (1) 98 mol% DOPC and 2 mol% NBD-PC and (2) 68 mol % DOPC, 30 mol% cholesterol, and 2 mol% NBD-PC. Data represent means ± SD of three liposome solutions.

Composition	τ_{OR} (ns)	θ_0 (^{o})	D_W (MHz)
(1) Extruded DOPC/NBD-PC	3.03 ± 0.22	62 ± 5	113 ± 27
1) Sonicated DOPC/NBD-PC	2.94 ± 0.09	57 ± 5	98 ± 21
(2) Extruded DOPC/Chol/NBD-PC	3.59 ± 0.28	42 ± 3	44 ± 10
(2) Sonicated DOPC/Chol/NBD-PC	3.00 ± 0.22	37 ± 2	41 ± 8

Table 2.4 Translational diffusion coefficients (D_L) and mobile fractions for NBD-PC in sBLMs prepared with sonicated and extruded liposomes comprising (1) 98 mol% DOPC and 2 mol% NBD-PC and (2) 68 mol % DOPC, 30 mol% cholesterol, and 2 mol% NBD-PC. Data represent means ± SD of three liposome solutions.[a]

Composition	D_L ($\mu m^2/s$)	Mobile fraction
(1) Extruded DOPC/NBD-PC	2.24 ± 0.25	0.78 ± 0.18
1) Sonicated DOPC/NBD-PC	2.02 ± 0.15	0.81 ± 0.11
(2) Extruded DOPC/Chol/NBD-PC	1.65 ± 0.22	0.73 ± 0.10
(2) Sonicated DOPC/Chol/NBD-PC	1.72 ± 0.04	0.69 ± 0.06

[a] All values are averages over at least three different samples, and uncertainties are standard deviations of the mean.

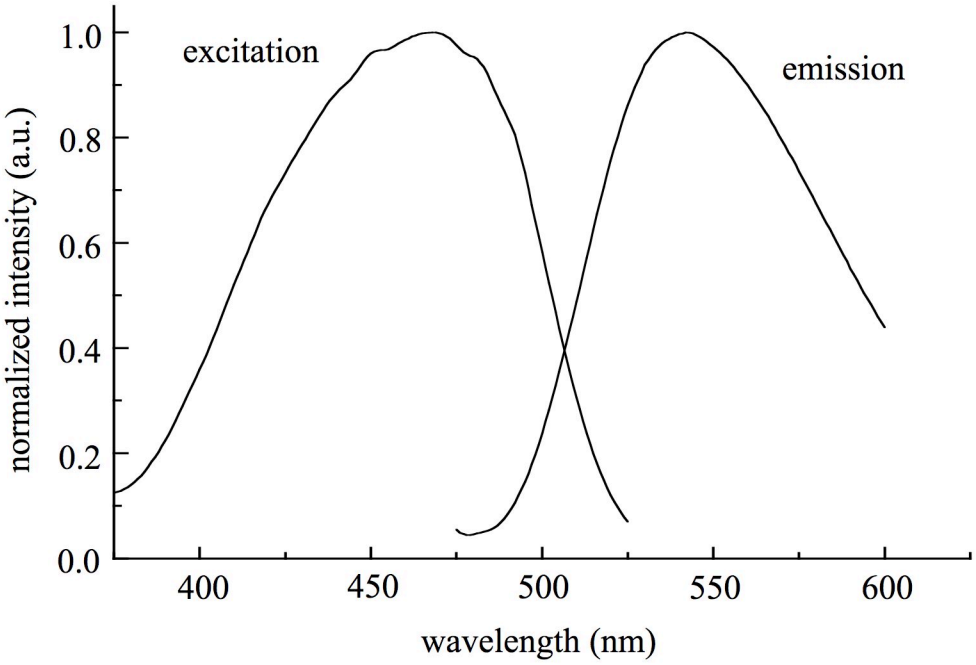

Figure 2.1 Steady-state solution phase absorption and emission spectra of vesicles containing 2% NBD-PC and 98% DOPC. Both spectra have been normalized for clarity of presentation.

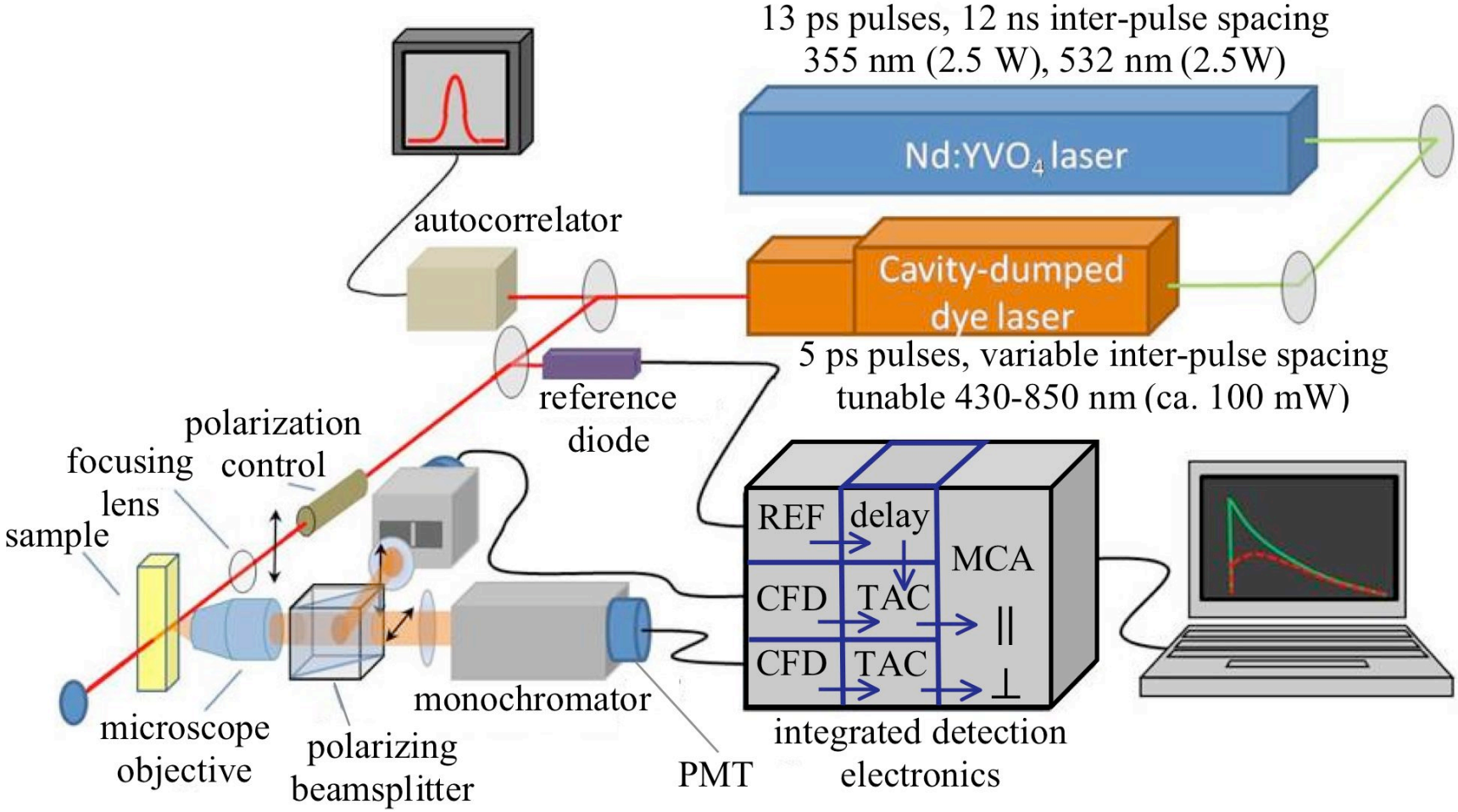

Figure 2.2 Schematics of the experimental setup for time correlated single photon counting (TCSPC).

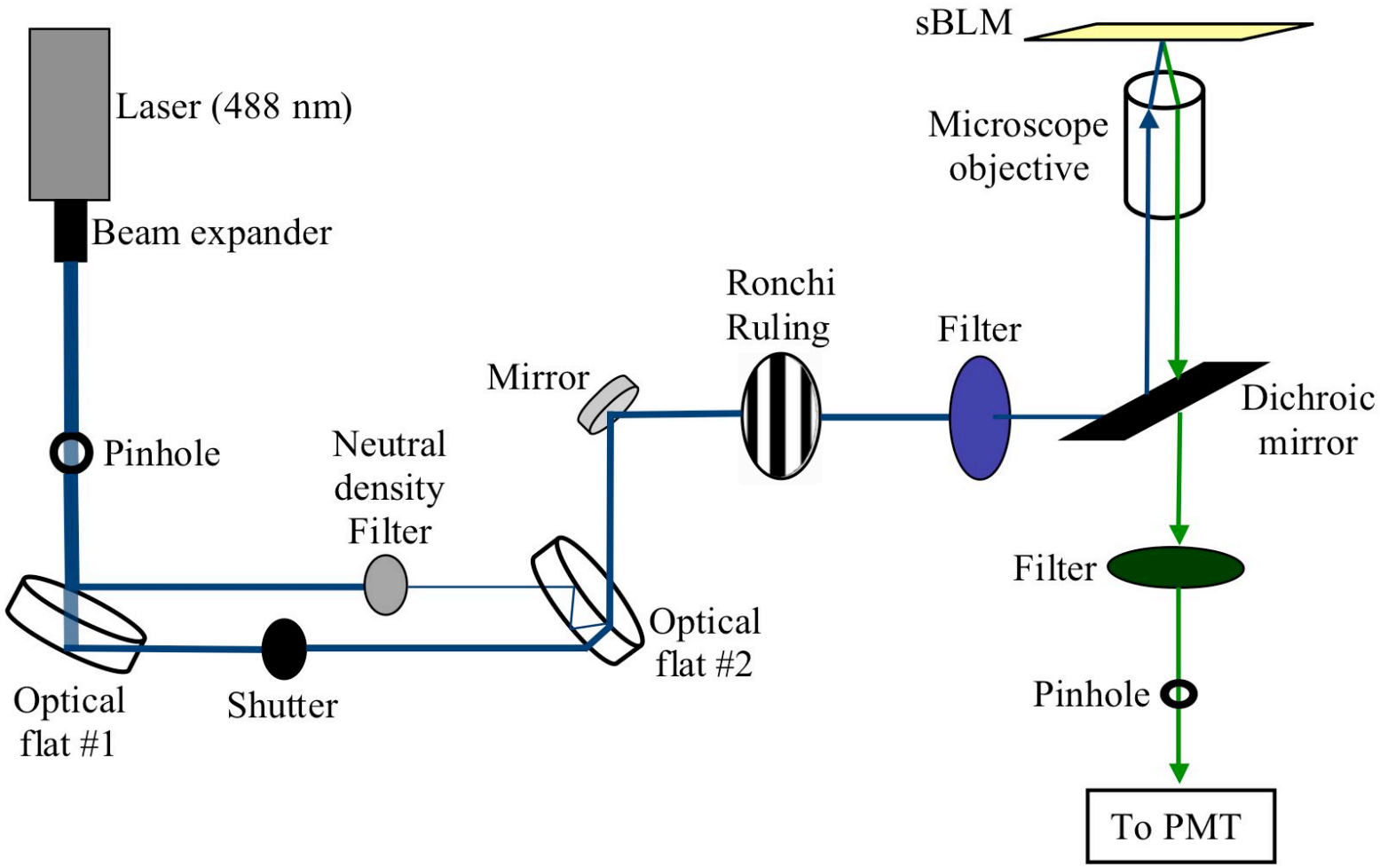

Figure 2.3 Schematics of the experimental set-up for fluorescence recovery after pattern photobleaching (FRAPP).

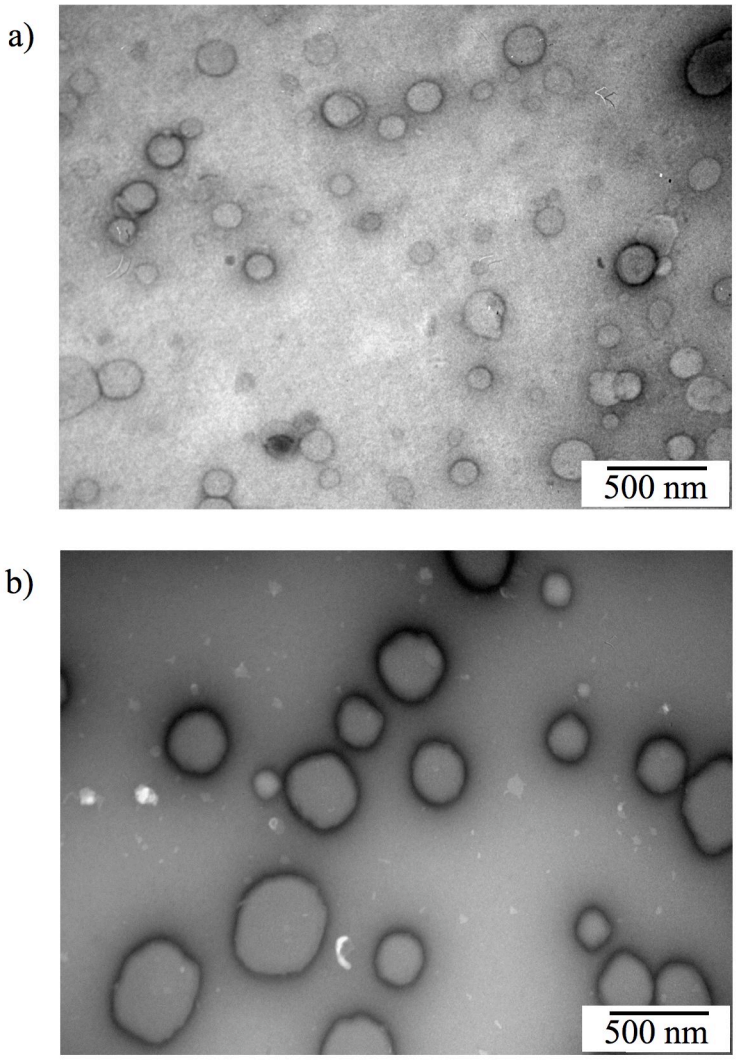

Figure 2.4 Transmission electron microscopy images of liposomes formed by extrusion and sonication: a) TEM image of extruded vesicles without cholesterol; b) TEM image of sonicated vesicles without cholesterol.

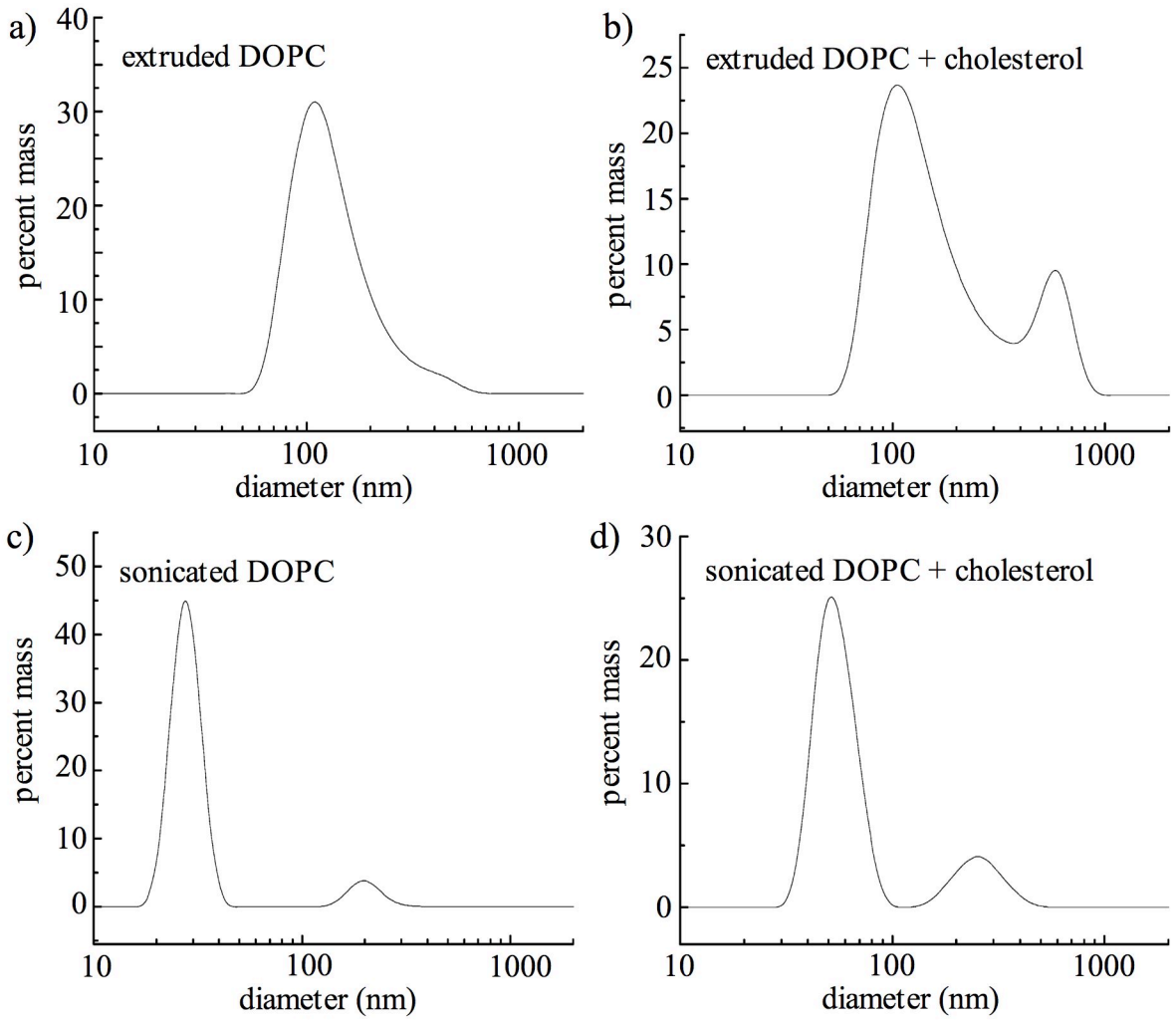

Figure 2.5 Size distribution obtained by dynamic light scattering showing diameters of liposomes as a function of method of preparation and lipid composition: a) extruded DOPC liposomes, b) extruded liposomes containing DOPC and cholesterol, c) sonicated DOPC liposomes, and d) sonicated liposomes containing DOPC and cholesterol.

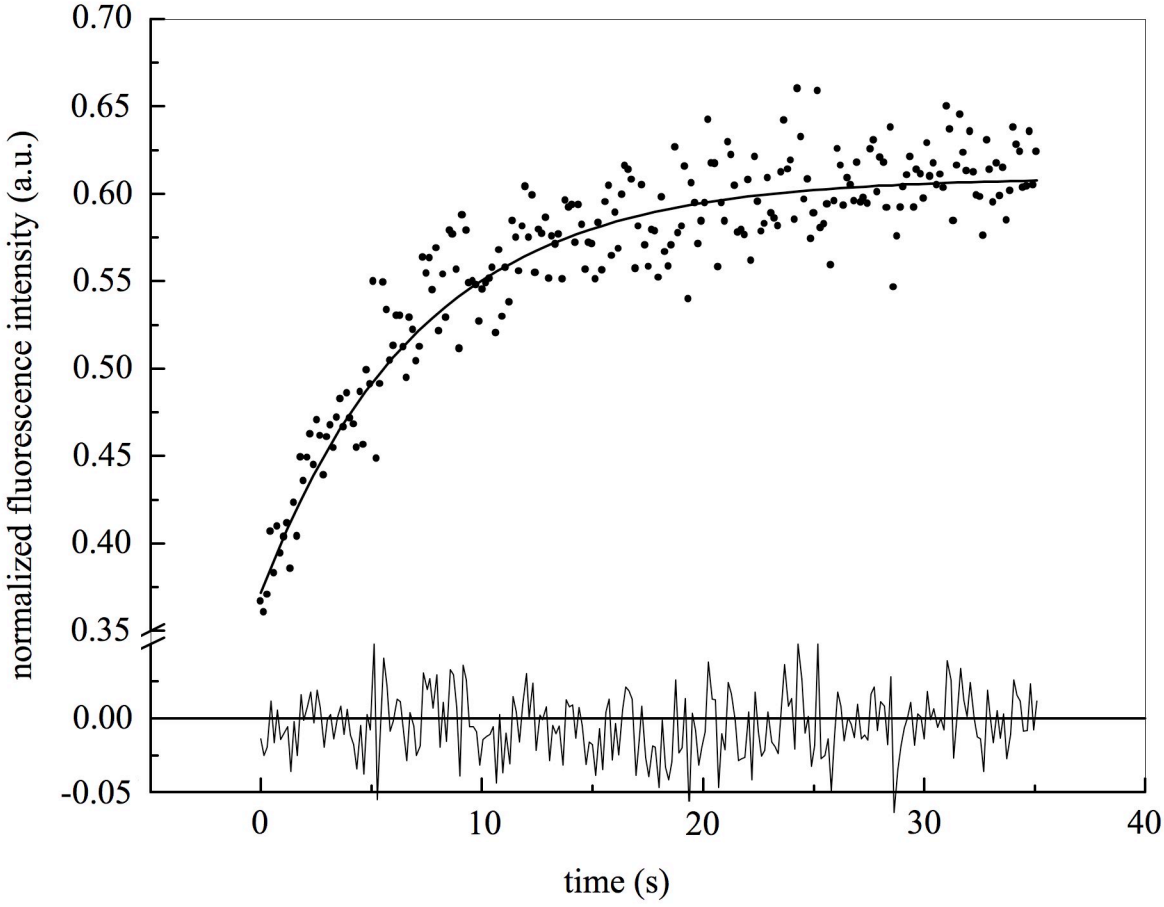

Figure 2.6 Representative FRAPP recovery curve and residual plot (below) for DOPC/NBD-PC supported bilayer lipid membranes reconstituted from extruded liposomes. Similar recovery curves were obtained for bilayer lipid membranes reconstituted from sonicated liposomes. Photobleaching time was 300 ms.

Chapter 3.

MASS-PRODUCTION AND *IN-VITRO* ASSEMBLY OF PROTEIN NANOWIRES USING RECOMBINANT PILINS FROM *GEOBACTER SULFURREDUCENS*

3.1. Introduction

Bionanotechnology is an emerging area of research that applies biological principles or integrates biological components to advance nanotechnology and molecular biology. Biological molecules possess intrinsic characteristics that make them attractive for the fabrication of high performance nanodevices [1, 77]. In particular, proteins, nucleic acids, and phospholipids have precisely-controlled structures, specific functionalities, and capabilities for self-assembly [5], and they are all being actively investigated to design new interfaces for biosensors, drug delivery, and catalytic applications [77, 78].

The protein nanotubes or pili produced by the bacterium *Geobacter sulfurreducens* show promise for the development of nanodevices. Not only do they have self-assembly capabilities but they are also electrically conductive [17]. Although these protein nanowires can be purified from the native organism, yields are low because only a few nanowires are produced per cell and because, even under optimized culturing conditions, these organisms cannot be grown to the high

cell densities often required in industrial settings [23]. Furthermore, culturing the native organism under pili-inducing conditions requires strict anaerobiosis, controlled temperature and specialized culturing vessels, which increases the cost associated with their natural production. These considerations greatly limit practical applications and commercialization of the protein nanowires.

We are interested in studying possible applications of protein nanowires in the development of novel nanostructured devices. This requires the development of cost-effective methods for pili production at high yields. Pili are homopolymers of a pilin subunit (PilA) that self-assemble and disassemble using molecular motors that hydrolyze adenosine triphosphate (ATP) [19, 51]. The first step to integrating pili proteins into nano-devices is to produce pilin monomers in an efficient, reproducible, and controlled manner.

Audette *et al.* successfully expressed recombinant pilin subunits from *Pseudomonas aeruginosa* strain K122-4 (termed ΔK122-4) by deleting 28 residues from the peptide's highly hydrophobic N-terminus to enhance solubility [79]. The recombinant pilins were expressed in the periplasmic space of *Escherichia coli* as part of a maltose-binding (MBP)-*pilA*(Δ1-28) fusion protein [79]. These studies demonstrated that recombinant protein expression can be used to mass-produce pilins in a controlled environment. However, a similar approach in *Geobacter* is challenging because the nanowire subunits are much more hydrophobic and contain amino acids implicated in electron transfer in the most N-t region (e.g., a tyrosine in position 27)[1]. Such long truncations are also challenging because they can affect the natural self-assembly process and generate pilus fibers with structural and functional differences compared to the native ones.

The truncated K122-4 pilin subunit aggregated into soluble high molecular weight structures in the presence of alkyl thiol molecules, and chromatography resins such as Superdex.

[1] Gemma Reguera, personal communication, October 7, 2011.

Transmission electron microscopy (TEM) showed that the aggregates formed hair-like structures similar to pili. Modeling of wild type IV pili and recombinant ΔK122-4 pili predicted the outer diameter (~ 60 Å) to be similar. However, the recombinant ΔK122-4 pili had a wider inner channel (~ 20 Å), which can affect the structural integrity of the protein nanotubes. The ΔK122-4 pili were also longer than the conventionally purified wild-type *P. aeroginosa* pili, probably because of the lack of pilus assembly machinery *in vitro* versus *in vivo* [48]. Further studies demonstrated that ΔK122-4 protein nanotubes retain certain functionalities of the natural pilus fiber such as the ability to bind to single and double-stranded DNA [80].

The ability to mass-produce biologically active recombinant pili from *G. sulfurreducens* is critical towards advancing their application in the development of biosensors, biocatalysts, and nanoelectronic devices. Based on the previous studies with pilins from *P. aeruginosa*, we hypothesized that recombinant pili from *G. sulfurreducens* could be generated without affecting their conductivity. However, it is challenging to truncate the pilin's N-terminus to the degree required to increase its solubility and recombinant expression while maintaining the amino acids critical for self-assembly and conductivity. Furthermore, recombinant expression prevents post-translational modification of the pilin, which could affect the self-assembly and the conductive properties of the recombinant pili.

In the present study, the expression of recombinant pilin subunits of *G. sulfurreducens* and their *in vitro* assembly were investigated. Because of the low solubility of the full-length pilin, several truncated versions of PilA (termed $PilA_n$) were engineered to enhance solubility. Several systems were tested to optimize expression and purification of pilin monomers. Using this approach, a truncated pilin was mass-produced as a soluble peptide. The secondary structure of the recombinant pilin was investigated using circular dichroism (CD). We also investigated the

effect of addition of surfactants on pilin conformation. Finally, recombinant subunits were assembled into fibers and imaged using transmission electron microscopy (TEM) and atomic force microscopy (AFM.) to assess structural features, and by scanning tunneling microscopy (STM) to investigate their conductive properties.

3.2. Materials and Methods

3.2.1. Recombinant DNA techniques

Production of pilin subunits from *G. sulfurreducens* was investigated using three different expression systems. All of the systems produced a fusion protein by attaching an affinity tag to the *pilA* sequence expressed. The use of these tags simplifies purification and, in some cases, improves solubility. The systems considered were: a) QIAexpressionist^{TM}, which attaches a hexa polyhistidine-tag (6×His-Tag) (Qiagen, Valencia, CA); b) pMAL^{TM} protein fusion and purification system, which attaches a maltose binding protein (MBP) tag (New England Biolabs Inc., Ipswich, MA); and c) Intein-mediated purification system, which attaches a chitin binding domain (IMPACT^{TM}, New England Biolabs Inc., Ipswich, MA).

Due to the low aqueous solubility of the pilin monomer (PilA), truncated versions of PilA (termed $PilA_n$, were n is the number of amino acids removed from the hydrophobic N-terminus) were engineered to enhance solubility. The truncated pilin gene was extracted from the genomic DNA of *G. sulfurreducens.* PCR amplification (30 cycles, 30 s at 95^{o}C, 20 s at 50.7^{o}C, and 1 min at 72^{o}C) was performed using 100 ng genomic DNA and Platinum® PCR SuperMix High Fidelity (Invitrogen, Carlsbad, CA). DNA was isolated from a 2% agarose gel using

Zymoclean® Gel DNA Recovery Kit (Zymo Research, Irvine, CA) and ligated in-frame into the expression vector. Table 3.1 shows the primers used to amplify the DNA and the restriction sites used to clone the $pilA_n$ gene into the expression vectors. Plasmids were then transformed into DH5α *E. coli* cells for propagation. The recombinant plasmids were confirmed by digestion and sequencing.

3.2.2. Expression of Recombinant Pilins

Expression plasmids were transformed into competent *Escherichia coli* host cells (see Table 3.2) for expression. To test expression and optimize growth conditions of recombinant proteins, small-scale shake-flask experiments (~ 50 mL cultures) were carried out using Luria-Bertani (LB) media. Glucose at a concentration of 2 g/L was added to LB media when using vectors from the p-MAL expression system to repress the maltose genes on the chromosome of the *E. coli* cells. Antibiotics were added where appropriate to the following final concentrations: ampicillin (Amp), 100 μg/mL; chloramphenicol (Cam), 34 μg/mL; kanamycin (Kan), 50 μg/mL. In general, cells were grown at 37^{o}C and 200 rpm and induced with isopropyl-1-thio-D-galactopyranoside (IPTG) when OD_{600} was between 0.4 and 0.6. After induction, the temperature was lowered to 30^{o}C. Cells were harvested 6 h later by centrifugation at 5000 x g for 20 minutes at 4^{o}C, and the cell pellet was stored at -70^{o}C.

After confirming expression and optimizing conditions, large-scale expression was carried out in a batch reactor. In these experiments, an overnight culture of transformed *E. coli* cells was used to inoculate a fed-batch bioreactor (Bioflo 3000, New Brunswick Scientific, Edison, NJ) containing 5 L yeast-enriched Hagem medium (HM) media plus ampicillin and

chloramphenicol. The HM medium contained 9 g/L potassium phosphate monobasic KH_2PO_4, 6 g/L potassium phosphate dibasic K_2HPO_4, 6 g/L sodium phosphate dibasic Na_2HPO_4, 3 g/L ammonium phosphate dibasic $(NH4)_2HPO_4$, 5 g/L yeast, 1 g/L magnesium sulfate $MgSO_4$, 10 g/L glucose, and 5 mL/L of trace elements [81]. The solution of trace elements contained 10 g/L iron (II) sulfate $FeSO_4$, 2.5 g/L zinc sulfate heptahydrate $ZnSO_4.7H_2O$, 1 g/L manganese sulfate pentahydrate $MnSO_4.5H_2O$, 1 g/L cobalt (II) chloride hexahydrate $CoCl_2.6H_2O$, 1 g/L sodium molybdate dihydrate $Na_2MoO_4.2H_2O$, 0.2 g/L sodium borate decahydrate $Na_2B_4O_7.10H_2O$, and 5 g/L calcium chloride dihydrate $CaCl_2.2H_2O$ dissolved in 5 M hydrochloric acid HCl. Temperature, pH, glucose feeding, and dissolved oxygen were controlled with a PID (proportional–integral–derivative) controller [82]. Cells were grown overnight (~16 to 20 h) at 37^oC. Glucose depletion was indicated by a spike in dissolved oxygen (DO) concentration. A solution containing 50% (w/v) glucose and 20 g/L $MgSO_4$ was fed on demand to replenish depleted glucose. The pH was controlled at 7.0 via automatic addition of concentrated ammonium hydroxide NH_4OH. Dissolved oxygen (DO) was kept at 10% during the fermentation process by increasing agitation speed from 50 to 1000 rpm, then increasing the airflow rate, and finally by controlling the glucose feeding rate. After overnight growth, expression of the recombinant protein was induced with 0.5 mM IPTG, and the temperature was lowered to 30^oC. Six hours after induction, cells were harvested by centrifugation at 5000 x g for 20 minutes at 4^oC. The cell pellet was stored at -70^oC. Expression of the fusion protein was

tested by SDS-PAGE and western blot.

3.2.3. Purification of Recombinant Pilins

Recombinant pilins were purified by affinity chromatography. The type of resin used varied with the expression system. The QIAexpressionist™ system used nickel-nitrilotriacetic acid (Ni-NTA) resin; the pMAL™ system used amylose resin; and the IMPACT™ system used chitin beads. Figure 3.1 shows the purification steps for each system.

In all cases of cytoplasmic expression, harvested cells were resuspended in lysis buffer (10 mL buffer per gram of cells) and lysed using a tip sonicator (Sonifier 250, Branson, Danbury, CT). The composition of all buffers used during purification can be found in Table 3.3. The crude extract was sonicated on ice 7 times for 10 s. Cell extract was clarified by centrifugation at 20,000 x g for 30 min at 4^{o}C. The supernatant was loaded into the affinity column to allow binding of the target protein. Vector p4x from pMAL™ system produced periplasmic expression of the MPB-PilA_n fusion protein. In this case, the harvested cell pellet was subjected to osmotic shock to release periplasmic proteins. The osmotic shock fluid was loaded into the affinity column. After binding, a wash buffer was pumped through the column to remove unwanted proteins that were bound non-specifically to the column. The subsequent steps to recover the target protein varied depending on the purification system used.

For the QIAexpressionist™ system, His-tagged pilin was eluted from the column with a buffer containing 300 mM imidazole. For the pMAL™ system, the MBP-PilA_n fusion was eluted with a buffer containing 10 mM maltose. After elution, the MBP tag was cleaved from the

pilin using Factor Xa protease. For the IMPACT^{TM} system, the PilA_n subunit was cleaved from the chitin-bound intein tag (CBD) by incubating the column with a buffer containing 50 mM dithiothreitol (DTT). Cleavage efficiency was tested at 4^{o}C or 23^{o}C for 24 to 72 h. After cleavage, the pilin subunits were eluted from the column using a storage buffer. Production of pilin subunit was confirmed by SDS-PAGE, and MALDI-TOF mass spectrometry.

3.2.4. Sodium Dodecyl Sulfate-Polyacrylamide Gel Electrophoresis (SDS-PAGE)

Protein expression and cleavage efficiency were evaluated using Tris-glycine (Biorad, Hercules, CA). Cell pellets from 100 to 1000 μL of cell culture were dissolved in a loading buffer (100 mM Tris pH 6.8, 20% glycerol, 8 M urea, 2% (w/v) sodium dodecyl (SDS), 0.02% bromophenol blue). Liquid samples (e.g. cell lysate, osmotic shock fluid, elution fractions) were dissolved in a 1:1 ratio using a loading buffer. Production of pilin was confirmed as bands having the right molecular weight as the pilin peptide appeared on Tris-tricine gels (Biorad, Hercules, CA). Samples for Tris/tricine gels were prepared by dilution with the same volume of Tricine sample buffer ((Biorad, Hercules, CA). Gels were run in a Mini Trans-Blot cell system (Biorad, Hercules, CA). Tris/glycine gels were run using Tris/glycine/SDS buffer (25 mM Tris, 192 mM glycine, 0.1% w/v SDS). Tris/tricine gels were run using Tris/tricine/SDS buffer (100 mM Tris, 100 mM Tricine, 0.1% w/v SDS). The gel running conditions were as follows: 30 min at 200 V for Tris-glycine gels, and 120 min at 100 V for Tris-tricine gels. Gels were stained with Bio-safe Coomassie (Biorad, Hercules, CA) for one hour and de-stained in water until bands were clearly visible. Tricine gels required an additional 30 minutes fixing step with a solution of 50% methanol, 10% acetic acid in water prior to being stained.

3.2.5. Western Blot Analysis

Proteins were transferred from acrylamide gel to a polyvinylidene fluoride (PVDF) membrane (Millipore, Billerica, MA) using a Trans-Blot SD semi-dry transfer cell (Biorad, Hercules, CA). After transfer, the PVDF membrane was blocked with 5% (w/v) non-fat dry milk in Tris buffered saline and tween 20 buffer (TBST, 20 mM Tris pH 7.6, 137 mM NaCl, 0.1% Tween 20) for at least 1 hour at 4^{o}C. The membrane was incubated for 1 hour at 23^{o}C with the primary antibody. After three washes of 5 min each with TBST buffer, the membrane was incubated with the secondary antibody for 1 h at 23^{o}C, and then the TBST washing step was repeated. Proteins were visualized after staining with 3,3',5,5'-tetramethylbenzidine (TMB) (Thermo Scientific Pierce, Rockford, IL). Antibodies were dissolved in blocking solution. Primary antibodies, anti-His and anti-MBP, were used at 1:5000 dilutions (New England Biolabs Inc., Ipswich, MA). Secondary antibody, goat anti-mouse IgG-HRP linked, was used at 1:5000 dilutions (Sigma-Aldrich, St. Louis, MO).

3.2.6. Matrix Assisted Laser Desorption-Ionization-Time of Flight Mass Spectrometry (MALDI-TOF MS)

A 1 μL of sample was mixed with 1 μL of 50 mM 3,5-dimethoxy-4-hydroxycinnamic acid in 50% acetonitrile CH_3CN/0.5% trifluroacetic acid (TFA) and dried on a sample plate. Mass spectra were collected on a time-of-flight (TOF) Voyager-DE Pro-MALDI-TOF (Applied Biosystems, Framingham, MA).

3.2.7. Circular Dichroism (CD)

Circular dichroism (CD) spectra were acquired on a Chirascan^{TM} spectrometer (Applied Photophysics Ltd., Leatherhead, United Kingdom). Spectra were recorded from 190 to 260 nm at 0.5 nm increments and a 5 second integration time using a quartz cuvette with a 0.1 cm path length (Starna Cells Inc., Atascadero, CA), and peptide concentrations ranging from 65 μg/mL to 41 μg/mL. Measurements were performed in 10 mM potassium acetate buffer at pH 3.8 with 50 mM Na_2SO_4 and 10 mM potassium phosphate buffer at pH 7.0 with 50 mM Na_2SO_4. The effect of the detergents sodium dodecyl sulfate (SDS) and octyl β-D-glucopyranoside (OG) on the secondary structure of the pilin monomers was investigated. The spectra were baseline-corrected and smoothed using a third order Savitsky-Golay filter. Spectral data are presented in units of molar ellipticity per residue, [θ]. To convert CD instrument units (θ, millidegrees) into mean residue molar ellipticity [θ] units, the following equation was used [83]:

$$[\theta] = \left(\frac{\theta \times 0.1 \times MRW}{c \times l} \right) \tag{3.1}$$

where c is the peptide concentration in mg/mL, l is the path length of the cuvette in cm, and MRW is the mean residue weight of the sample, calculated by:

$$MRW = \frac{MW}{n-1} \tag{3.2}$$

where MW is the peptide molecular mass in Daltons, and n is the number of amino acid residues (42 for the $PilA_{19}$ monomer).

The peptide concentration was determined from the difference spectrum of the protein dissolved in 6 M guanidine hydrochloride at pH 12.5 versus pH 7.1 [84]. The baseline was

scanned from 320 to 270 nm with 1 mL of the pH 7.1 guanidine solution in the reference compartment and 1 mL of the pH 12.5 guanidine solution in the sample compartment. The same volume of peptide sample was added to each cuvette, and the difference spectrum was obtained and baseline-corrected. The concentration was determined from absorbance at 294 nm using the known amino acid composition of the $PilA_{19}$ subunit and the reported values of the molar extinction coefficients for tyrosine and tryptophan residues [85], using the equation below:

$$c = \frac{A_{293}}{2{,}357Y + 830W} \tag{3.3}$$

where Y is the number of tyrosines and W is the number of tryotophans, which are three and zero, respectively, for the $PilA_{19}$ subunit.

3.2.8. *In-vitro* Assembly of Recombinant Pilins into Pilus Fibers

After purification, recombinant pilin subunits were exchanged from buffer solution to a mixture of 80% acetonitrile and 20% methanol. The exchange of the pilins from buffer to organic solvent was done using the Oasis MAX extraction cartridges, 60 mg sorbent (Waters Corporation, Milford, MA). The column was wetted with 1 mL of 100% acetonitrile, followed by 1 mL wash with DI water. Before loading, the pH of the protein solution was adjusted above 10 with 1 mM NaOH. Approximately 2 mL of buffer containing pilin was passed through the column. The column was washed with 1 mL solution of 5% NH_4OH. The pilin was eluted with 1 mL solution of 20% methanol and 80% acetonitrile. Samples were dried with a SpeedVac concentrator. The dry sample was re-suspended in filtered deionized (DI) water or 10 mM CHES buffer at pH 10.0. The re-suspended sample was imaged by TEM and AFM to confirm the assembly of $PilA_{19}$ subunits into pili.

3.2.9. Transmission Electron Microscopy (TEM)

A 10 μL aliquot of sample was deposited on a Formvar nickel-coated grid, and stained with a solution containing 2% uranyl acetate in water. Images were acquired using a JEOL 1000 CX transmission electron microscope (JEOL, Peabody, MA) operated at an accelerated voltage of 100 kV.

3.2.10. Atomic Force Microscopy (AFM)

Pili fibers were adsorbed on freshly cleaved mica and imaged with a Nanoscope IV Multimode scanning probe microscope (Veeco, Santa Barbara, CA) equipped with a *J* scanner. Images were collected in tapping mode using commercially available silicon or silicon nitrite cantilevers.

3.2.11. Scanning Tunneling Microscopy (STM)

We assessed the conductive properties of the recombinant pili using a table-top Nanosurf EasyScan STM. Members of the research group of our collaborator, Dr. Stuart Tessmer, carried out the STM measurements. This system is described in detail elsewhere [86]. Briefly, the sample was firmly attached to a conductive cylinder that rested on a rail system. The tip was held by a conductive clamp that also served as a tunneling current lead. The sample holder was moved towards the fixed tip via a linear piezo motor. The sample was grounded and the voltage was applied just to the tip. Vibration isolation was implemented by a rubber damping stack that suppresses high frequencies and a single spring suspension stage that suppresses frequencies lower than 50 Hz. The STM was placed inside a plastic glove bag through which a constant flow of dry nitrogen is supplied. Even though this microscope is easy to use and can achieve atomic

level resolution, it has some disadvantages. Mainly, the scan range (500 nm × 500 nm) is small and the high propensity for thermal drift makes the image not reproducible from one scan to the next.

After corroboration of recombinant pili assembly via TEM, a 10 μL drop of the sample was deposited on a freshly cleaved layer of highly oriented pyrolytic graphite (HOPG). The sample was left on the HOPG for at least 30 minutes to allow pili diffusion to and adsorption onto the surface. The HOPG substrate was then rinsed with DI water, and excess moisture was removed using filter paper. STM topography measurements of the recombinant pili were done at room temperature (~ 23^{o}C).

3.3. Results and Discussion

3.3.1. Production of Recombinant Pilins

The high hydrophophicity of the nanowire pilin greatly limits its mass-production in a heterologous host. The pilin's hydrophobicity is illustrated using a Kyte and Doolittle [87] hydropathicity plot (Figure 3.2). This method calculates the average hydropathicity of a moving segment as it advances through the sequence from the amino to the carboxy terminus. It uses a hydropathicity index scale that assigns hydrophobicity values to each amino acid in the protein segment under consideration. Hydrophilic amino acids give negative hydropathicity values, and hydrophobic amino acids give positive values. The plot presented was evaluated using a 19-residue segment algorithm. The Kyte and Doolittle plot confirms the trans-membrane nature of the pili. This method establishes that when the hydropathicity of a given 19-residue segment averages a value greater than 1.6, there is a high probability that this sequence is part of a membrane-bound protein spanning the membrane. This criterion is met up to position 18 of PilA

(red dashed line in Figure 3.2). Figure 3.2 also shows hydropathicity values for the truncations investigated in this project. The GRAVY index is the average hydropathicity score for all the amino acids in a protein, where a positive GRAVY index indicates a protein is hydrophobic, while a negative GRAVY index indicates a protein is hydrophilic [87]. A PilA truncation of 10 amino acids yields a protein having a GRAVY index that is lower than the full length PilA, but is still positive indicating that some hydrophobicity is still present. Other truncations, $PilA_{19}$, $PilA_{20}$, and $PilA_{22}$, have negative indexes indicating a change from a hydrophobic to a hydrophilic nature.

Based on this analysis of pilin hydrophobicity, truncated versions of the full length PilA were genetically engineered to overcome pilin hydrophobicity and improve solubility. Initially a 20-amino-acid truncation of the PilA subunit (named $PilA_{20}$) was selected, and the expression and purification conditions were investigated using the QIAexpressionist (Qiagen, Valencia, CA) expression system. A hexa polyhistidine-tag was attached to the N-terminal $PilA_{20}$ subunit. A 6×His-Tag facilitates purification via (Ni-NTA) metal chromatography but generally does not interfere with the protein's folding and function [88]. The theoretical molecular weight of the 6×His-$PilA_{20}$ is 6,590 Da. Figure 3.3 shows SDS-PAGE and western blot analysis carried out after expression and purification of the 6×His-$PilA_{20}$. Appearance of a band with the right molecular weight as the 6×His-$PilA_{20}$ pilin confirmed the expression of the truncated pilin. However this band appeared in induced as well as non-induced samples, which indicated leaky expression of the recombinant peptide. In addition, several bands with molecular weight larger

than the 6×His-PilA_{20} pilin were observed in the western blot, which suggested that the pilins might be aggregating or self-assembling.

To improve the solubility of the PilA_{20} subunits being expressed, a maltose binding protein (MBP) tag was used. The MBP tag is a large protein secreted by *E. coli* cells that can be expressed at high levels and helps keep proteins attached to either the N- or C- terminus soluble. The MBP also binds strongly to amylase resin, enabling the fusion protein to be purified via affinity chromatography [88]. Recombinant pilin from *P. aeruginosa* [79] was successfully expressed as a MBP-PilA fusion protein. The pMAL^{TM} protein fusion and purification system (New England Biolabs Inc., Ipswich, MA) provide vectors where the cloned gene is inserted down-stream from the malE gene, which encodes the MBP resulting in the expression of an MBP fusion protein. This system offers the flexibility to use either cytoplasmic or periplasmic expression depending on the vector used. The maltose binding protein (MBP) was attached to the hydrophobic N-terminal end of the PilA_{20} subunit. Expression of the MBP-PilA_{20} fusion was attempted both cytoplasmically and periplasmically. Both constructs were transformed into K12 TB1 *E. coli* cells.

Periplasmic expression of a MBP fusion after induction, osmotic shock, and recovery of periplasmic proteins was confirmed by SDS-PAGE and western blot analysis (Figure 3.4). The molecular weight of the fusion protein eluted from the amylase column was determined by MALDI-TOF (see Figure 3.4) to be 43,031.9 Da. This value is smaller than the theoretical value for the periplasmic MBP-PilA_{20} fusion (46,902.6 Da). Certain proteins have been reported to be incompatible with trans-location to the periplasmic space, as evidenced by their degradation during expression. Another possibility is that the intact fusion could have been degraded by

periplasmic proteases [89]. Protease inhibitors and protease deficient *E. coli* strains were used in subsequent experiments without any changes in the outcome.

SDS-PAGE and western blot analysis after cytoplasmic expression confirmed the production of a MBP fusion protein (Figure 3.5). After purification of the fusion, two bands that tested positive against anti-MBP antibody were observed in the elution from the amylose column (Figure 3.5). MALDI-TOF mass spectrum of the elution fraction showed two main peaks. The peak at 47,042.6 Da has a molecular weight consistent with the theoretical molecular weight of the MBP-$PilA_{20}$ fusion produced in the cytoplasm (47,033.9 Da). The peak at 43,671.1 Da is likely the result of proteolytic attack that might have taken place after the cells were lysed to obtain the crude extract for purification.

Even though proteolysis was suspected, some of the MBP-$PilA_{20}$ fusions produced via cytoplasmic expression remained intact. Cleavage of the $PilA_{20}$ subunit from the MBP tag was tested using Factor Xa protease. Cleavage conditions tested included different temperatures ($4^{o}C$ and $23^{o}C$), incubation times (24 and 48 h), and concentration of Factor Xa protease (0.5 and 1 μg/mL). SDS-PAGE characterization after cleavage showed that the reaction efficiency depends on temperature, time, and concentration of Factor Xa (Figure 3.6). The gradual disappearance of the upper band and thickening of the lower band indicates the pilin is being cleaved from the MBP tag. Cleavage was more efficient at higher temperature ($23^{o}C$), higher concentration of Factor Xa, and longer incubation times. Almost complete cleavage was observed after 24 h when done at $23^{o}C$ using 1 μg/mL of Factor Xa (final concentration). Complete cleavage was not observed at $4^{o}C$ even after 48 h of incubation.

After cleavage, samples were analyzed by MALDI-TOF MS to confirm presence of the pilin subunit. MS indicated that two peptides were being produced during cleavage (Figure 3.7). The peak at 4,527.4 Da is consistent with the production of the $PilA_{20}$ subunit (theoretical molecular weight of $PilA_{20}$ is 4,523.9 Da). The second peak has a molecular weight of 3,563.3 Da. To check whether this peptide was the result of non-specific cleavage by Factor Xa protease, an HPLC-purified sample was sent for N-terminal sequencing of the first five amino acid residues (MSU Research Technology Support Facility). The sequence obtained was V-AYN (definite identification of second amino acid residue was not possible). Figure 3.7 shows where this sequence matches the $PilA_{20}$, and that a fragment starting at this point would have a molecular weight consistent with the result obtained by MS. Modifications in reaction conditions did not eliminate or reduce the non-specific cleavage.

Even though the pMAL expression system seemed very promising because of its previously reported success on the expression of recombinant pilin from *P. aeruginosa* [79], it did not give satisfactory results in the production of pilin from *G. sulfurreducens*. Degradation of the MBP-$PilA_{20}$ fusion protein produced either periplasmically or cytoplasmically was observed. Additionally, treatment with Factor Xa protease aimed at removing the MBP tag from the $PilA_{20}$ gave the undesired outcome of cleavage within the $PilA_{20}$ subunit.

The third expression system considered was the Intein-mediated purification with an affinity chitin binding tag system (IMPACT^{TM}, New England Biolabs Inc., Ipswich, MA). An advantage of this system is the use of a thiol-induced intein, which is a self-splicing protein that excise itself from the target protein in the presence of reducing agents, eliminating the need for

proteases for cleavage [90]. This system was used to express various truncations ($pilA_n$) of the *pilA* gene. The objective was to identify a relatively small number of amino acids to truncate (n) that would simultaneously give good expression of a soluble fusion in *E. coli*, as well as facile purification of pilins and *in-vitro* self-assembly of the purified $PilA_n$ peptide to yield synthetic pili. A chitin-binding domain (CBD) was attached to the N-terminus of the $pilA_n$ sequence. Clones were prepared for the full length pilin (PilA) and truncations $PilA_{10}$, $PilA_{19}$, $PilA_{20}$, and $PilA_{22}$. Constructs were transformed into Rosetta 2(DE3)pLysS *E. coli* cells, a strain that enhances expression of foreign proteins by addition of tRNAs for codons rarely used in *E. coli* (AGA, AGG, AUA, CUA, GGA, CCC, and CGG).

As evidenced by SDS-PAGE data, expression of the fusion protein was achieved for all truncated constructs (CBD-$PilA_{10}$, CBD-$PilA_{19}$, CBD-$PilA_{20}$, CBD-$PilA_{22}$) but not for the full length (CBD-PilA) (Figure 3.8). Cells expressing the CBD-PilA fusion only grew to a cell density ½ that of the other constructs. This suggests that CBD-PilA might be toxic to *E. coli* cells, probably because of the high hydrophobicity of the full length pilin.

Purification of truncated pilins was done by affinity chromatography with a column of chitin beads. On-column cleavage of the pilin from CBD was done by incubating with 50 mM DTT. Pilin peptides are released following cleavage, but the CBD tag remains bound to the chitin beads. After the pilin peptides were eluted from the affinity column, the cleavage efficiency was determined as a function of incubation time (24, 48, and 72 h) and temperature (4^oC and 23^oC). In SDS-PAGE analysis, the appearance of a second band lower in molecular weight than the CBD-$PilA_n$ fusion indicated cleavage of the $PilA_n$ monomer from the CBD tag

(Figure 3.9). Higher temperature (23^{o}C) produced more complete cleavage for all constructs. Cleavage of PilA$_{19}$ from CBD was faster when compared to PilA$_{10}$, PilA$_{20}$, and PilA$_{22}$, with nearly complete cleavage of PilA$_{19}$ observed at 23^{o}C after 24 h of incubation. PilA$_{10}$ showed approximately 50% cleavage after 24 h at 23^{o}C, and it did not seem to improve significantly over time. PilA$_{22}$ showed approximately 80% cleavage at 23^{o}C after 48 h of reaction. Cleavage was considerably less efficient for PilA$_{20}$ as it required at least 48 h of incubation at 23^{o}C to show any noticeable effect, probably because the amino acid closest to the cleavage site (isoleucine) is sub-optimal for the cleavage reaction with this expression vector. PilA$_{10}$ and PilA$_{19}$ have an alanine at the cleavage site, and PilA$_{22}$ has a glutamine; both of these amino acids are known to achieve higher cleavage efficiency when using this expression vector [91].

The elution fractions were analyzed by SDS-PAGE to confirm pilin production (Figure 3.10). Prominent bands were observed for PilA$_{19}$ and PilA$_{22}$ monomers when cleavage was done at 23^{o}C and 4^{o}C. Although some PilA$_{20}$ was cleaved from the fusion protein (Figure 3.9), soluble PilA$_{20}$ was not visible in the SDS-PAGE gels, indicating low cleavage efficiency of this construct. However, PilA$_{20}$ in the elution fraction was detected by MALDI-TOF mass spectrometry, a more sensitive technique (Figure 3.11). While significant cleavage of PilA$_{10}$ was observed (Figure 3.9), the subunits were only slightly visible in gels when cleavage was done at 4^{o}C (Figure 3.10), and no bands could be seen when cleavage was done at 23^{o}C. In addition, the matrix clogged when cleavage was performed on-column, suggesting that the PilA$_{10}$ subunits

aggregated after cleavage. The four truncated pilins have a molecular weight consistent with their theoretical molecular weight as confirmed by MALDI-TOF MS (Figure 3.11).

The IMPACT^{TM} expression system overcame the shortcomings of the other two systems. The fusion protein exhibited high solubility and no protease was required during cleavage. Four truncated constructs were expressed using this system. Even though the shortest truncation (longest pilin peptide) was expressed as a soluble fusion protein (CBD-PilA_{10}), the PilA_{10} subunit showed signs of aggregation after cleavage that made it challenging to purify in larger quantities. On the other hand, PilA_{19}, the second shortest truncation, was expressed well and could be recovered and purified readily, so it was selected for subsequent studies of pilin self-assembly.

3.3.2. Characterization of Secondary Structure of Pilin Subunits

One of the architectural features shared by type IV pilin monomers is the hydrophobic N-terminal α-helical spine known as α1 [17]. This helical structure plays a significant role in pilus assembly by forming a hydrophobic helical bundle in the filament core [47]. After production of PilA_{19} subunits, an important goal was to determine whether recombinant pilin retained this structural feature.

Two powerful techniques are generally used to determine the secondary and tertiary structure of proteins, x-ray crystallography and nuclear magnetic resonance (NMR). These methods provide structural information with atomic resolution [92, 93]. Although powerful, these techniques have experimental limitations. X-ray crystallography can be applied to large and small proteins but it requires the protein to be in crystalline form [93]. Crystallization

requires large amounts of protein to find optimum crystallization conditions and not all proteins are suitable for crystallization. NMR does not need protein crystallization, but it requires large quantities of soluble protein, extensive isotopic labeling, and considerable time. It is also limited to proteins with a molecular weight lower than 30 kDa [94].

The experimental restrictions inherent to x-ray crystallography and NMR analysis have increased the use of circular dichroism (CD) [93]. Circular dichroism allows the estimation of structural features of a protein. CD does not provide atomic resolution; it does not assign specific amino acids to a specific secondary structure [93]. However, CD can be applied to all proteins at low concentrations (< 20 μg) under various solvent conditions [84]. CD is very useful for rapid determination of conformational changes in protein structure resulting from temperature, pH, heat, mutations, detergents or denaturants, or binding interactions [84, 92]. CD is based on the difference in absorbance of right- and left-handed circularly polarized light as it passes through a chiral molecule [83]. For proteins, different secondary conformations have characteristic CD spectra. Disordered proteins have very low ellipticity above 210 nm and negative peaks near 195 nm. In contrast, α-helical peptides have two negative peaks at 222 nm and 208 nm, and a positive peak at 193 nm [83, 84].

Circular dichroism (CD) experiments were carried out to evaluate the secondary structure of $PilA_{19}$ monomers. To determine whether the net charge of the $PilA_{19}$ subunit would have an effect on the peptide secondary structure, CD experiments were performed at pH values below and above the isoelectric point (pI) (pH 3.8 and 7.0). The theoretical isoelectric point of the $PilA_{19}$ subunit is 4.86. The effect of detergents, sodium dodecyl sulfate (SDS) and octyl β-D-glucopyranoside (OG), on the conformation of the pilin monomer was investigated. SDS has been shown to induce and stabilize secondary structure, especially α-helices [95]. SDS is

commonly used to mimic membranes and other hydrophobic environments [95]. OG has been used to dissociate pili into pilins. The use of OG to depolymerize PAK pili demonstrated that OG produced pilin monomers without disrupting the peptide secondary structure [96]. Depolymerization of PAK pilin using SDS resulted in a 6% increase in α-helix [96]. The critical micelle concentrations (CMC) of these surfactants are ~ 8 mM for SDS and ~ 25 mM for OG [97, 98].

The effect of SDS on the CD spectra of PilA19 subunits at pH 3.8 and 7.0 is shown in Figures 3.12 and 3.13. Without detergent, the spectra suggest a disordered or unfolded peptide, with very low ellipticity above 210 nm. The presence of SDS resulted in the characteristic structural signature of a α-helix for all SDS concentrations and pH values tested. The effect of OG on the CD spectra of $PilA_{19}$ subunits at pH 3.8 and 7.0 is shown in Figures 3.14 and 3.15. When OG was present at a concentration close to the CMC (25 mM), no significant change in the shape of the spectra was observed at both pH values, indicating the protein was still in a disordered conformation. However, an OG concentration approximately five times higher than the CMC yielded an α-helical signature.

Since α-helical proteins exhibit a large positive peak at 193 nm, and two small negative peaks at 208 nm and 222 nm [83], the ellipticity values at these wavelengths were plotted (Figures 3.16 and 3.17). The changes observed after the addition of either SDS or OG followed similar patterns at both pH values investigated. The ellipticity at 193 nm increased after the addition of both surfactants. However, the change was more significant for SDS than for OG. The mean residue ellipticity values at 208 nm and 222 nm became more negative when detergents were added, with the effect larger for SDS than for OG. At pH 7.0, the values became more negative as the concentration of SDS increased, suggesting an increase in α-helical content

with SDS concentration. The behavior at pH 3.8 was different, with the ellipticity values at 208 nm and 222 nm becoming more negative in the following fashion: 0 SDS > 1 mM SDS > 40 mM SDS > 8 mM SDS.

To determine the percentage of the peptide having an α-helix conformation, the CD data were analyzed using the program CONTINLL. This program, which is available through the DICROWEB server [99, 100], is a modification of the CONTIN method developed by Provencher and Glöckner [101, 102]. It uses a ridge regression algorithm to estimate the CD spectrum of unknown proteins by comparison to a linear combination of CD spectra of *N* reference proteins with known conformations [84, 103]. Relatively good predictions of α-helix and β-sheet content can be obtained with this method [84]. The secondary structure components determined with CONTINLL are α-helix (regular α_R and distorted α_D), β-strands (regular β_R and distorted β_D), turns and unordered [103].

CONTINLL has been shown to give more accurate results than other CD-analysis algorithms in the case of polypeptides or short protein fragments [84]. However, the main limitation of the CONTINLL program is that the reference data sets currently available are compiled from globular proteins, and do not necessarily represent the correct conformation of peptides, fibrous, and membrane proteins [83, 84, 99].

The program evaluates the goodness of fit parameter normalized mean residue standard deviation (NMRSD), which is defined as:

$$NRMSD = \left[\frac{\sum \left(\theta_{\exp} - \theta_{cal} \right)^2}{\sum \left(\theta_{\exp} \right)^2} \right]^{1/2} \tag{3.4}$$

where θ_{exp} and θ_{cal} are the experimental and calculated ellipticity values at a specific wavelength. A NRMSD value of less than 0.1 is generally considered a good fit [83]. In the analysis presented here, data with NRMSD values above 0.12 were rejected. Samples with 125 mM OG at pH 3.8 and pH 7.0 have NRMSD values above 0.12. Therefore, these data were not considered during the analysis.

Table 3.3 shows the calculated percentage of the various secondary structure components for the conditions tested. The analysis is focused on the percentage of regular α-helix (α_R). The secondary structure calculations showed an increasing percentage of α-helix with increasing concentrations of SDS both at pH 3.8 and 7.0. The trend was also apparent when the data were plotted as percentage of regular α-helix versus the concentration of SDS at both pH values (Figure 3.18). The percentage of α-helix was higher at pH 3.8 than at 7.0. These calculations are consistent with qualitative observations based on changes in spectral shape and ellipticity values at 193 nm, 208 nm, and 222 nm after the addition of SDS.

Collectively, the CD results suggest that SDS triggers a conformational change of the pilin monomers that gives a more α-helical structure. This finding is consistent with previous reports that SDS stabilizes and induces secondary structures, especially α-helices [95]. SDS provides an environment that mimics the hydrophobic core and polar head of a membrane [95, 98]. Pili are transmembrane proteins that protrude from the outer membrane of *Geobacter* [17]. During pilus assembly, the hydrophobic part of pilin monomers is buried inside a helical coiled-coil structure in the filament core [17, 19]. We speculate that pilin monomers need that membrane-like environment that SDS provides to attain a more native α-helical structure. The

conserved ~ 53 residue helix at the N-terminus of type IV pilins controls inner membrane insertion, and pilin polymerization [17, 39]. The specific value of α-helical content for the wild type pilin (PilA) of *Geobacter* has not been determined yet for comparison with the experimental data for the recombinant $PilA_{19}$ subunit.

3.3.3. *In-vitro* Assembly of Recombinant Pilins into Pili Fibers

In previous work with *P. aeruginosa*, self-assembly of *in-vitro* expressed pilin into pilus-like structures was triggered when an aqueous solution of the pilins was contacted with hydrophobic undecanethiol or Superdex resin. This suggests that the nature of the hydrophobe may not be important and that the hydrophobe may only serve as a nucleation point for self-assembly [48]. We have used a different strategy to assemble *G. sulfurreducens* pilin subunits from solution. During pilus assembly, pilin monomers are held together by hydrophobic interactions [47]. We hypothesized that a hydrophobic environment could induce proper conformation and trigger assembly. Therefore, recombinant pilins were exchanged from buffer to an organic solvent. The organic solvent mixture was removed using a roto-evaporator, and the dry pellet was resuspended in DI water. TEM and AFM images of the resuspended pellet (Figures 3.19 and 3.20) showed micron size clusters of hair-like filaments that were less than 10 nm in diameter and several microns in length. Several factors may have contributed to pilin self-assembly as the solvent was removed, including a lack of buffer, salt, or detergent to stabilize the peptide solution, the peptide solubility limit being exceeded, and the presence of an air-water phase boundary.

3.3.4. Conductivity Assessment of Recombinant $PilA_{19}$ Fibers via STM

Scanning tunneling microscopy (STM) provides three-dimensional real space images and also allows spatial variations in the density of states within the sample to be probed with atomic resolution [104]. In STM, a bias voltage is applied between a sharp metal tip and a conductive sample as the two are brought close together. When the tip and the sample are separated by a few angstroms, the electron wave functions of the tip and the sample overlap, and a tunneling current is generated whose magnitude depends exponentially on the sample-tip distance. A piezoelectric control system with very high vertical resolution adjusts the position of the tip in three dimensions (*x*, *y*, and *z*) in response to the current [104, 105]. When the tip scans the sample in the x-y plane, changes in tunneling current are converted into an image and used to analyze the sample's topography and density of states [104, 105].

Wild type pili of *G. sulfurreducens* have been shown to be highly conductive [17]. STM experiments are being performed to assess whether the recombinant pili fibers are also conductive. Figure 3.21 shows an STM image collected at 0.05 V of a filament with a similar size and structure to that of the native pilus nanowire of *G. sulfurreducens*. Previous studies of wild type pili from *G. sulfurreducens* showed that the finite tip radius led to geometric convolution of the tip and the pilus in the resulting images [86]. This resulted in vertical flattening, decreasing the apparent height, and lateral broadening, enlarging the diameter.

The STM images obtained indicated that the recombinant pilus is electrically conductive, with the low voltage required to obtain the measured tunneling current consistent with conductivity. Complementary methods, such as scanning tunneling spectroscopy (STS) and CP-AFM would provide a more complete characterization of the electrical properties of the recombinant pilin fibers.

3.4. Conclusions

The IMPACT^{TM} expression system, which produced a CBD-PilA_n fusion, was selected for pilin subunit expression for several reasons: (1) no aggregation of the fusion protein was observed, (2) the fusion peptide was not susceptible to degradation, and (3) no proteases were required to cleave the fusion tag. To avoid problems associated with overexpressing hydrophobic recombinant peptides, a variety of N-terminal end truncations (PilA_{10}, PilA_{19}, PilA_{20}, and PilA_{22}) were evaluated for success in expression, purification and self-assembly. The PilA_{19} subunit was the shortest truncation that expressed well as a soluble fusion protein.

The CD spectrum for the purified PilA_{19} peptide in pure buffer was characteristic of a disordered secondary structure. However, after SDS addition, the CD spectrum exhibited the characteristic signature of an α-helix. This result is consistent with the hypothesis that the recombinant pilin monomers require a hydrophobic, membrane-like local environment to attain the α-helical structure characteristic of Type IV pilins.

Dissolution of purified PilA_{19} pilins in a hydrophobic solvent, followed by evaporation of the solvent, triggered pilin self-assembly into filaments. As indicated by both TEM and AFM analyses, the filaments had properties similar to native *G. sulfurreducens* Type IV pili, including a similar diameter and tendency to aggregate in tangled bundles. STM data indicated that the synthetic pili were conductive, but further studies are needed to more fully characterize the electrical properties.

The production and purification of truncated recombinant pilin monomers and subsequent assembly into synthetic pili demonstrated, for the first time, the feasibility of producing

nanostructured filaments based on conductive Geobacter pili. Conductive, synthetic pili represent a new class of protein-based nanowires that may be suitable for a wide range of applications.

Table 3.1 Restriction enzymes and primers used for cloning of $pilA_n$ gene into expression vectors.

Expression system cloning vectors		**Restriction enzymes**	**Primers**
QIAexpressionist pQE-30 UA (Amp^R)			Rev 5'-TGGATAGGCGGGCTTTCAAT-3'
			Fwd $pilA_{20}$ 5'-TTAACTTTCGGGCGGATAGGT-3'
pMAL	c4x (Amp^R)	Rev Hind III	Rev 5'-CCCAAGCTTTTAACTTTCGGGCGGATAGGT-3'
	p4x (Amp^R)	Fwd Xmn I	Fwd $pilA_{20}$ 5'-ATTCCGCAGTTCTCGGCGTA-3'
IMPACT PTYB11 (Amp^R)		Rev Pst I	Rev 5'-GGTGGTCTGCAGTCATTAACTTTCGGGCGGATAGGT-3'
		Fwd Sap I	Fwd *pilA* 5'-GGTGGTTGCTCTTCCAACTTCACCCTTATCGAGCTGCT-3'
			$pilA_{10}$ 5'-GGTGGTTGCTCTTCCAACGCGATCATCGGTATTCTCGC-3'
			$pilA_{19}$ 5'-GGTGGTTGCTCTTCCAACGCGATTCCGCAGTTCTCGGC-3'
			$pilA_{20}$ 5'-GGTGGTTGCTCTTCCAACATTCCGCAGTTCTCGGCGTA-3'
			$pilA_{22}$ 5'-GGTGGTTGCTCTTCCAACCAGTTCTCGGCGTATCGTGT-3'

Table 3.2 Bacterial strains used to express recombinant pilin subunits.

Expression system	***E. coli* strain**	**Characteristics**
QIAexpressionist™	M15[pREP4]	Kan^R
p-MAL™	K12 TB1	F^- *ara* Δ*(lac-proAB) [Φ80dlac* Δ*(lacZ)M15] rpsL*(Str^R) *thi hsdR*
IMPACT™	Rosetta 2 (DE3)pLysS[a]	F^- *ompT hsdS*$_B$(r_B^- m_B^-) *gal dcm* (DE3) pLysSRARE2 (Cam^R)

[a]Novagen, EMD Chemicals, Gibbstown, NJ

Table 3.3 Affinity resin and composition of buffers and solutions used during affinity chromatography purification of recombinant pilin subunits.

	QIAexpressionist™	**p-MAL™**	**IMPACT™**
Resin	Ni-NTA	Amylose	Chitin
Lysis Buffer	50 mM Na-phosphate pH 7.8, 0.3 mM NaCl, 10 mM βME, 2% CHAPS, 20 mM imidazole, 1mg/mL lyzozyme	20 mM Tris-HCl pH 7.4, 200 mM NaCl, 1 mM EDTA, 1 mM PMSF	20 mM Tris-HCl pH 7.4, 100 mM NaCl, 1 mM EDTA, 1 mM PMSF, 2% CHAPS
Osmotic Shock		30 mM Tris-HCl pH 8.0, 20% sucrose, 1 mM EDTA (incubate 5-10 min, centrifuge at 8000 × g for 20 minutes at 4^{o}C) Resuspend pellet in 5 mM $MgSO_4$ ice cold (stir for 10 min, centrifuge at 8000 × g for 20 minutes at 4^{o}C). Supernatant is osmotic shock fluid.	
Wash Buffer	50 mM Na-phosphate pH 7.8, 0.3 mM NaCl, 10 mM βME, 0.2% CHAPS, 20 mM imidazole	20 mM Tris-HCl pH 7.4, 200 mM NaCl, 1 mM EDTA	20 mM Tris-HCl pH 7.4, 600 mM or 1 M NaCl, 1 mM EDTA
Cleavage Buffer			20 mM Tris-HCl pH 9.0, 100 mM NaCl, 50 mM DTT
Elution Buffer	50 mM Na-phosphate pH 7.8, 0.3 mM NaCl, 10 mM βME, 0.2% CHAPS, 300 mM imidazole	20 mM Tris-HCl pH 7.4, 200 mM NaCl, 1 mM EDTA, 10 mM maltose	20 mM Tris-HCl pH 9.0, 100 mM NaCl, 1% OG

Table 3.4 Analysis of CD data using the CONTINLL algorithm. The various secondary structures determined are α-helix (regular α_R and distorted α_D), β-strands (regular β_R and distorted β_D), turns and unordered. The NRMSD parameter indicates the goodness of fit. Values below 0.1 are considered a good fit.

% secondary structure												
Type of secondary structure	**No detergent**		**1 mM SDS**		**8 mM SDS**		**40 mM SDS**		**25 mM OG**		**125 mM OG**	
	pH 3.8	**pH 7.0**	**pH 3.8**	**pH 7.0**	**pH 3.8**	**pH 7.0**	**pH 3.8**	**pH 7.0**	**pH 3.8**	**pH 7.0**	**pH 3.8**	**pH 7.0**
α_R	1.2	1.7	33.7	19.2	37.2	28.6	38	31.3	5.4	3.5	15.6	26.9
α_D	3.0	4.9	14.9	7.6	18.4	14.5	18.3	17.0	5.7	5.2	6	14.9
β_R	13.9	9.1	18.5	13.6	1.6	5.7	5.8	0.9	11.9	7.4	19.7	21.8
β_D	6.6	5.1	10.2	4.1	2.7	2.9	4.1	2.6	6.2	4.1	6.8	12
Turns	12.0	11.9	22.7	9.6	13.6	12.7	14.8	14.3	12.7	10.4	13.5	24.5
Un-ordered	63.2	67.2	0	45.9	26.6	35.6	18.9	33.8	58.2	69.3	38.4	0
Total	99.9	99.9	100	100	100.1	100	99.9	99.9	100.1	99.9	100	100.1
NRMSD	0.045	0.068	0.036	0.113	0.058	0.119	0.028	0.117	0.073	0.073	0.177	0.206

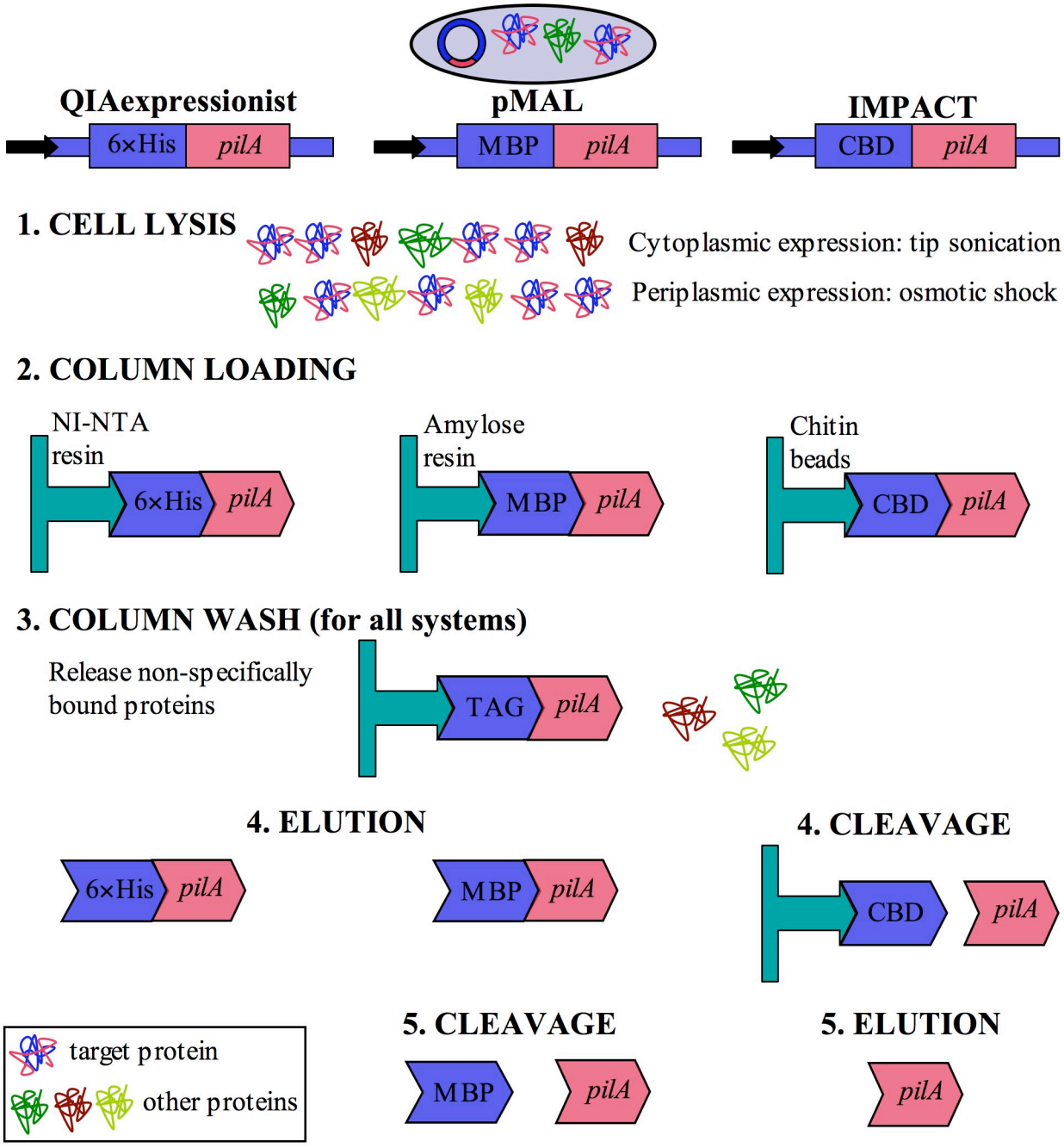

Figure 3.1 Purification steps used for each expression system.

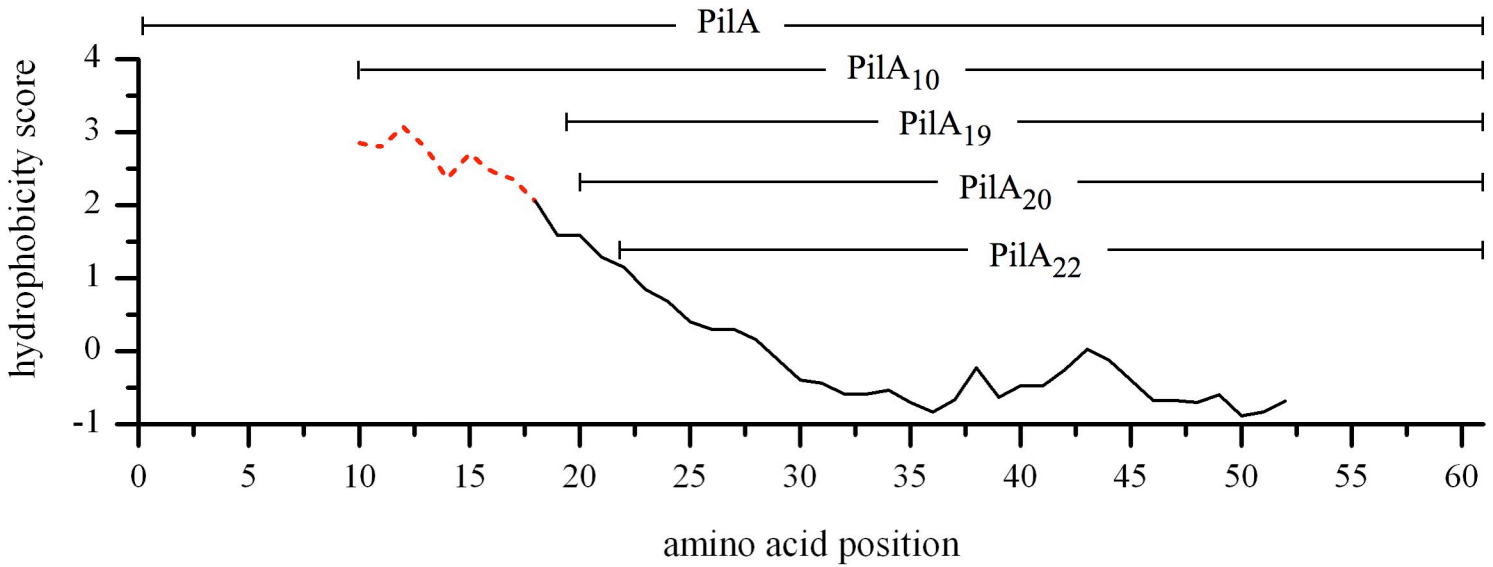

		GRAVY
PilA	FTLIELLIVVAIIGILAAIAIPQFSAYRVKAYNSAASSDLRNLKTALESAFADDQTYPPES	0.510
$PilA_{10}$	----------AIIGILAAIAIPQFSAYRVKAYNSAASSDLRNLKTALESAFADDQTYPPES	0.073
$PilA_{19}$	------------------AIPQFSAYRVKAYNSAASSDLRNLKTALESAFADDQTYPPES	-0.550
$PilA_{20}$	--------------------IPQFSAYRVKAYNSAASSDLRNLKTALESAFADDQTYPPES	-0.607
$PilA_{22}$	----------------------QFSAYRVKAYNSAASSDLRNLKTALESAFADDQTYPPES	-0.713

Figure 3.2 Analysis of hydrophobicity of pilin subunits and effect of amino acid truncation. Kyte and Doolittle hydrophaticity [87] plot using a 19-residue segment, amino acid sequence and GRAVY index of PilA and $PilA_n$ truncations.

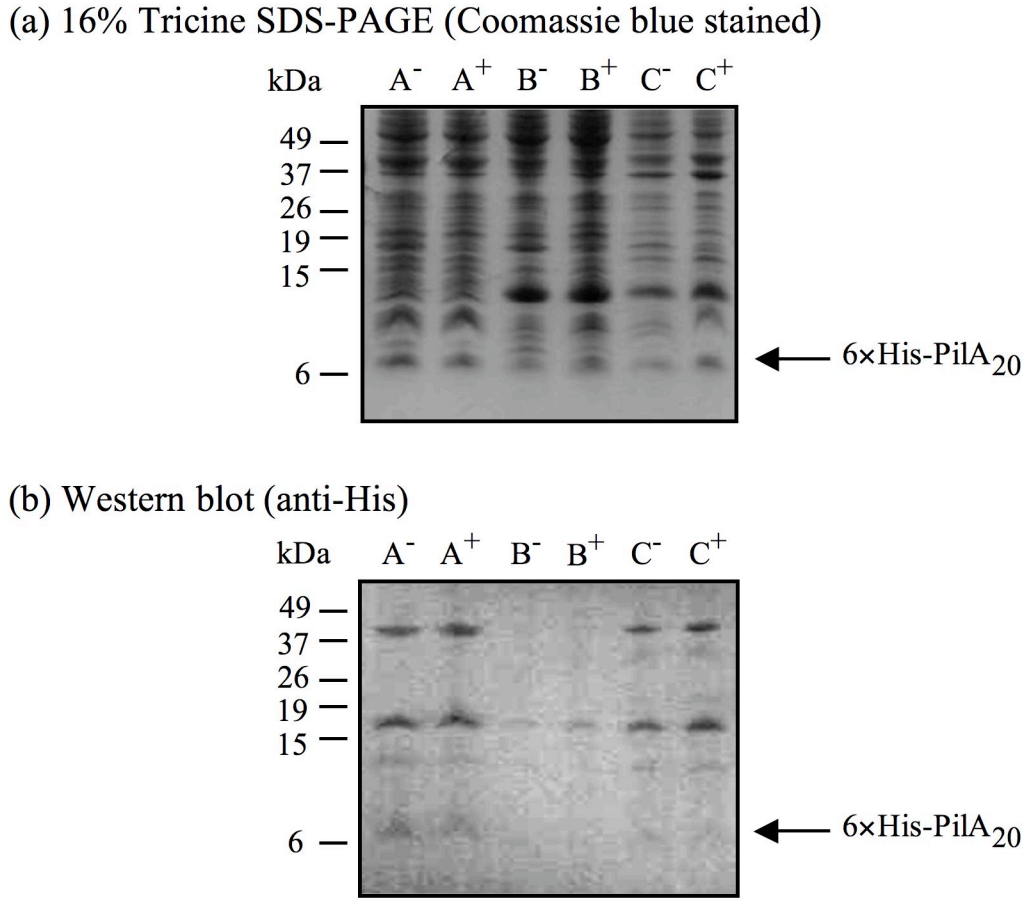

Figure 3.3 Expression and purification of 6×His-PilA$_{20}$. a) 16% tricine SDS-PAGE and b) western blot analysis of cell pellet (A), soluble fraction of cell lysate (B), and insoluble fraction of cell lysate (C); before (-) and after (+) induction.

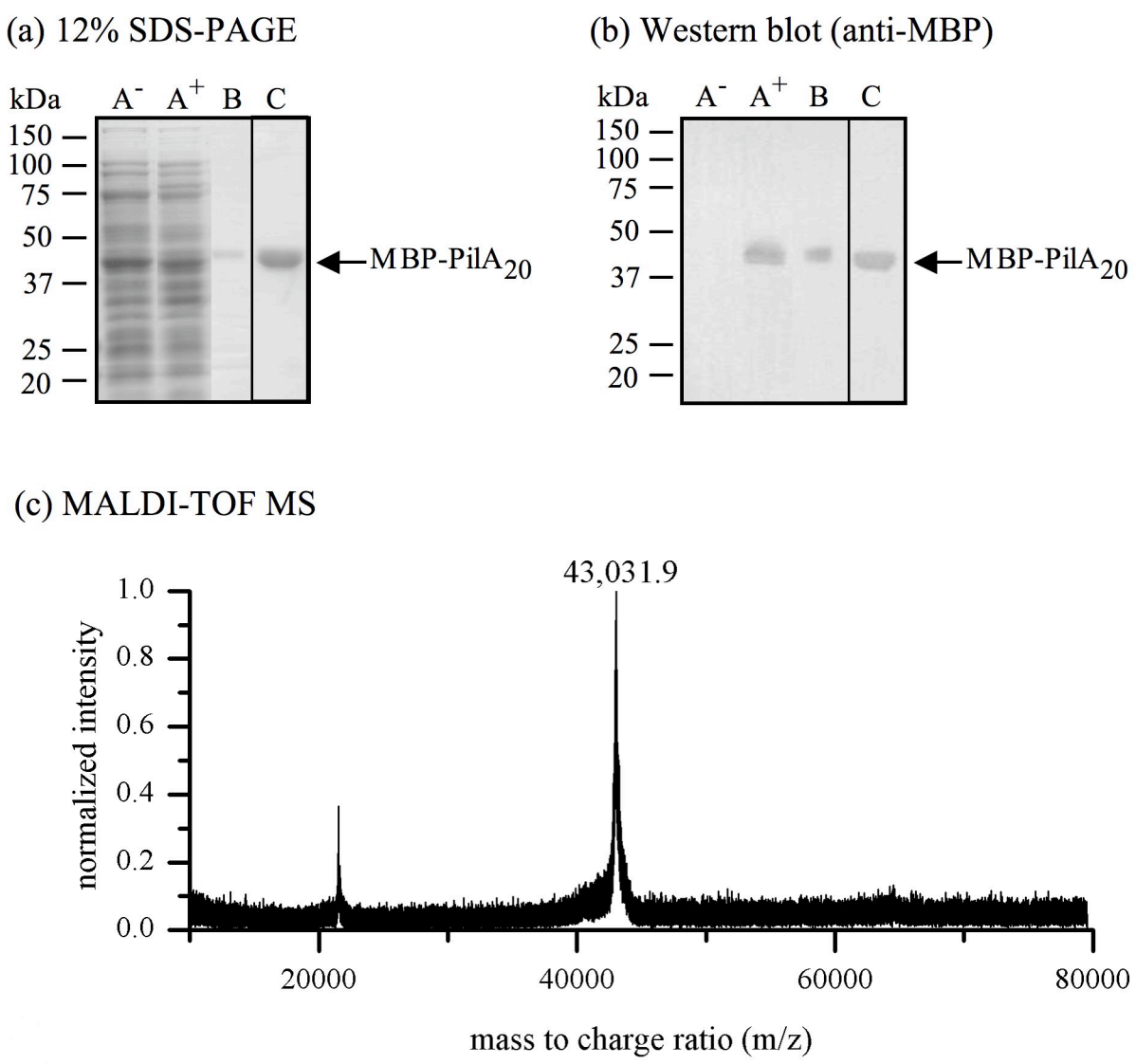

Figure 3.4 Periplasmic expression and purification of MBP-PilA$_{20}$. a) 12% glycine SDS-PAGE and b) western blot analysis of crude extract (A) before (-) and after (+) induction; soluble fraction of cell lysate (B), and elution fraction from amylose column (C); c) MALDI-TOF MS analysis of elution fraction from amylose column. Theoretical molecular weight of the periplasmic MBP-PilA$_{20}$ fusion is 46,902.6 Da.

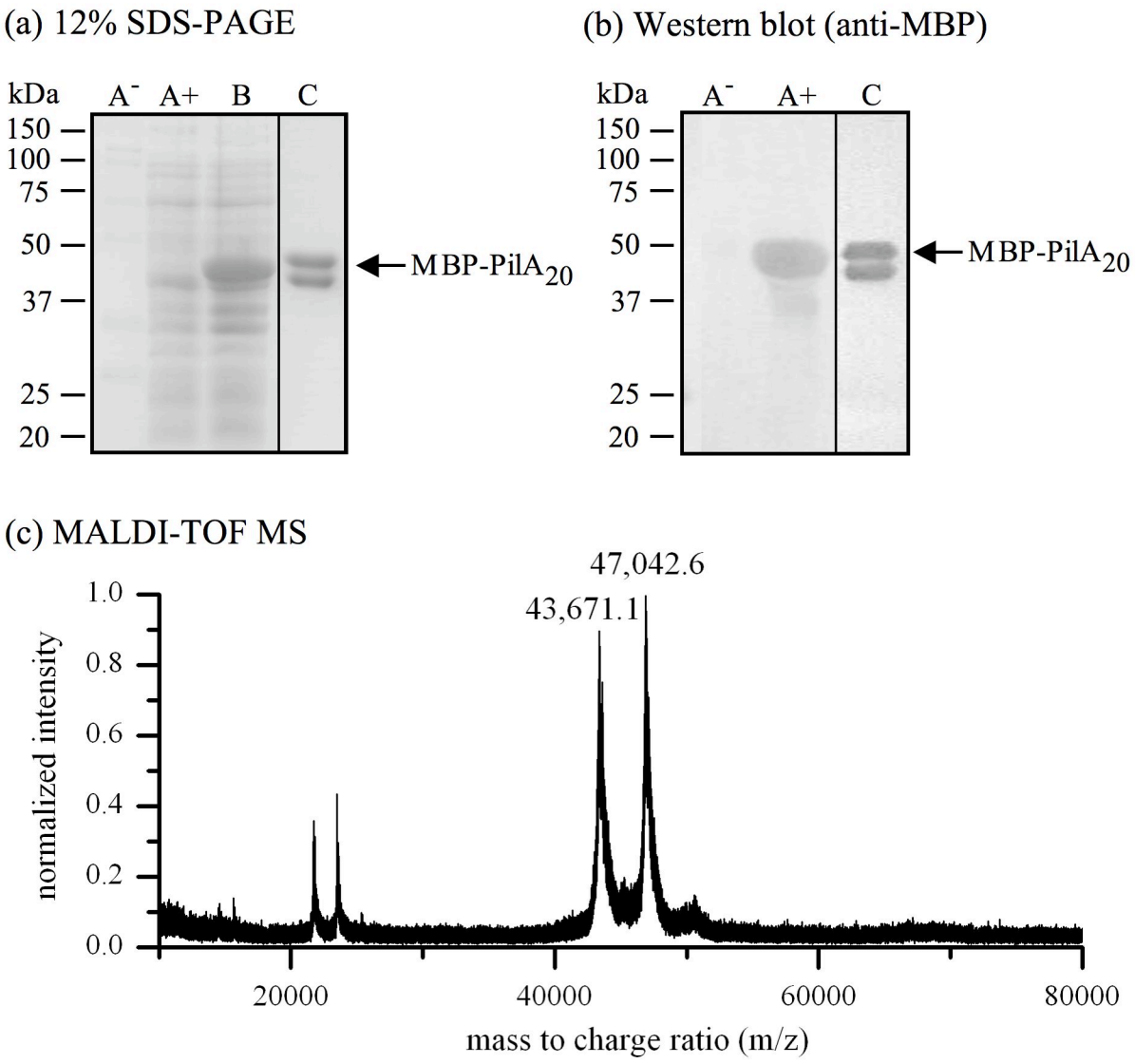

Figure 3.5 Cytoplasmic expression and purification of MBP-PilA$_{20}$. a) 12% glycine SDS-PAGE and b) western blot analysis of crude extract (A) before (-) and after (+) induction; soluble fraction of cell lysate (B), and elution fraction from amylose column (C); c) MALDI-TOF MS analysis of elution fraction from amylose column. Theoretical molecular weight of the periplasmic MBP-PilA$_{20}$ fusion is 47,033.9 Da.

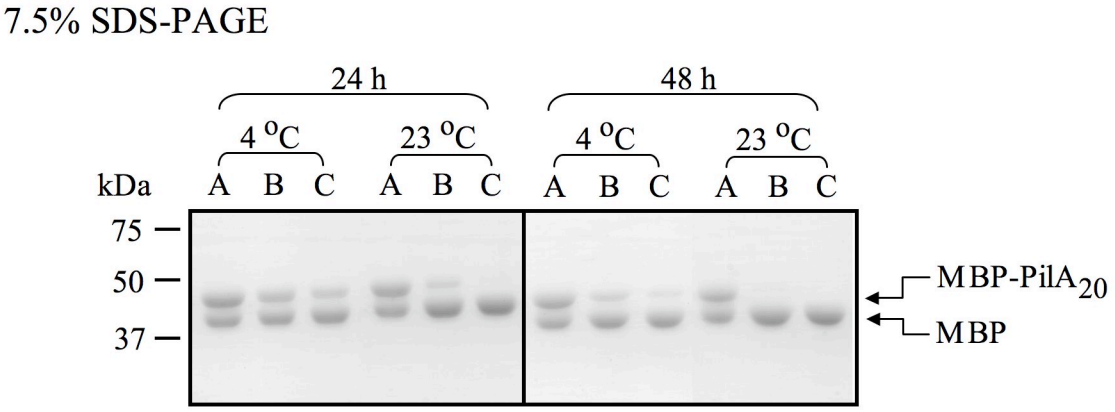

Figure 3.6 Cleavage efficiency of $PilA_{20}$ subunit from MBP tag mediated by Factor Xa protease. Elution fractions from amylose column were incubated with Factor Xa protease at $4^{o}C$ and $23^{o}C$. Samples were analyzed by 7.5% glycine SDS-PAGE after 24 h and 48 h of reaction. Gels show elution sample untreated with protease as control (A), elution treated with 0.5 μg/mL (B), and elution treated with 1.0 μg/mL (C).

(a) control

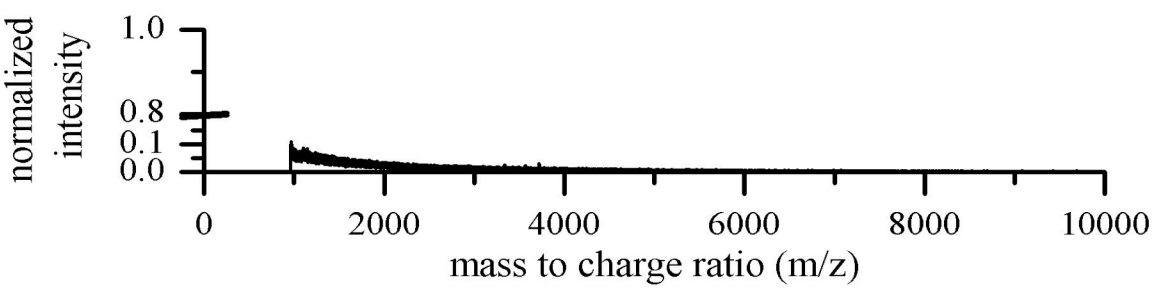

(b) cleavage $PilA_{20}$ (after treatment with Factor Xa)

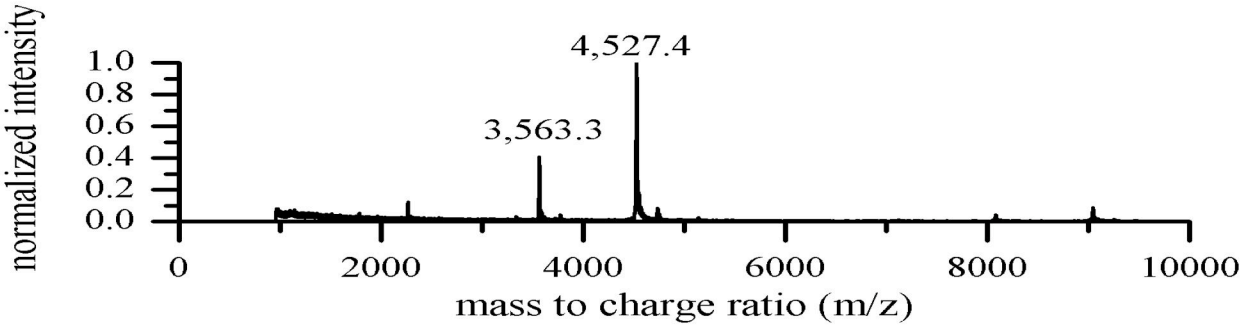

(c) N-terminal sequencing 3,563.3 Da peptide

		Theoretical MW (kDa)
5aa sequence	V-AYN----------	
$PilA_{20}$	IPQFSAYRVKAYNSAASSDLRNLKTALESAFADDQTYPPES	4,523.9
	VKAYNSAASSDLRNLKTALESAFADDQTYPPES	3,560.8

Figure 3.7 Production of $PilA_{20}$ subunits after treatment with Factor Xa protease. MALDI-TOF MS analysis of a) sample untreated with protease used as a control, and b) sample treated with protease. MS results indicate two peptides are produced during cleavage. The peptide with MW of 4,527.4 Da corresponds to the $PilA_{20}$ subunit. c) N-terminal sequencing of the peptide with MW of 3,563.3 Da. Sequencing indicated that non-specific cleavage of the pilin subunit occurred.

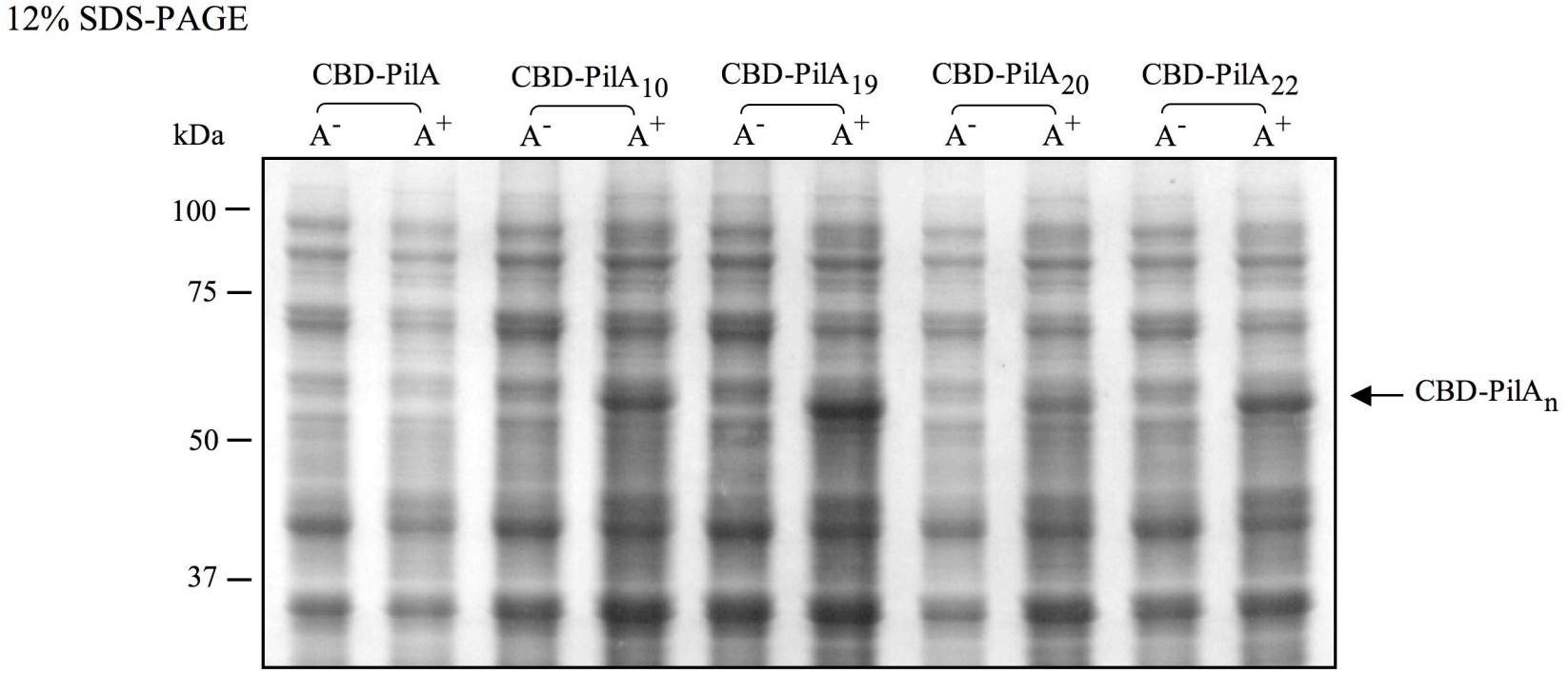

Figure 3.8 Expression of various truncations of pilin subunits using a CBD fusion tag (CBD-PilA$_n$). Expression was determined by analyzing cell pellet samples before (A^-) and after (A^+) induction using a 12% glycine SDS-PAGE.

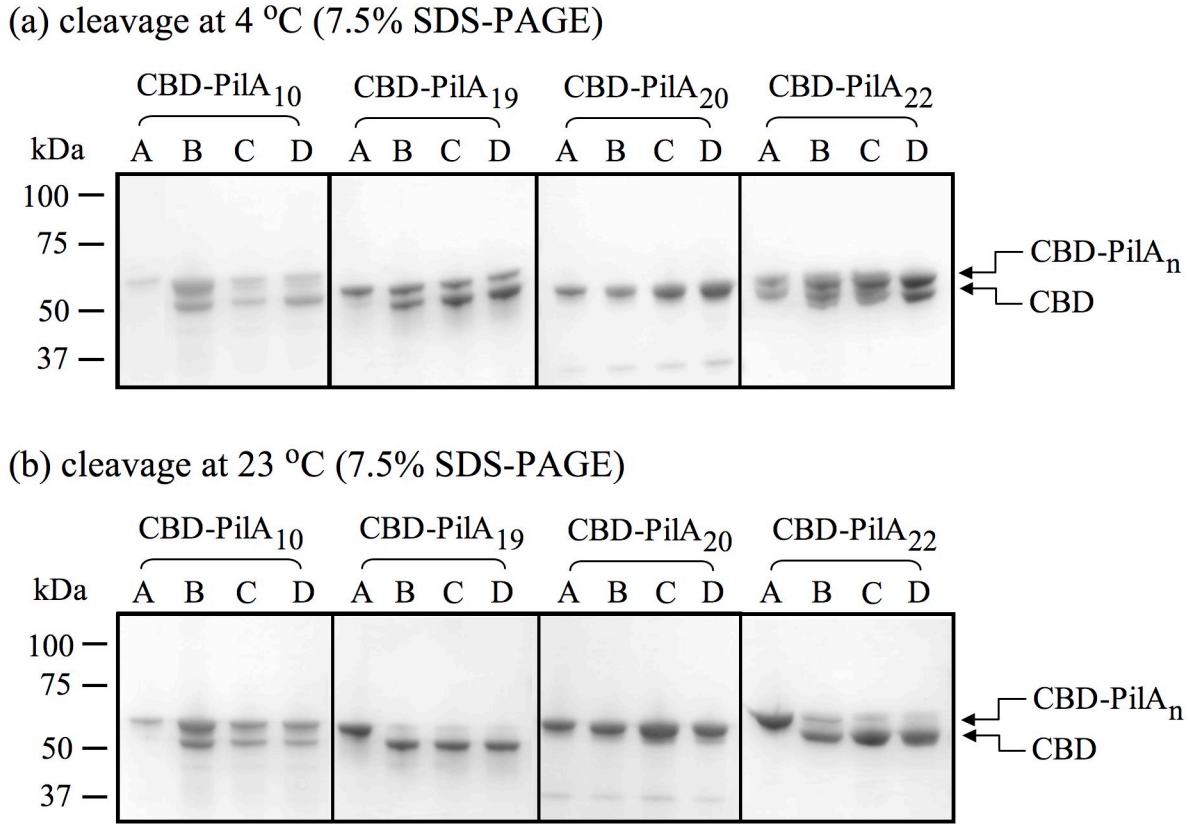

Figure 3.9 Cleavage efficiency of CBD tag from $PilA_n$ subunits after incubation with 50 mM DTT at 4°C and 23°C. During cleavage, pilin monomers are released but CBD remains bound to the chitin beads. Chitin beads were boiled with 1% SDS to release bound protein, which was analyzed by 7.5% glycine SDS-PAGE. Control (no DTT in incubation buffer) (A), cleavage efficiency after 24 h (B), 48 h (C), and 72 h (C). The appearance of a lower molecular weight band indicates the cleavage.

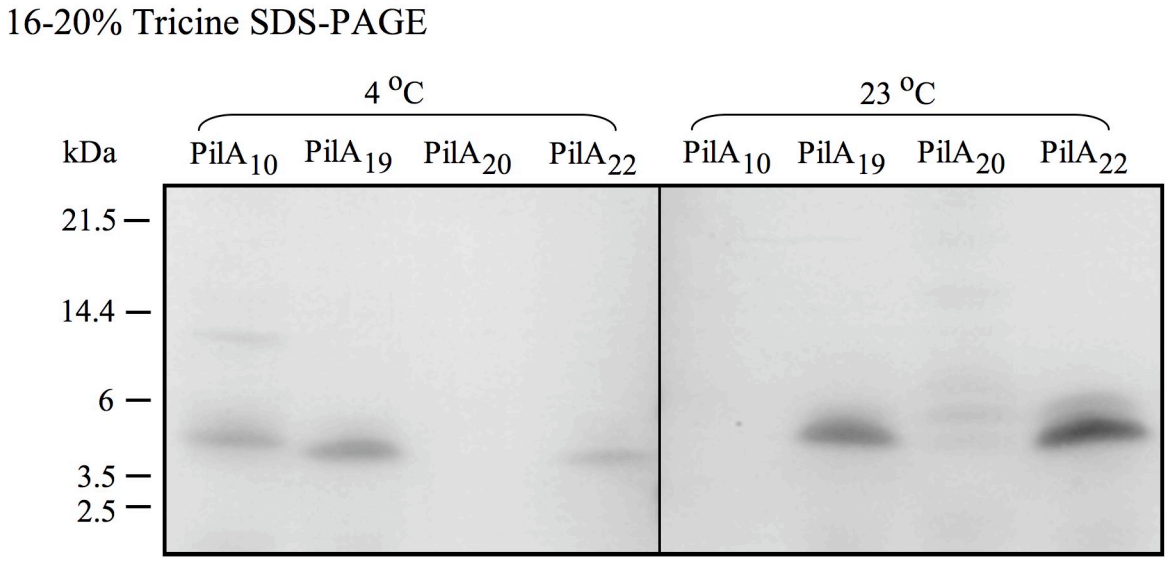

Figure 3.10 Presence of pilin monomers in elution from chitin column after cleavage from CBD tag determined by 16-20% Tricine SDS-PAGE.

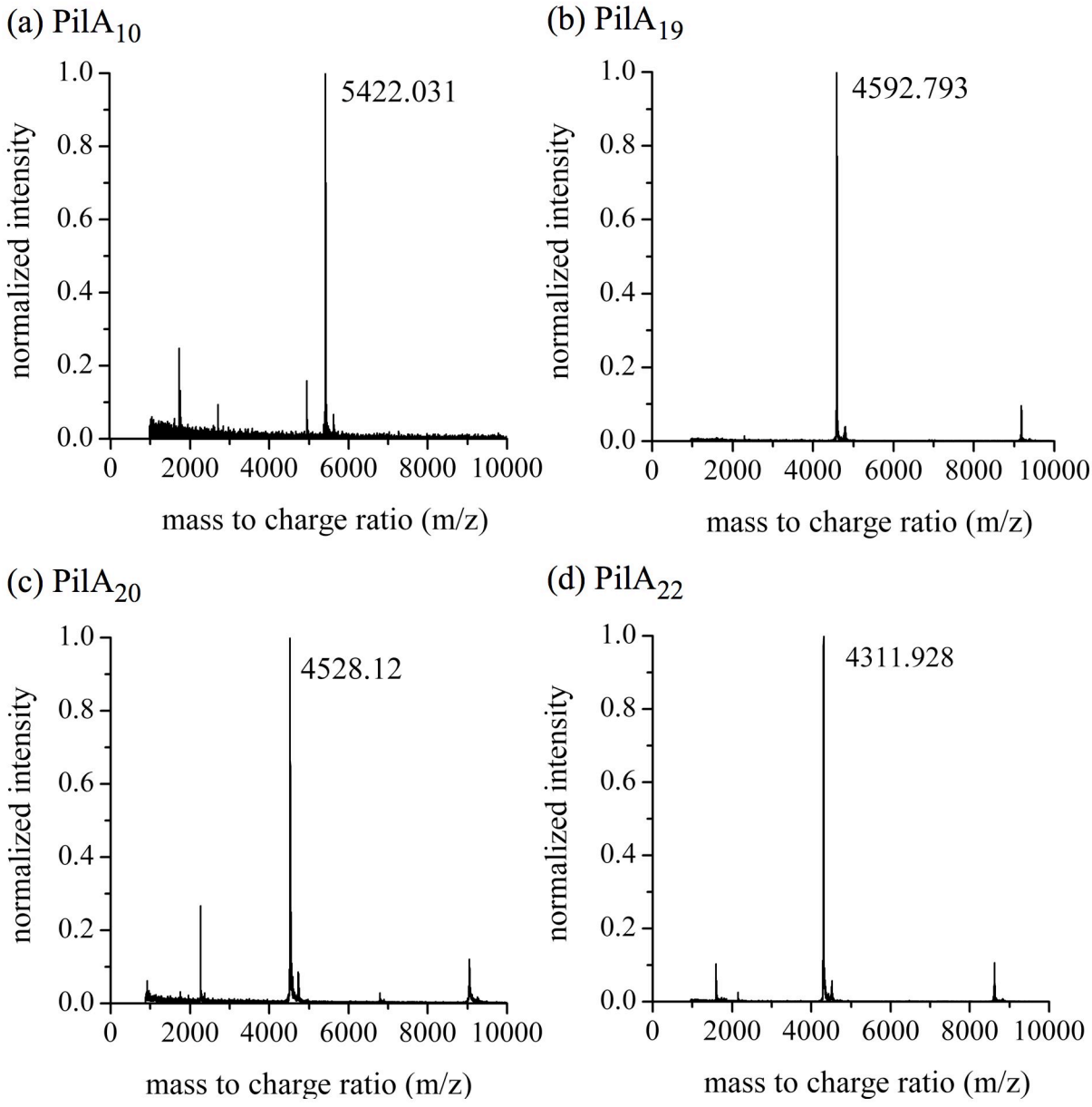

Figure 3.11 MALDI-TOF MS analysis of elution from chitin column after cleavage. MS analysis confirmed the molecular weight of the four truncated pilins. Theoretical molecular weights of the truncated pilins are $PilA_{10}$: 5,431 Da, $PilA_{19}$: 4,595 Da, $PilA_{20}$: 4,524 Da, and $PilA_{22}$: 4,314 Da.

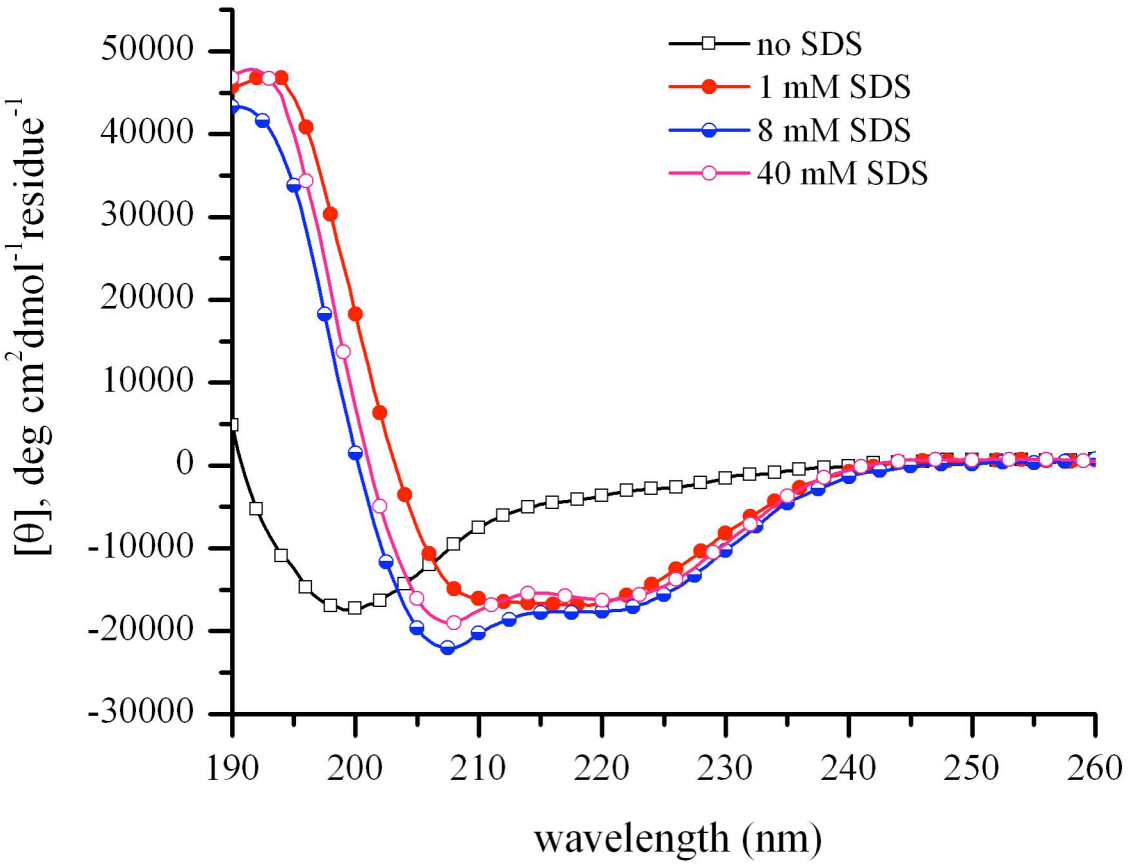

Figure 3.12 Surfactant-dependent folding of recombinant $PilA_{19}$ subunits at pH 3.8. CD Spectra of $PilA_{19}$ subunits in 10 mM potassium acetate pH 3.8, 50 mM Na_2SO_4 with and without sodium dodecyl sulfate (SDS).

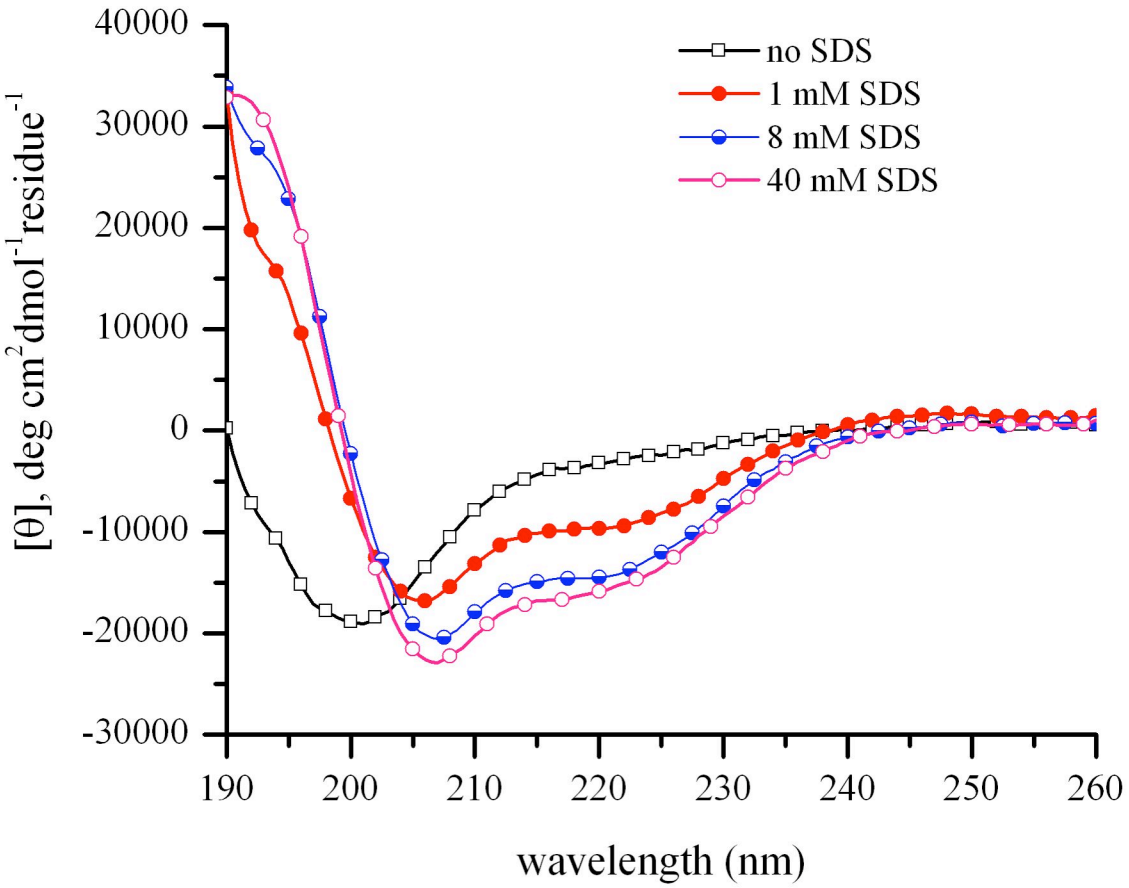

Figure 3.13 Surfactant-dependent folding of recombinant $PilA_{19}$ subunits at pH 7.0. CD Spectra of $PilA_{19}$ subunits in 10 mM potassium acetate pH 7.0, 50 mM Na_2SO_4 with and without sodium dodecyl sulfate (SDS).

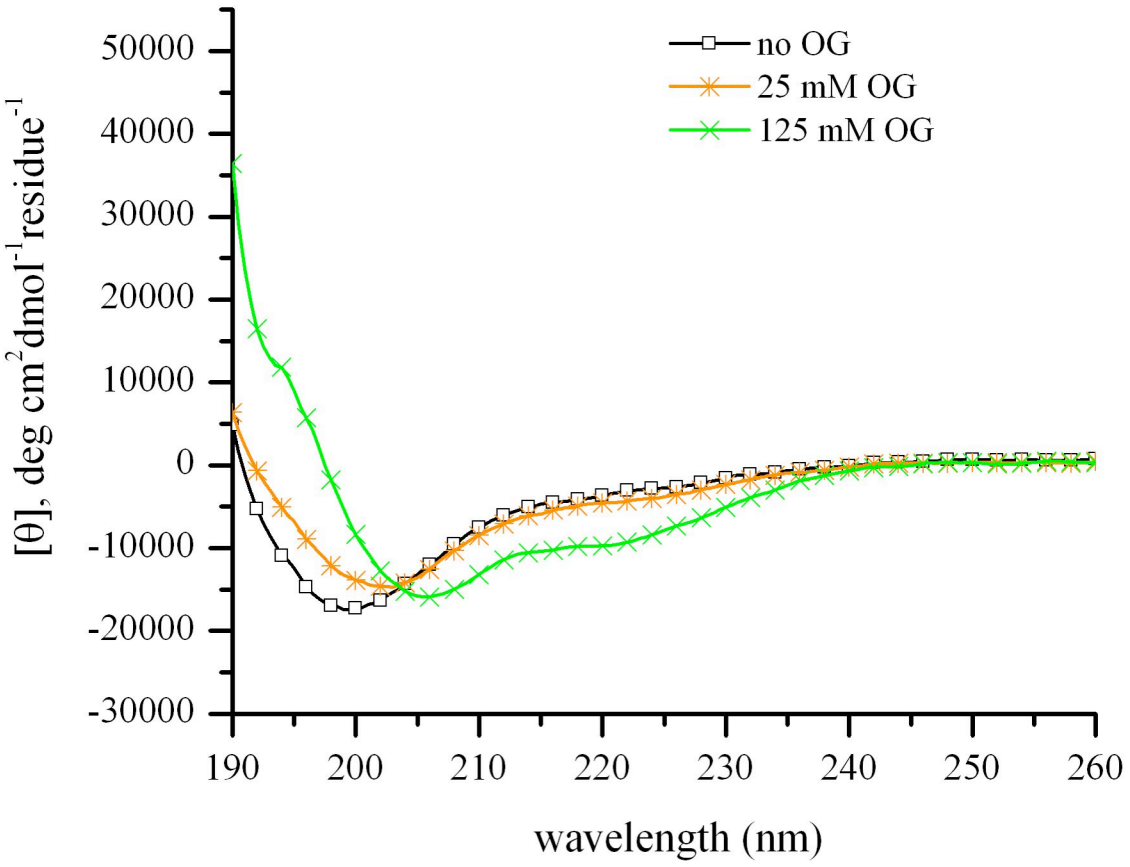

Figure 3.14 Surfactant-dependent folding of recombinant $PilA_{19}$ subunits at pH 3.8. CD Spectra of $PilA_{19}$ subunits in 10 mM potassium acetate pH 3.8, 50 mM Na_2SO_4 with and without octyl β-D-glucopyranoside (OG).

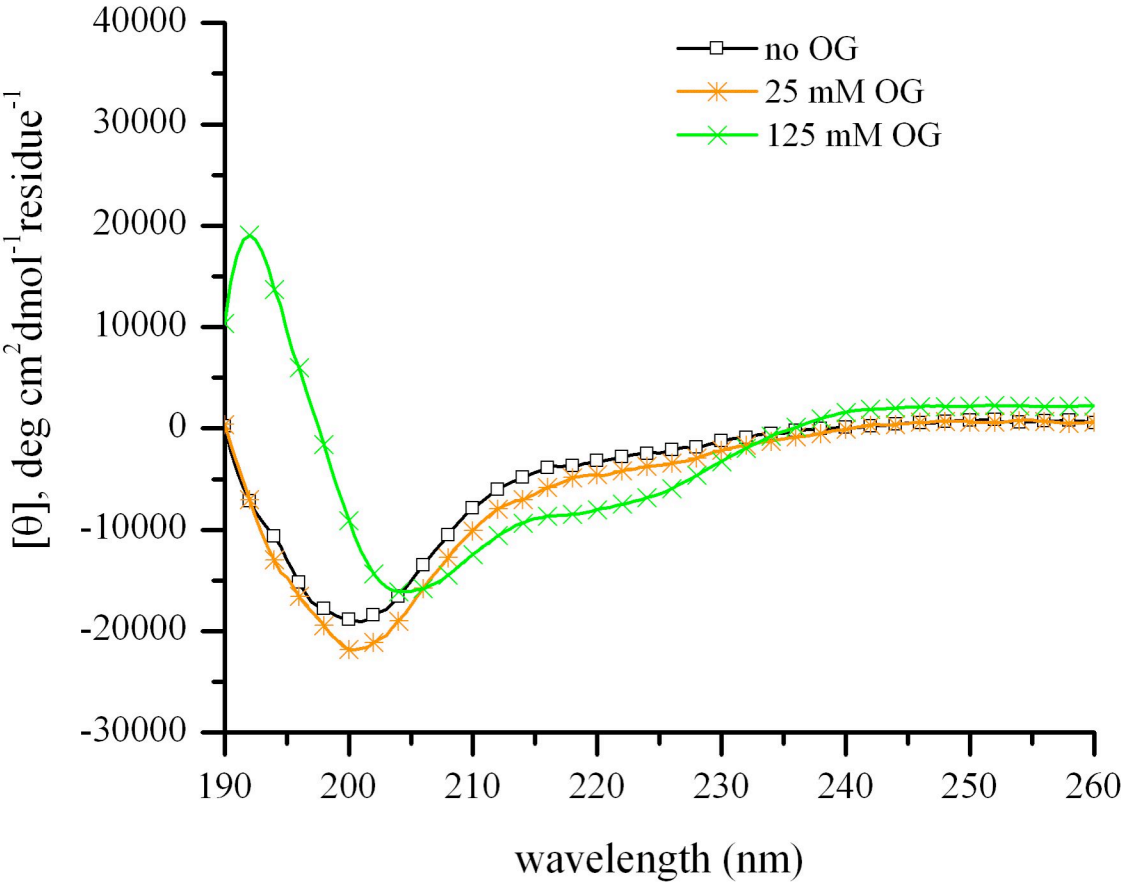

Figure 3.15 Surfactant-dependent folding of recombinant $PilA_{19}$ subunits at pH 7.0. CD Spectra of $PilA_{19}$ subunits in 10 mM potassium acetate pH 7.0, 50 mM Na_2SO_4 with and without octyl β-D-glucopyranoside (OG).

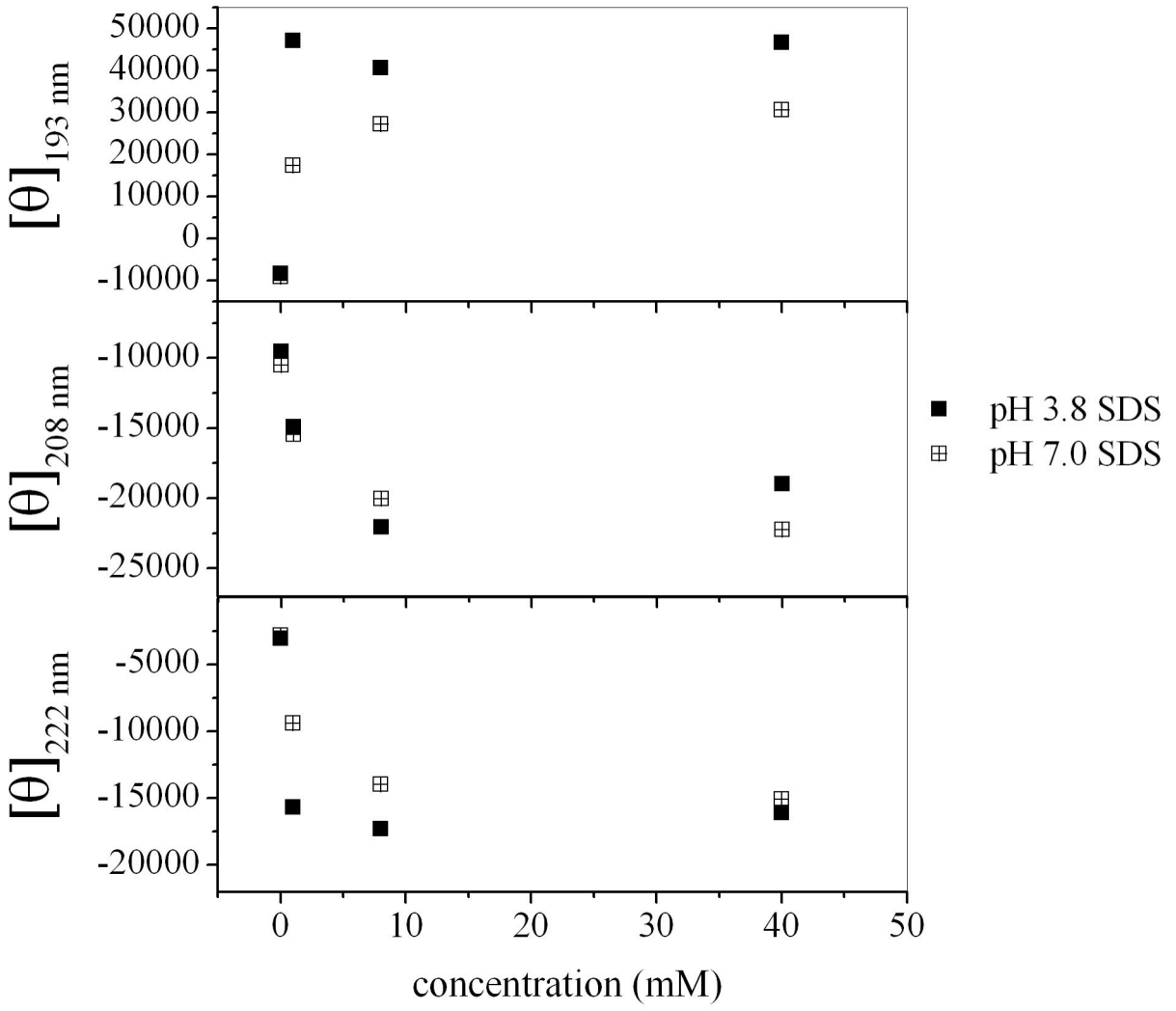

Figure 3.16 Effect of sodium dodecyl sulfate (SDS) on the conformation of $PilA_{19}$ subunits. Molar ellipticities at pH 3.8 and 7.0 are plotted for three wavelengths, 192, 208, and 222 nm, as a function of SDS concentration.

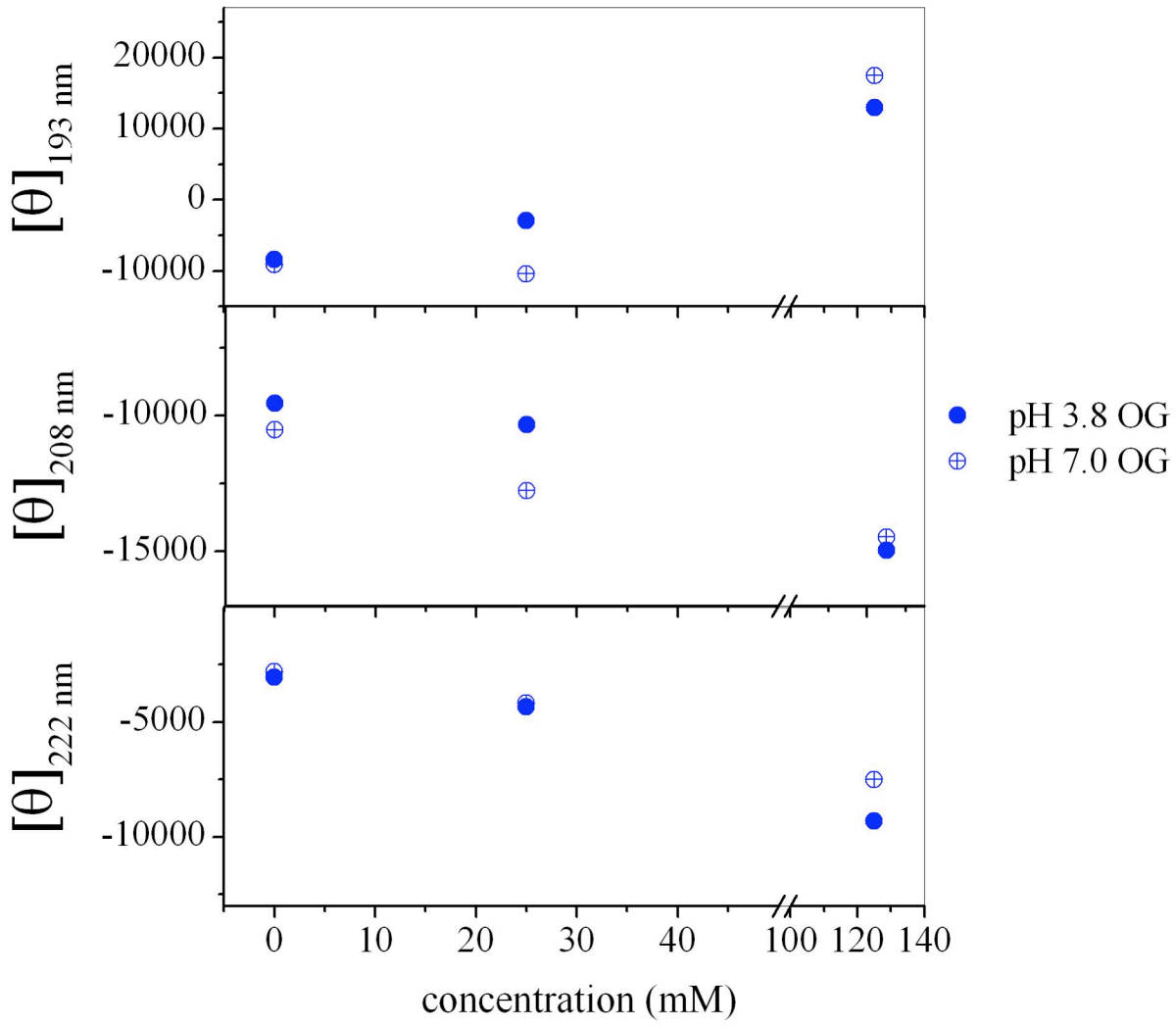

Figure 3.17 Effect of octyl β-D-glucopyranoside (OG) on the conformation of $PilA_{19}$ subunits. Molar ellipticities at pH 3.8 and 7.0 are plotted for three wavelengths, 192, 208, and 222 nm, as a function of SDS concentration.

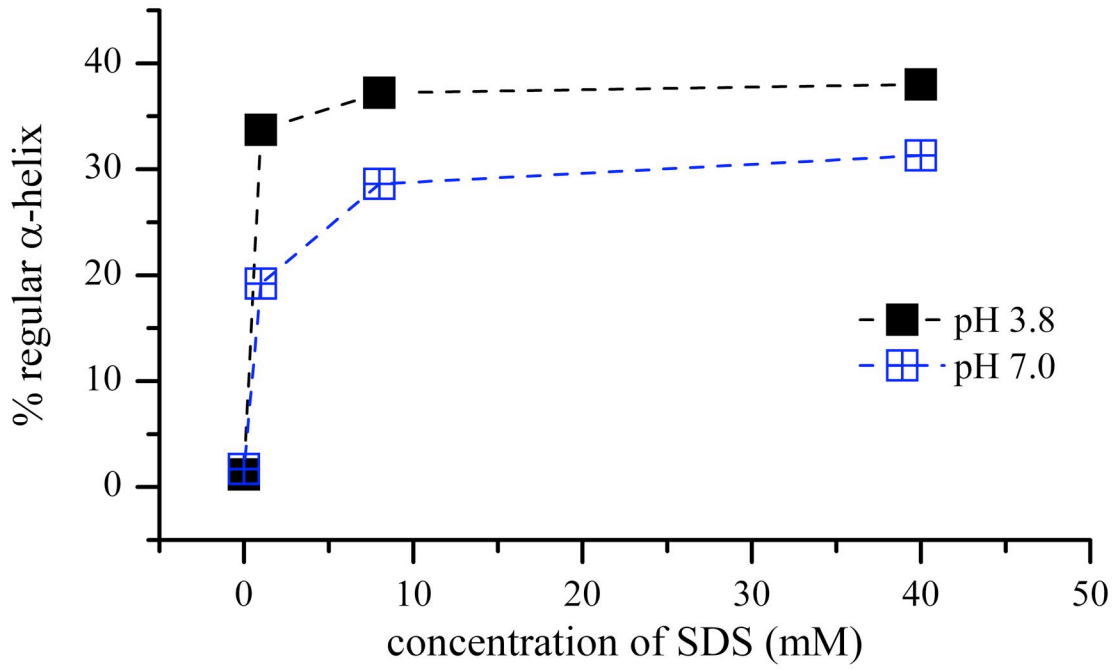

Figure 3.18 Effect of SDS on the percentage of regular α-helix of $PilA_{19}$ subunits at pH 3.8 and 7.0. Percentage of regular α-helix was calculated using the CONTINLL algorithm. Lines connecting data points are for visual aid only.

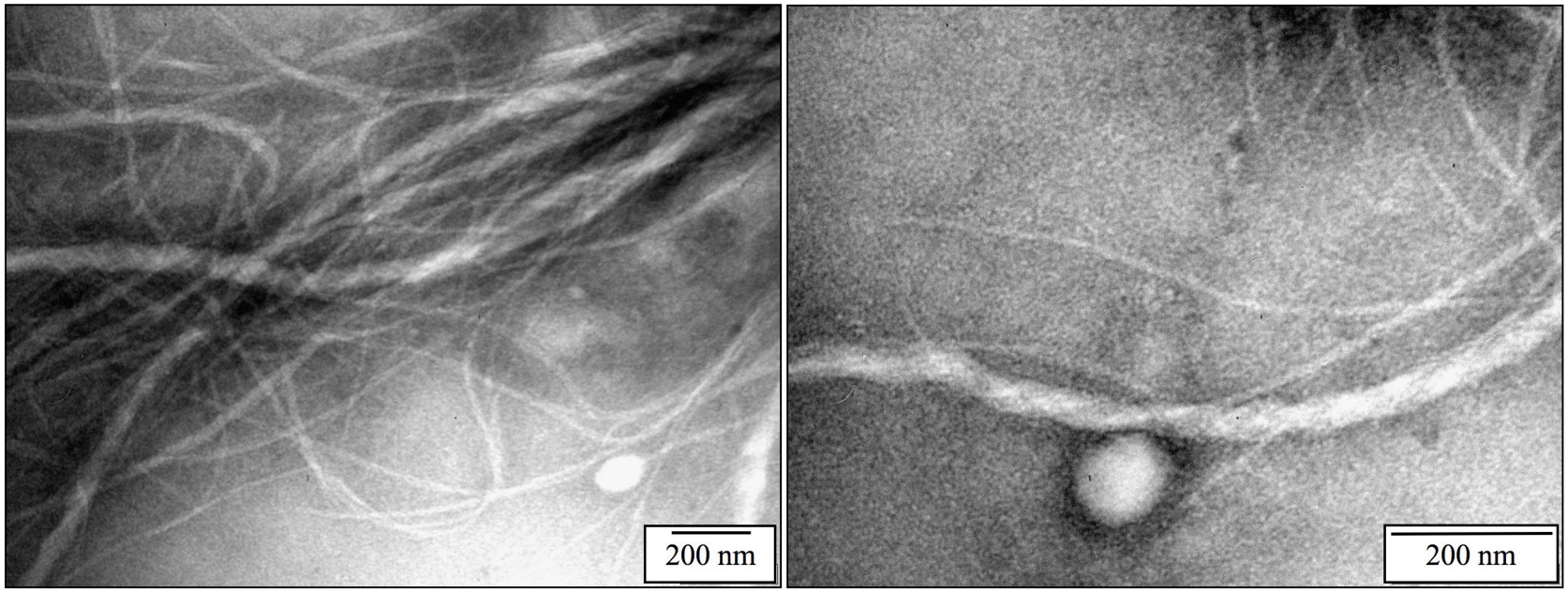

Figure 3.19 Transmission electron microscopy images of recombinant pili fibers. Samples were stained with uranyl acetate. TEM JEOL 2200FS (JEOL Inc., Boston, MA) operated at an accelerating voltage of 100 kV.

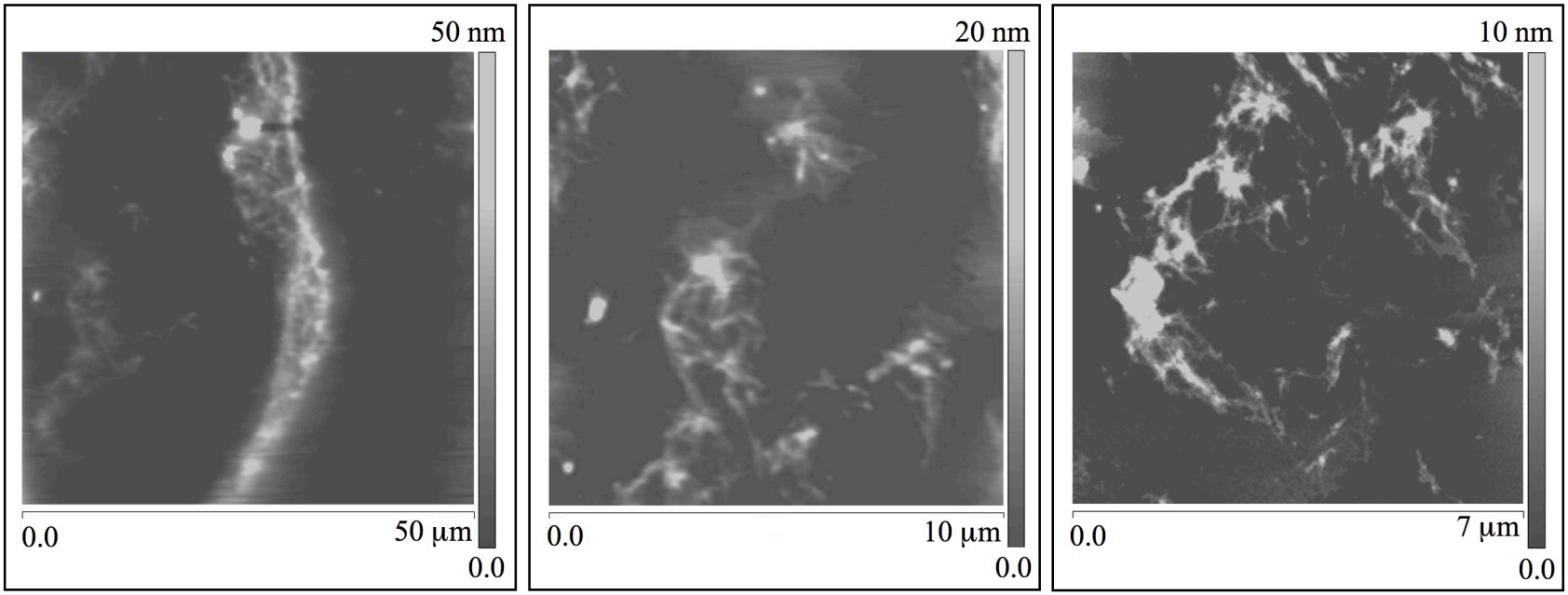

Figure 3.20 Atomic force microscopy images of recombinant pili deposited on mica. Tapping mode in air.

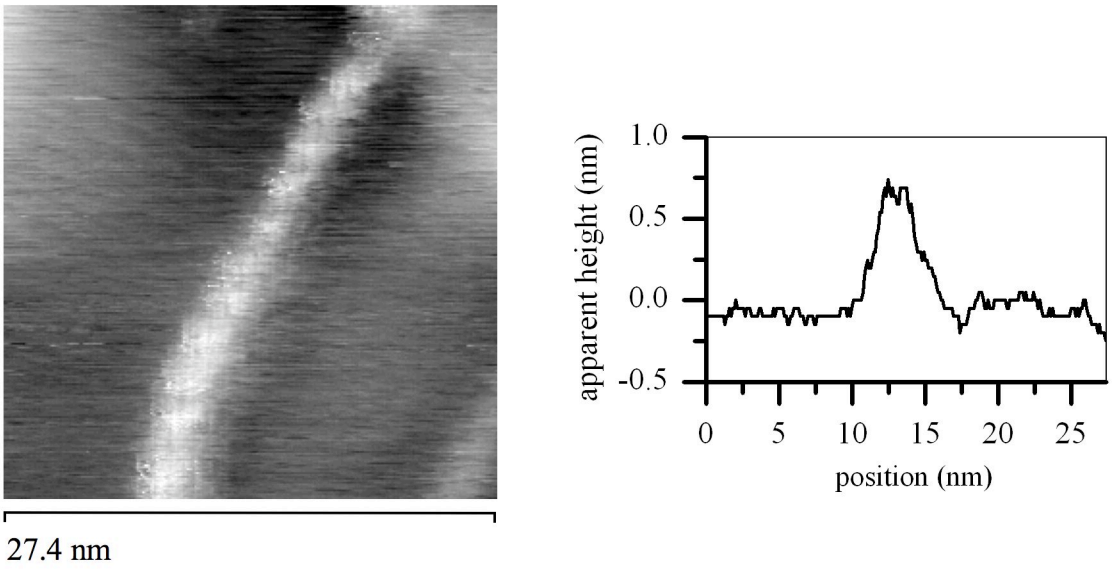

Figure 3.21 Scanning tunneling microscopy image of a recombinant $PilA_{19}$ fiber at an applied voltage of 0.05 V.

Chapter 4.

STUDY OF PILIN MODIFICATIONS TO ENABLE INTERFACING WITH ELECTRODES

4.1. Introduction

Protein assemblies, which are essential components in viruses, bacteria, eukaryotic cells, and organisms, participate in transport of intracellular and intercellular cargo and act as cytoskeletal scaffolds, storage containers, and molecular motors [4, 106]. These multi-subunit complexes self-assemble into specific architectures with controlled shapes and physicochemical properties, making them ideal for bottom-up fabrication in bionanotechnology applications [4]. Protein assemblies such as beta-amyloid fibrous proteins, viral proteins, bacterial pili and bacterial flagella are being investigated as alternative components of nanostructured devices [77, 78].

The self-assembling capability of bacterial pili might be a useful feature in bottom-up fabrication of interfaces [48, 80]. An added advantage of using the pili of *Geobacter sulfurreducens* is their ability to transfer electrons [17], which may enable applications in biobased electronics. The first step towards using the pili of *G. sulfurreducens* as a building

material is the mass production of pilin monomers. The successful mass-production of recombinant $PilA_{19}$ monomers and *in-vitro* assembly of conductive pili was discussed in Chapter 3 of this dissertation. The next step was to determine whether recombinant pilin monomers and pili could be interfaced with gold electrodes. This is an important step towards using pilins and pili *from G. sulfurreducens* for the construction of bioelectronic devices.

Several strategies to interface pilin monomers and pili with gold electrodes were investigated. The first strategy used a hydrophobic alkanethiol self-assembled monolayer (SAM) deposited on gold to interact with recombinant $PilA_{19}$ monomers. This strategy was based on the results reported by Audette *et al.* showing that recombinant pilins from *Pseudomonas aeruginosa* strain K122-4 (ΔK122-4) interacted with surface-constrained hydrophobes [48]. In these experiments, *P. aeruginosa* pilins were placed in contact with undecanethiol covalently attached to maleimide-activated microtiter plates. The interaction was monitored immunologically using polyclonal sera generated against the *P. aeruginosa* strain K pili. A concentration-dependent binding of the pilin to the hydrophobe was observed [48]. However, it was unclear whether the pilins were assembled into pili as a result of the interaction with undecanethiol or only physically adsorbed onto the monolayer. The proposed approach is aimed at determining whether the interaction of $PilA_{19}$ subunits with an undecanethiol SAM could trigger self-organization into pili. Cyclic voltammetry and ellipsometry were used to confirm the formation of the alkanethiol monolayer. Scanning electron microscopy was used to determine the assembly of pilin subunits into pili.

To investigate direct interaction between pilin subunits and gold substrates, a cysteine-modified $PilA_{19}$ subunit was engineered. Several studies have shown that cysteine-

functionalized peptides and proteins bind to gold surfaces by interaction with the sulfur atoms. Cysteine forms a strong bond through the interaction of SH groups and Au atoms [107]. The last amino acid at the N-terminus of the $PilA_{19}$ monomer, alanine, was replaced by cysteine (Figure 4.1). The truncation is referred to here as $PilA_{19}$-A20C. $PilA_{19}$-A20C pilins were produced with the same protocol used to express and purify $PilA_{19}$ pilins.

After production of $PilA_{19}$-A20C monomers, interactions between pilin monomers and *in-vitro* assembled pili with gold electrodes were examined using cyclic voltammetry, ellipsometry, quartz crystal microbalance, and scanning electron microscopy. $PilA_{19}$-A20C monomers were assembled into pili using the same protocol successfully demonstrated with $PilA_{19}$ pilins.

4.2. Materials and Methods

4.2.1. Interfacing of Recombinant $PilA_{19}$ Monomer with Gold Electrodes

Gold substrates (LGA Thin Films, Santa Clara, CA) were washed with ethanol, dried under nitrogen, and cleaned by a 30 s immersion in piranha solution (7 parts by volume concentrated sulfuric acid to 3 parts by volume 30% aqueous hydrogen peroxide)[2]. After piranha cleaning, the substrates were washed with copious amounts of DI water and dried under nitrogen. Substrates were incubated for 48 h at room temperature with a 1 mM undecanethiol (Sigma-Aldrich St. Louis, MO) solution in ethanol. Following monolayer formation, the gold substrates

[2] Caution: piranha solution is an extremely strong oxidant and potentially explosive; it must be handled with extreme care.

were washed with ethanol and dried under nitrogen. Formation of undecanethiol monolayer was verified using ellipsometry and cyclic voltammetry.

Monolayer formation was followed by overnight incubation at room temperature with $PilA_{19}$ subunits dissolved in 20 mM sodium phosphate buffer pH 7.0, 100 mM NaCl, with or without 10 mM SDS. To assess the assembly of recombinant pilins into pili, the samples were analyzed using scanning electron microscopy (SEM).

4.2.2. Expression and Purification of Recombinant $PilA_{19}$-A20C Subunits

Since the IMPACT expression system (New England Biolabs Inc., Ipswich, MA) gave the best results for production of $PilA_{19}$ subunits, this system was used to produce the cysteine-modified pilin. The pilin was expressed as a fusion of a chitin binding domain tag (CBD-$PilA_{19}$-A20C). Plasmid was transformed into DH5α *E. coli* cells for propagation. Sequence of the expression plasmid was confirmed before transforming into competent *E. coli* strain Rosetta2 DE3 p(LysS). The expression was carried out in a 10 L batch reactor (Bioflo 3000, New Brunswick Scientific, Edison, NJ). A detailed protocol for using this batch system is given in section 3.2.2 of this dissertation. Briefly, 5 L of yeast-enriched HM media containing trace elements, 100 μg/mL ampicilin, and 34 μg/mL chloramphenicol, was inoculated. Cells were grown overnight at 37^{o}C with periodic additions of 50% (w/v) glucose and 20 g/L $MgSO_4$. The pH was set to 7.0 and the dissolved oxygen (DO) was kept at 10%. Expression of the recombinant protein was induced with 0.5 mM IPTG and the temperature was lowered to 30^{o}C. Six hours after induction, the cells were harvested by centrifugation at 5000 x g for 20 min at

4^{o}C. The cell pellet was stored at -70^{o}C. Expression of the fusion protein was tested by SDS-PAGE and western blot.

The $PilA_{19}$-A20C monomers were purified by affinity chromatography using chitin beads. All the buffers used during purification are shown in Table 3.3. Harvested cells were re-suspended in a lysis buffer (10 mL of buffer per gram of cells) and lysed using a tip sonicator (Sonifier 250, Branson, Danbury, CT). The crude extract was sonicated on ice 7 times for 10 s, and the cell extract was clarified by centrifugation at 20,000 x g for 30 minutes at 4^{o}C. The supernatant was loaded into the chitin affinity column to allow binding of the target protein. Non-specifically bound proteins were removed from the column by increasing the concentration of NaCl in the washing buffer. The CBD was cleaved from the $PilA_{19}$-A20C pilin by rinsing the column with 3 column volumes of incubation buffer containing 50 mM DTT. The column was then incubated for 40 hours at room temperature. The $PilA_{19}$-A20C monomers were eluted from the column with a storage buffer. The production of pilin subunits was confirmed by SDS-PAGE, and MALDI-TOF mass spectrometry. For experimental details regarding SDS-PAGE, western blot, and MALDI-TOF analysis refer to sections 3.2.4, 3.2.5 and 3.2.6 of this dissertation.

4.2.3. Interfacing Recombinant $PilA_{19}$-A20C Pilins with Gold Electrodes

Clean gold substrates (see section 4.2.1) were incubated overnight with a solution containing $PilA_{19}$-A20C subunits. After incubation, samples were analyzed using ellipsometry, cyclic voltammetry (CV), and scanning electron microscopy (SEM). The deposition of $PilA_{19}$-

A20C monomers on the gold electrode was monitored in real time using quartz crystal microbalance (QCM).

4.2.4. Interfacing Recombinant $PilA_{19}$-A20C Fibers with Gold Electrodes

In-vitro assembly of $PilA_{19}$-A20C subunits in solution was carried out with the same protocol used with the $PilA_{19}$ monomers. Cysteine-modified subunits were exchanged from buffer to an organic solvent, followed by complete evaporation of the solvent, and re-suspension of the dry pellet in DI water. Oasis MAX extraction cartridges, 60 mg sorbent (Waters Corporation, Milford, MA) were used to exchange the pilins from buffer to organic solvent. The column was wetted with 1 mL of 100% acetonitrile, followed by 1 mL wash with DI water. Before loading, the pH of the protein solution was adjusted above 10 with 1 mM NaOH. Approximately 2 mL of buffer containing pilin was passed through the column. The column was washed with 1 mL solution of 5% NH_4OH. The pilin was eluted with 1 mL solution of 20% methanol and 80% acetonitrile. The organic solvent mixture was removed using a roto-evaporator. After pellet re-suspension in DI water, TEM was used to confirm the formation of cysteine-modified pili.

Following assembly, the cysteine-modified pili were brought into contact with a gold substrate. To shorten the micron long fibers, pili-containing samples were sonicated over three different periods for comparison (5 min, 30 min, and 1 hour). After overnight incubation with the pili samples, the gold substrates were analyzed using SEM.

4.2.5. Ellipsometry

Film thicknesses were determined using an M-44 rotating analyzer ellipsometer (J.A. Woollam Co., Inc., Lincoln, NE) controlled by WVASE32 software. The incident angle was set at 75^{o} using 44 wavelengths of light between 414.0 and 736.1 nm. The refractive index (n) and extinction coefficient (k) were assumed to be n = 1.5 and k = 0, respectively, for determination of all thicknesses. Thickness measurements were performed on at least 3 spots on each substrate and then averaged.

4.2.6. Scanning Electron Microscopy (SEM)

To prepare samples for SEM, the gold substrates were gently washed and dried by either critical point drying or freeze-drying. In critical point drying, the water in the sample is first replaced by a dehydration fluid. The samples were dehydrated by incubation in a graded ethanol series (25%, 50%, 75%, 95%) for 20 min at each concentration, followed by three 10 min changes in 100% ethanol. Samples were dried in a Balzers Model 010 critical point dryer (Balzers Union Ltd., Balzers, Liechtenstein) using liquid carbon dioxide as transitional fluid. Samples for freeze-drying were first frozen in liquid nitrogen, then water was sublimated during an 18 h cycle in an EMS 750 freeze dryer (Electron Microscopy Sciences, Hatfield, PA). After drying, samples were mounted on SEM stubs and coated with a thin layer (~ 2 nm) of osmium using a NEOC-AT pure osmium coater (Meiwa Shoji CO. Ltd., Osaka, Japan).

Scanning electron microscopy was performed using the secondary electron imaging (SEI) detector of a JSM 7500F with cold field emission electron emitter SEM (JEOL Ltd., Tokyo, Japan). An accelerating voltage of 5 kV or less was used for imaging. Energy dispersive X-ray (EDS) microanalysis coupled to the SEM was used for elemental analysis. EDS was done using

an Oxford Instruments INCA system (Oxford Instruments, High Wycomb, Bucks, England), software version 14.3, using a 30 mm^2 detector crystal and an ultrathin window. An accelerating voltage of 1 kV was used to avoid excitation of gold characteristic X-ray lines during EDS characterization.

4.2.7. Cyclic Voltammetry (CV)

In cyclic voltammetry, the potential of the working electrode is cycled between two values at a specific scan rate, and the current produced by the electron transfer process is measured [108]. The cyclic voltammogram of a clean electrode in the presence of a redox couple will display a characteristic duck shape with well-defined reduction and oxidation peaks. The formation of a SAM on the electrode can be studied using CV. A defect free monolayer acts as an insulating barrier that hinders electron transfer at the electrode surface, so no reduction or oxidation peaks would be observed. However, pinholes or defects in the monolayer would allow access of redox species to the electrode surface.

A conventional three-electrode cell consisting of the gold-modified working electrode, a platinum auxiliary electrode, and a silver/silver chloride (Ag/AgCl) reference electrode was used for electrochemical measurements. Cyclic voltammetry (CV) was performed using a CHI660 potentiostat (CH Instruments, Austin, TX). Measurements were carried out in 100 mM phosphate buffer at pH 7.0, containing 100 mM NaCl and 5 mM potassium ferricyanide ($K_3[Fe(CN)_6]$).

4.2.8. Quartz Crystal Microbalance (QCM)

Quartz crystal microbalance (QCM) is a very sensitive technique used to study formation of films on surfaces in real time [109, 110]. It takes advantage of the piezoelectric properties of quartz crystals and the relationship between the frequency of oscillation and the mass of deposited material [110]. A research quartz crystal microbalance (RQCM, Inficon, East Syracuse, NY) controlled by a RQCM logging data system was used to monitor crystal frequency (*f*) changes due to the deposition of $PilA_{19}$-A20C monomers on the gold substrate. Changes in viscoelastic properties of the adsorbed mass are reflected in changes of the dissipated energy (*D*), which was calculated from the measured resistance (*R*), using the following equation [109, 110]:

$$D = \frac{32 f_f^2 Z_q d_q^2 RA}{\pi} \tag{4.1}$$

where f_f is the fundamental frequency of the quartz crystal (5×10^6 Hz), Z_q is the acoustic impedance for AT-cut quartz (8.8×10^6 kg m^2 s^{-1}), d_q is the piezoelectric strain coefficient for AT-cut quartz (3.1×10^{-12} m V^{-1}), and *A* is the electrode area (34.19 mm^2). The RQCM was equipped with a 0.1 mL flow cell and an AT-cut polished sensing crystal, 5 MHz Ti/Au (Inficon, East Syracuse, NY). A PHD standard infusion syringe pump (Harvard Apparatus, Holliston, MA) was used to fill the flow cell with buffer (10 mM potassium phosphate buffer pH 7.0 with 50 mM Na_2SO_4). After equilibration of the crystal, the $PilA_{19}$-A20C monomers were introduced into the flow cell at a flow rate of 0.2 mL/min and changes in frequency and resistance were monitored.

4.3. Results and Discussion

4.3.1. Interfacing Recombinant $PilA_{19}$ Monomers with Gold Electrodes

Interaction of recombinant pilins from *P. aeruginosa* in solution with undecanethiol has been reported to trigger assembly of the subunits into pili [48]. The goal in this work was to determine whether a hydrophobic SAM deposited on a gold electrode could trigger assembly of recombinant $PilA_{19}$ subunits into pili. The formation of the undecanethiol monolayer on gold was confirmed by cyclic voltammetry and ellipsometry. Figure 4.2 shows the CV curves for bare gold and the undecanethiol SAM. The bare gold voltammogram shows the characteristic duck shape with well-defined oxidation and reduction peaks. The CV curve for the SAM shows a significant decrease in current with no distinctive peaks, indicating that the monolayer acts as an insulating barrier that blocks electron transfer between the electroactive species in solution and the electrode. Ellipsometry results showed a monolayer thickness of 11.90 ± 0.720 Å (see insert of Figure 4.2), consistent with values reported in literature [111].

Formation of the undecanethiol SAM on the gold substrate was followed by incubation with $PilA_{19}$ monomers in buffer solution with and without SDS. After incubation with the pilin subunits, the substrates were gently washed and the remaining solution was removed by freeze-drying. Samples were analyzed by SEM to determine whether the interaction with the hydrophobic monolayer would trigger assembly of pilin subunits into pili.

SEM analysis of samples incubated with $PilA_{19}$ monomers in buffer without SDS did not show formation of any defined structures. Samples incubated with $PilA_{19}$ subunits in buffer containing 10 mM SDS showed areas where horizontal fiber-like structures were observed on the

surface (Figure 4.3). The filaments were not evenly distributed on the gold surface. Energy dispersive X-ray spectroscopy (EDS) was used to determine the elements present in these fibers. An accelerating voltage of 1 kV was used to avoid excitation of gold X-ray characteristic lines, which would make it extremely difficult to identify other elements present in the sample. The EDS data shown in Figure 4.4 indicated that the carbon content was higher on the fiber than on the gold substrate.

Based on the available results, it was not possible to conclude whether the fibers imaged using SEM correspond to pilin subunits assembled into pili. It has been reported that SDS can form various structures when adsorbed onto a hydrophobic surface or monolayer [112, 113]. A relation between the concentration of SDS and the resulting structures has been observed [113]. AFM images have shown that SDS adsorbed onto a hydrophobic monolayer form poorly-defined aggregates at concentrations close to the CMC (8.1 mM), whereas long parallel aggregates believed to be hemi-micellar structures are formed at concentrations well above the CMC (100 mM) [113]. The SDS concentration used in our experiments was 10 mM, which is above the CMC. The increase in carbon content could be attributed to either a proteinaceous structure (pili) or an SDS structure. For example, the structures observed in SEM images could be the result of SDS forming aggregates upon interaction with the undecanethiol monolayer.

Control experiments could be used in the future to determine whether the observed fibers represent assembled pili or SDS structures. However, even if the fibers are the result of pilin monomers assembled into pili, the protocol used here did not lead to a controlled assembly process. SEM images showed that the surface coverage was not uniform, and fibers of various lengths were formed.

4.3.2. Production of Cysteine-Modified Recombinant Pilin: $PilA_{19}$-A20C

To facilitate the interfacing of pilin monomers with gold substrates, a cysteine-modified subunit was engineered. The $PilA_{19}$-A20C monomer is a 19 amino acid truncation of the full length pilin of *Geobacter sulfurreducens*, where the last amino acid at the N-terminal end, alanine, was substituted with a cysteine (Figure 4.1). The $PilA_{19}$-A20C subunit was expressed as a fusion protein with a chitin-binding domain (CBD-$PilA_{19}$-A20C). The purification of the recombinant pilin was performed by affinity chromatography using chitin beads.

Figure 4.5 shows SDS-PAGE and MALDI-TOF results that demonstrate the successful production of recombinant cysteine-modified subunit ($PilA_{19}$-A20C). SDS-PAGE results confirmed the expression of the CBD-$PilA_{19}$-A20C fusion, based on the appearance of a strong band at ~65 kDa after induction. Western blot analysis was positive when using an anti-chitin antibody. Insert c in the figure corresponds to a tricine gel showing the two bands in the elution fraction after purification. The elution fraction was analyzed by MALDI-TOF mass spectrometry (Figure 4.5b), with the peak at 4,632.26 Da confirming the production of $PilA_{19}$-A20C subunits. The theoretical molecular weight of the $PilA_{19}$-A20C monomer is 4,627.08 Da. The peak at 6,218.5 Da is likely a non-specifically bound protein that was not removed from the column during the washing step. The peak at 1,606.94 Da does not show on the tricine gel because of the low molecular weight and corresponds to an additional peptide that is cleaved from the fusion.

4.3.3. Interfacing Recombinant $PilA_{19}$-A20C Pilins with Gold Electrodes

Several characterization techniques were used to investigate the interaction between the cysteine-modified subunits and the gold substrates. The results suggested the formation of a monolayer of $PilA_{19}$-A20C subunits on the gold surface. Figure 4.6 shows QCM results obtained during the deposition of cysteine-modified pilins on a gold electrode. The arrow pointing down indicates the time when the protein solution was introduced into the flow cell. The arrow pointing up indicates the time when the syringe pump was stopped. There is a perturbation associated with the stoppage of the flow, which is probably thermally related, as it is present in both the frequency and dissipation curves. The frequency shift after the introduction of the pilin subunits is associated with a change in mass indicating the adsorption of pilin monomers on the gold electrode. The dissipation change is related to the presence of protein on the QCM crystal that is coupling more strongly to the fluid. A bare QCM crystal will not couple strongly to the fluid surrounding it, but the protein will. As more protein is deposited on the crystal, the sum of the protein-fluid interactions increases, and the dissipative contribution to the QCM signal increases as a result.

Ellipsometry measurements indicated the formation of a film with a thickness of 35.582 ± 9.110 Å (insert of Figure 4.7). The dimensions of a full length PilA (61 amino acid residues) from *Geobacter sulfurreducens* are approximately 80 Å in length and 1 Å in diameter. For the cysteine-modified truncation (42 amino acid residues), a length of roughly 55 Å would be expected. The thickness obtained by ellipsometry is about 65% of the expected length, which would suggest that the subunits arranged themselves at a particular tilt angle with respect to the surface normal. As reference, the tilt angle of an alkanethiol SAM is typically around 30 degrees

[111]. The film thickness and the lack of any structures under SEM examination suggest that the assembly of pilin monomers into pili did not occur.

Figure 4.7 shows CV curves of a bare gold surface, and a gold substrate incubated overnight with pilin subunits. Both curves display the characteristic duck shape with distinctive oxidation and reduction peaks. There is a decrease in current density after incubation with pilin subunits which, when compared to the bare gold substrate, would indicate a more insulating surface. Based on the CV, QCM and ellipsometry results, this change in current flow can be directly attributed to some coverage of pilin subunits on the gold substrate. However, the CV data cannot be used to unambiguously address the question of whether the pilins are conductive or not, primarly because there is no information on the uniformity of surface coverage. Thus, there are four possible interpretations of the data. If the surface coverage is uniform, then the pilins may be one of two things:

a) conductive species whose structural motif hinders ion transport to some extent; or
b) insulators that are thinner or less effective than, say, alkanethiol monolayers.

If the surface coverage is not uniform, then two other interpretations are possible. The pilins may be:

c) insulators that formed an imperfect monolayer that does not completely block electron transport; or
d) conductive but not to the same extent as the underlying gold substrate.

The pilus of *G. sulfurreducens* is highly conductive. Also, it was shown in Chapter 3 of this dissertation that recombinant $PilA_{19}$ fibers are conductive. While it has not been established that the pilins of *G. sulfurreducens* are conductive, electrical studies have shown that peptides with α-helical structures are efficient mediators of electron transfer [114, 115]. Considering that

pilins of *G. sulfurreducens* are α-helical peptides that assemble to form a conductive pilus, it is conceivable that a monolayer of pilin subunits would also be conductive. Our group is planning future studies to elucidate this.

4.3.4. Interfacing Recombinant $PilA_{19}$-A20C Fibers with Gold Electrodes

The interaction of $PilA_{19}$-A20C fibers with gold electrodes was also investigated. To assemble the $PilA_{19}$-A20C subunits into pili, we used the same strategy successfully applied to the $PilA_{19}$ subunits. The procedure has three main steps: exchange of the purified pilin monomers from aqueous to organic solvent, roto-evaporation of the organic solvent, and re-suspension of the dry pellet in water. Figure 4.8 shows TEM images of the microns long hair-like fibers that were formed after following this procedure. We hypothesized that several factors may have triggered pilin assembly including 1) the lack of buffer, salt, or detergent to stabilize the peptide solution, 2) the peptide solubility being exceeded, and 3) the presence of an air-water interface. The formation of fibers after the addition of a cysteine at the pilin N-terminal end is an indication that the assembly of pilin monomers into pili may tolerate certain modifications in sequence.

Each fiber formed should have a cysteine at the N-terminus that could interact with the gold surface. The cysteine-modified pili fibers were subjected to sonication prior to contact with the gold substrate to shorten the filaments. Three different sonication times were investigated: 1 min (tip sonicator), 30 min (bath sonicator), and 1 h (bath sonicator). After sonication, the gold substrates were interacted with the previously sonicated pili containing solutions. Under SEM analysis, none of the samples showed any evidence of attachment of the cysteine-modified pili to

the gold substrate. We speculated that the cysteine might be buried in the core of the helical fiber and not exposed to the gold substrate.

4.4. Conclusions

Several strategies were investigated in an attempt to interface pilin subunits with gold substrates. The first strategy was to use a hydrophobic monolayer to trigger assembly of the recombinant $PilA_{19}$ monomers. Some fiber formation was observed when the pilin monomers were dissolved in buffer containing SDS. However, this assembly scheme lacked control as the surface coverage was not uniform and fibers of various lengths were observed. In addition, it cannot be ruled out that the fibers observed were formed by SDS interacting with the hydrophobic monolayer.

A cysteine-modified pilin monomer ($PilA_{19}$-A20C) was expressed as a fusion using a chitin binding domain and purified using affinity chromatography. The $PilA_{19}$-A20C subunits formed a monolayer when they interacted with gold substrates. $PilA_{19}$-A20C subunits were assembled *in-vitro*, indicating that pilin assembly tolerates certain changes in amino acid sequence. The lack of attachment of cysteine-modified pili to the gold substrates suggests that the cysteine at the N-terminal end of the fiber is buried inside the helical core and not available for interaction with the gold substrate.

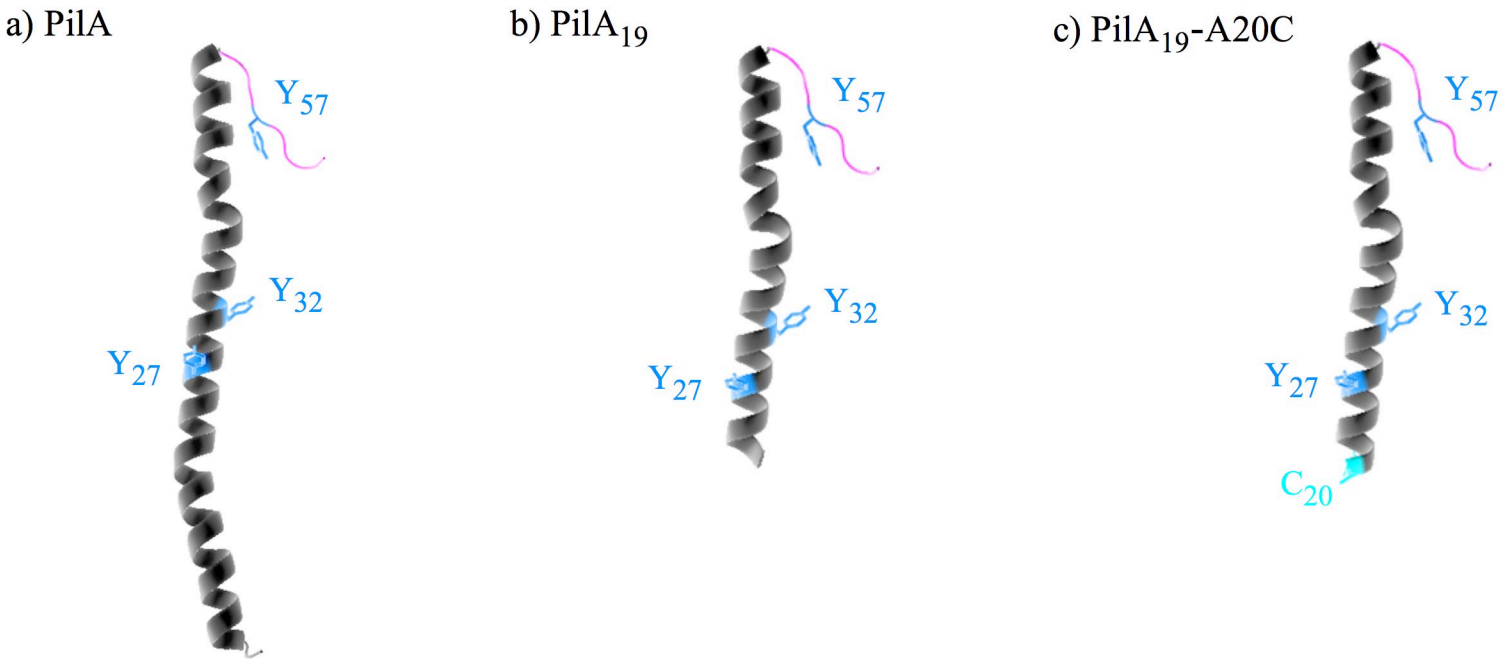

d) sequence alignment

```
                                10        20        30        40        50        60
                                |         |         |         |         |         |
PilA/1-61          FTLIELLIVVAIIGILAAIAIPQFSAYRVKAYNSAASSDLRNLKTALESAFADDQTYPPES
PilA19/1-42        ------------------AIPQFSAYRVKAYNSAASSDLRNLKTALESAFADDQTYPPES
PilA19-A20C/1-42   ------------------CIPQFSAYRVKAYNSAASSDLRNLKTALESAFADDQTYPPES
```

Figure 4.1 Structural comparisons of wild type and recombinant pilins of *Geobacter sulfurreducens.* Structure of a) wild type PilA protein; b) recombinant 19 amino acid truncation $PilA_{19}$ protein; c) recombinant cysteine-modified 19 amino acid truncation $PilA_{19}$-A20C protein, with the added cysteine colored turquoise. In each structure, the tyrosines are colored light blue. d) Sequence alignment of wild type and recombinant pilins of *Geobacter sulfurreducens.*

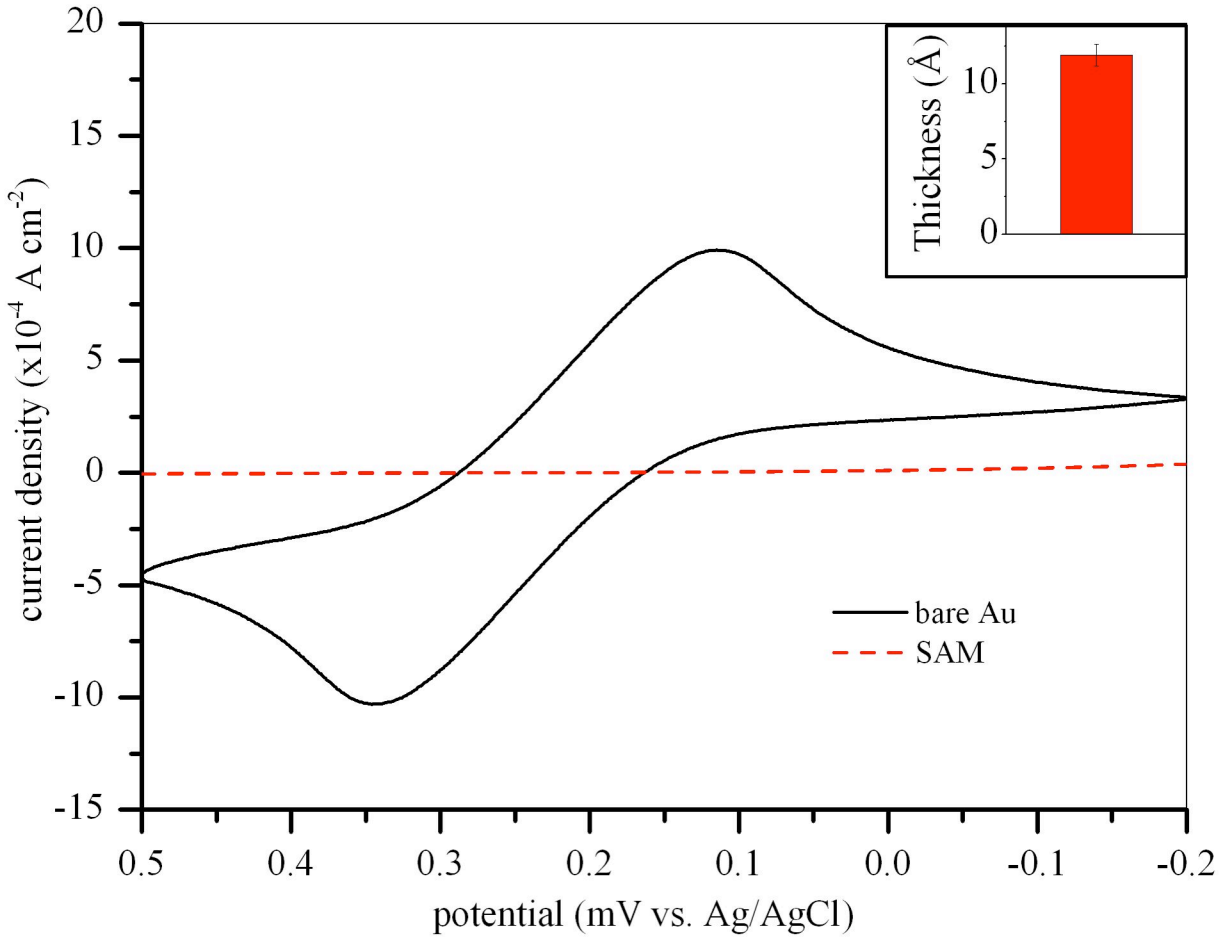

Figure 4.2 Formation of an undecanethiol self-assembled monolayer on a gold electrode. Cyclic voltammograms of bare gold (black line) and undecanethiol SAM (red dashed line). Data recorded at room temperature in 100 mM sodium phosphate buffer at pH 7.0 containing100 mM NaCl, and 5 mM $K_3[Fe(CN)_6]$ at a potential scan rate of 100 mV s^{-1}. The insert shows the thickness of the undecanethiol monolayer measured by ellipsometry.

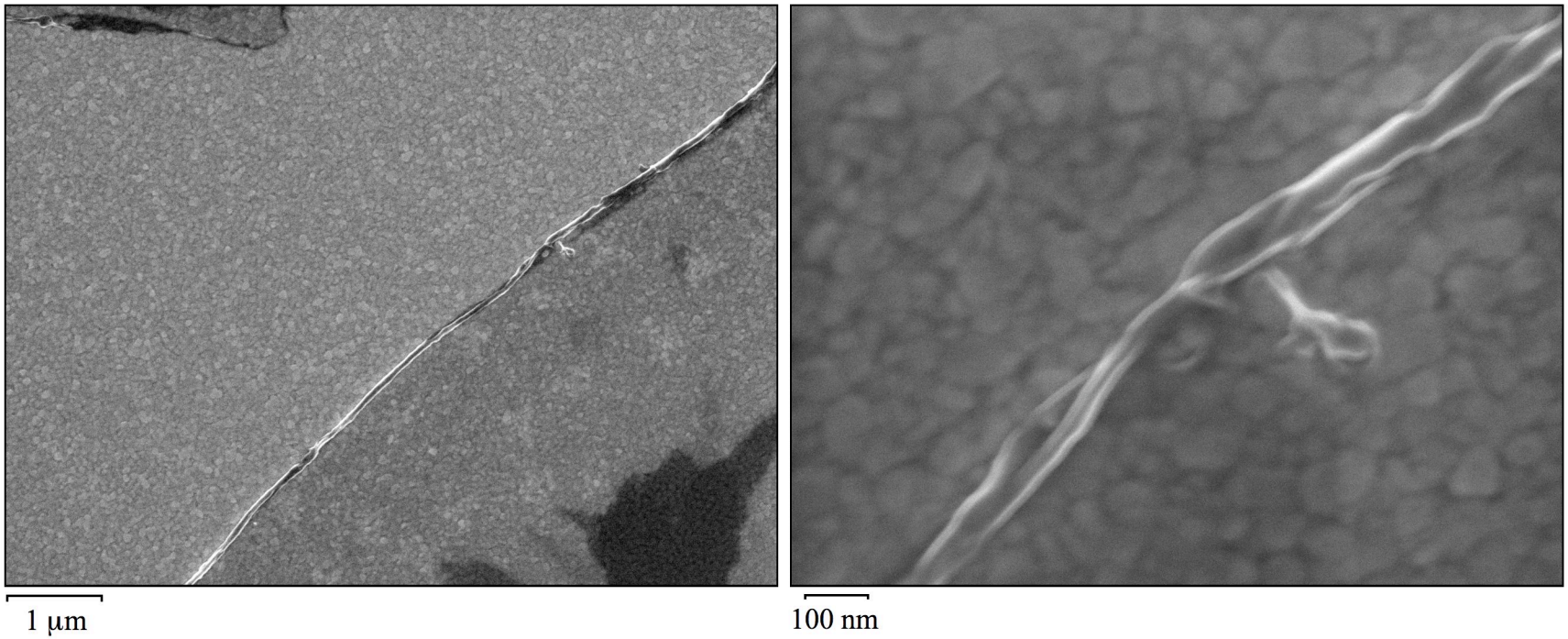

Figure 4.3 Scanning electron microscopy images of gold substrates after deposition of an undecanethiol SAM followed by incubation with $PilA_{19}$ monomers in 20 mM sodium phosphate pH 7.0, 100 mM NaCl, 10 mM SDS. Accelerating voltage 5 kV.

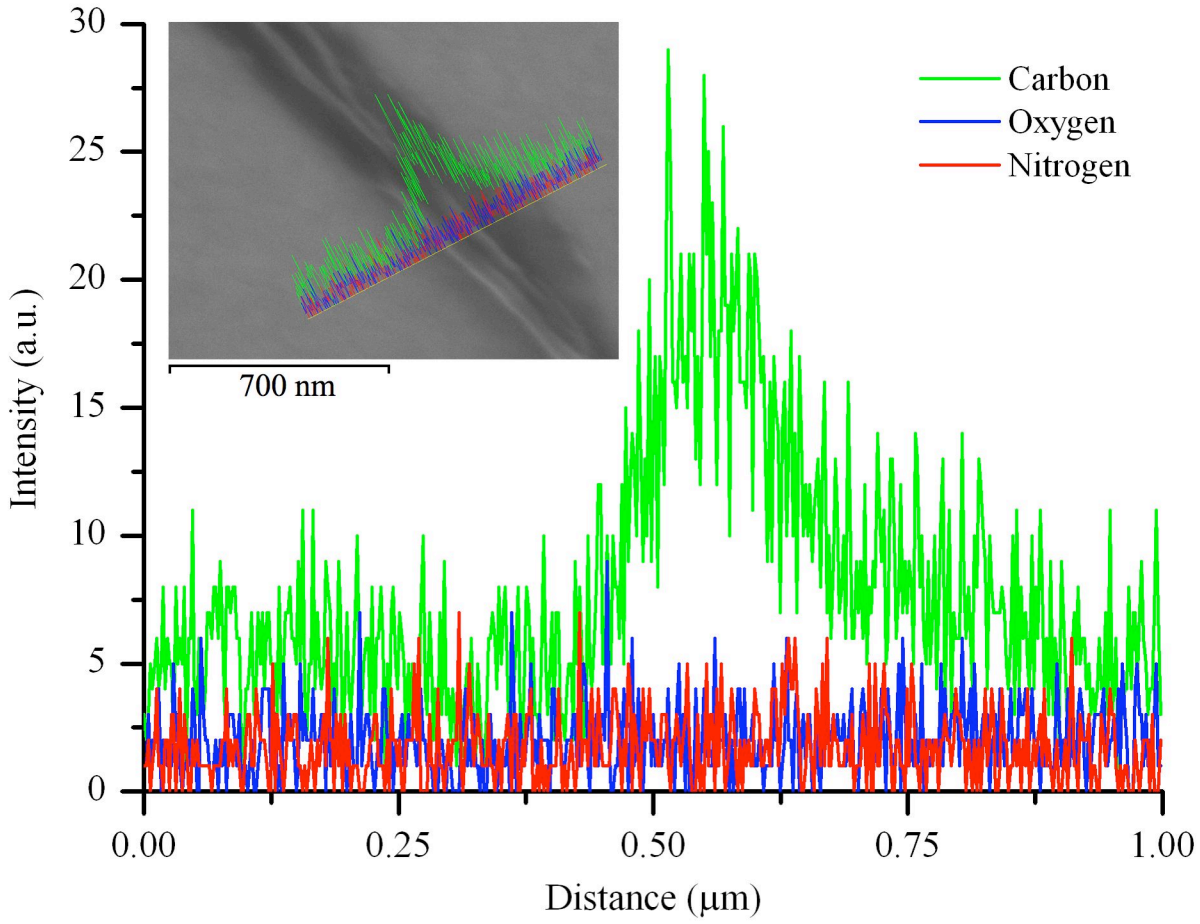

Figure 4.4 Energy Dispersive X-ray (EDS) microanalysis of fibers present on gold substrates modified by deposition of an undecanethiol SAM, followed by incubation with $PilA_{19}$ monomers in 20 mM sodium phosphate pH 7.0, 100 mM NaCl, 10 mM SDS. Accelerating voltage 1 kV.

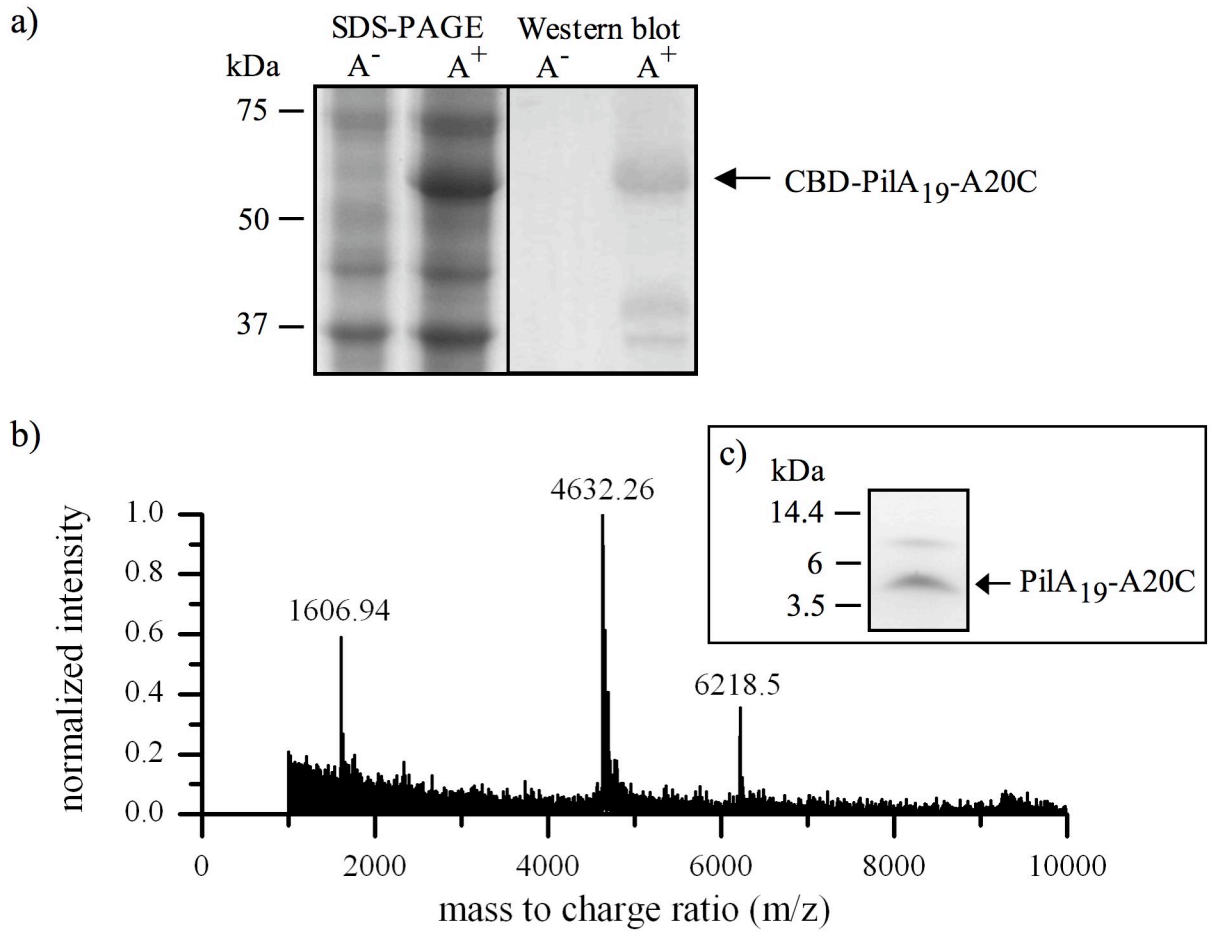

Figure 4.5 Expression and purification of recombinant $PilA_{19}$-A20C subunits: a) 12% SDS-PAGE and western blot analysis of cells before (A^-) and after (A^+) induction. Anti-chitin serum was used for western blot. b) MALDI-TOF mass spectrometry and c) 10-20% tricine gel of elution fraction after purification.

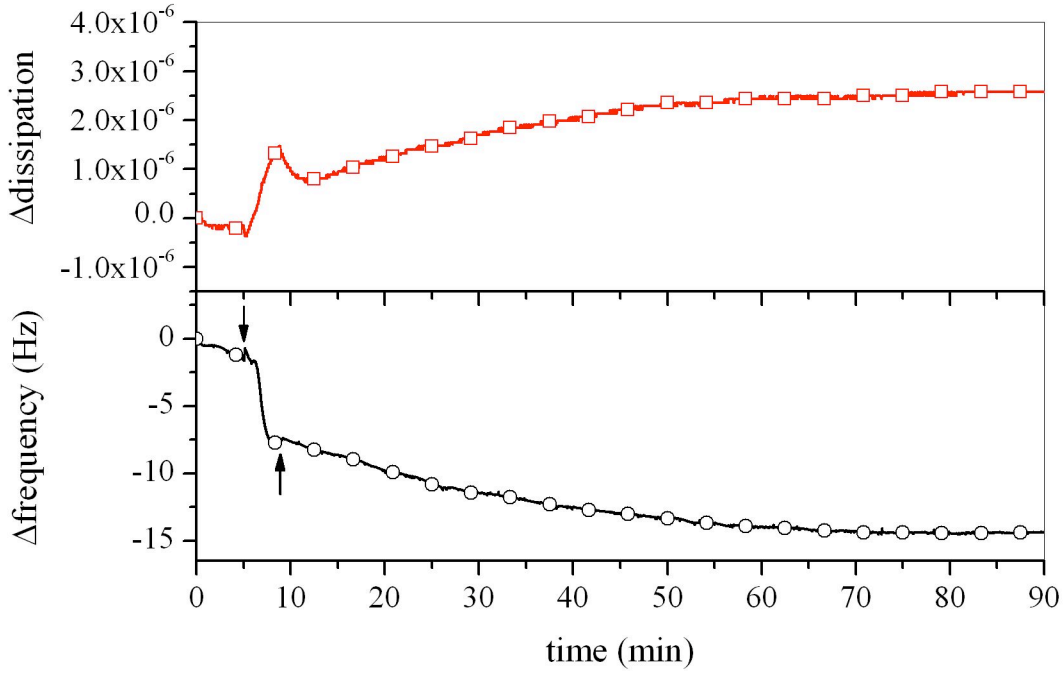

Figure 4.6 Deposition of $PilA_{19}$-A20C monomers on a gold electrode. Quartz crystal microbalance (QCM) was used to monitor changes in frequency and dissipated energy after the addition of pilin monomers.

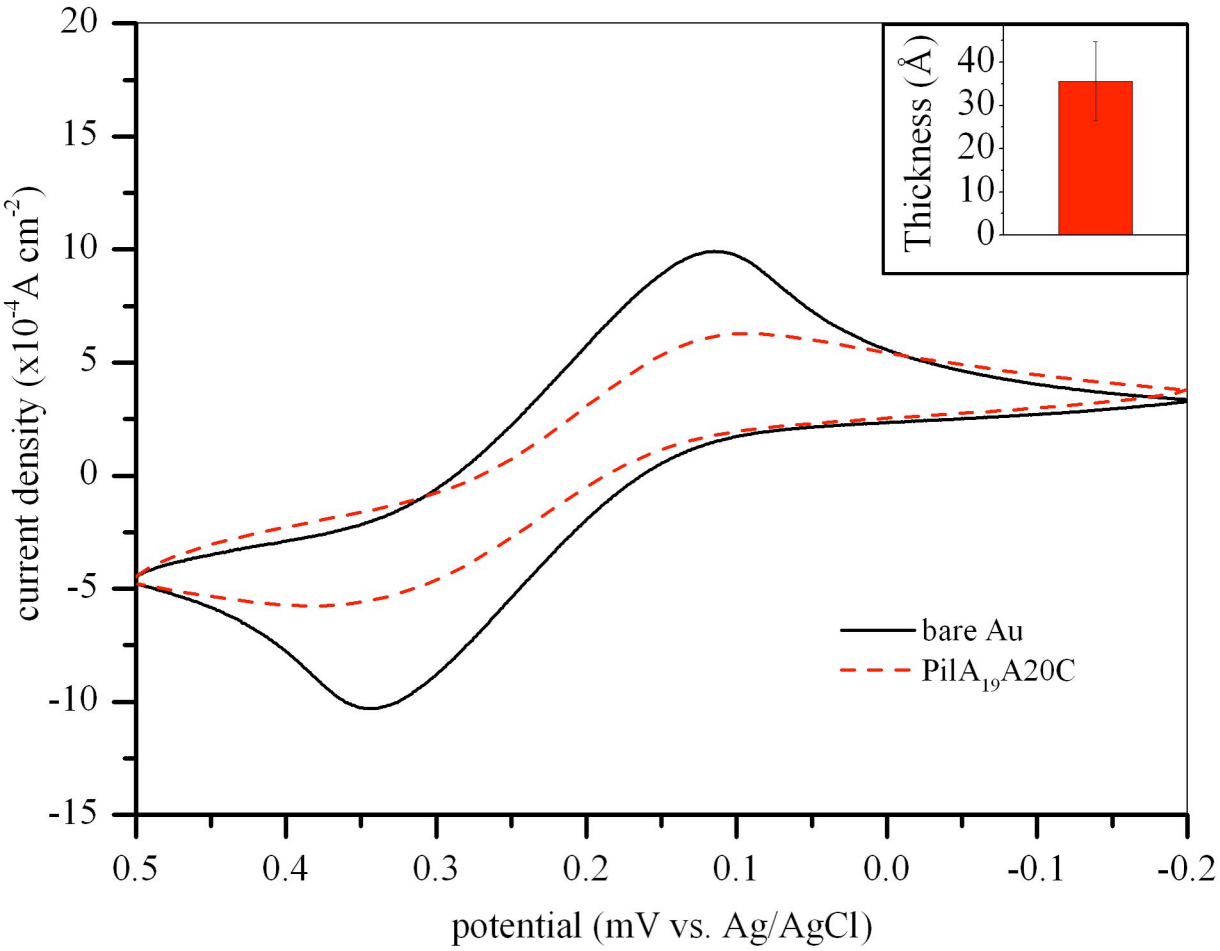

Figure 4.7 Deposition of PilA$_{19}$-A20C subunits on a gold electrode. Cyclic voltammograms of bare gold (black line) and undecanethiol SAM (red dashed line). Data recorded at room temperature in 100 mM sodium phosphate buffer at pH 7.0 containing 100 mM NaCl, and 5 mM $K_3[Fe(CN)_6]$ at a potential scan rate of 100 mV s^{-1}. Insert shows the thickness of PilA$_{19}$-A20C monolayer measured by ellipsometry.

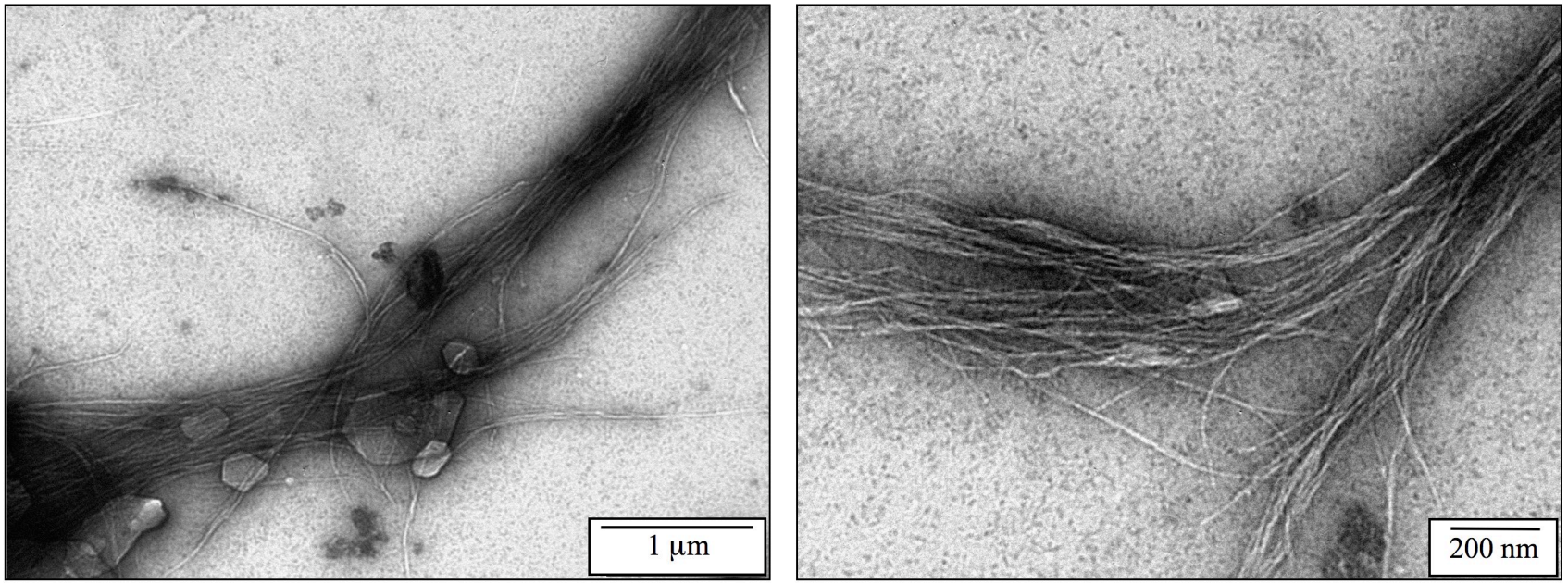

Figure 4.8 *In-vitro* assembly of $PilA_{19}$-A20C fibers. The transmission electron microscopy images were collected at an accelerating voltage of 100 kV.

Chapter 5.

CONCLUSIONS

The properties of self-assembling biological molecules can be exploited for bottom-up fabrication of well-defined nanostructured materials. This dissertation focused on two biomolecules: phospholipids and self-organizing peptides. Phospholipids assemble into an array of structures (vesicles, bilayers and micelles) that serve as models for cell membranes. Peptides are versatile building blocks with extensive chemical, conformational and functional diversity. The objectives of this study were to 1) assess the influence of the method of liposome preparation on selected properties of lipid bilayers, and 2) harness the self-organizing properties of a special class of peptides to produce synthetic protein nanowires.

To fulfill the first objective, the effect of the method of liposome preparation (sonication or extrusion) on bilayer properties was investigated. The results indicated that the morphology, average size, and size distribution of liposomes depends on the method of preparation. However, the molecular-scale behavior of the liposomes, as studied by fluorescence lifetime and anisotropy decay measurements, was independent of the method of preparation. In addition, translational diffusion of sBLMs reconstituted from liposomes was also independent of the method of

liposome preparation. The presence of cholesterol in the bilayers decreased membrane fluidity in both systems. The results indicate that the molecular scale organization of lipid bilayers is determined by interactions between the constituent species, which does not depend on the manner in which the bilayer is formed. Consequently, studies on lipid bilayers produced from liposomes prepared either by sonication or extrusion can be directly compared.

To fulfill the second objective, the investigation focused on the conductive, hair-like protein appendages or pili produced by the metal-reducing bacterium *Geobacter sulfurreducens*. A combination of genetic engineering and heterologous protein expression was used to mass-produce the recombinant pilin subunits. The highly hydrophobic nature of the pilin subunits made their expression as soluble peptides very challenging. Therefore, step-wise deletions of amino acids from the hydrophobic N-terminus were carried out to produce truncated pilins. The $PilA_{19}$ subunit was the shortest truncation (longest pilin) expressed as a soluble peptide. The secondary structure of the $PilA_{19}$ monomer was characterized using circular dichroism. The results showed that the addition of surfactants such as SDS and octyl β-D-glucopyranoside increased the helical content of the subunits. The assembly of type IV pilins is mediated by interactions between the N-terminal α-helices of the pilin subunits. *In-vitro* assembly of the recombinant pilins resulted in the formation of filaments with properties similar to those of native *G. sulfurreducens* pili, including a similar diameter, tendency to aggregate in tangled bundles, and electrical conductivity. Therefore, deletion of 19 amino acids from the N-terminal end did not significantly affect the self-assembly process or the conductivity of the synthetic pili.

In an attempt to facilitate interfacing of recombinant subunits with gold electrodes, a cysteine-modified pilin was engineered ($PilA_{19}$-A20C), expressed and purified. The results

indicated that, while the $PilA_{19}$-A20 monomers form a monolayer, they do not assemble into pili on the gold substrate. However, the $PilA_{19}$-A20C subunits self-assembled into pilus-like filaments in solution, indicating that pilin assembly can tolerate some changes in amino acid sequence.

The net recombinant expression, purification, and self-assembly of soluble pilin subunits from *Geobacter sulfurreducens* could facilitate structural studies of PilA peptides and enable application of these versatile structures in nanoelectronics. Conductive, protein nanowires represent a new platform for design of novel biomimetic interfaces suitable for scientific investigations of electron transfer mechanisms in *Geobacter* species, as well as development of new technologies.

REFERENCES

REFERENCES

1. Choi, J.W., et al., *Nanotechnology in biodevices.* J Microbiol Biotechnol, 2007. **17**(1): p. 5-14.

2. Villaverde, A., *Nanotechnology, bionanotechnology and microbial cell factories.* Microbial Cell Factories, 2010. **9**: p. 4.

3. Dirks, A.J., et al., *From (bio)molecules to biohybrid materials with the click chemistry approach.* Qsar & Combinatorial Science, 2007. **26**(11-12): p. 1200-1210.

4. de la Rica, R. and H. Matsui, *Applications of peptide and protein-based materials in bionanotechnology.* Chemical Society Reviews, 2010. **39**(9): p. 3499-3509.

5. Wu, L.-Q. and G.F. Payne, *Biofabrication: using biological materials and biocatalysts to construct nanostructured assemblies.* Trends in Biotechnology, 2004. **22**(11): p. 593-599.

6. Whitesides, G.M., *The 'right' size in nanobiotechnology.* Nat Biotech, 2003. **21**(10): p. 1161-1165.

7. Ball, P., *Synthetic biology for nanotechnology.* Nanotechnology, 2005. **16**(1): p. R1.

8. Reimhult, E., F. Höök, and B. Kasemo, *Temperature dependence of formation of a supported phospholipid bilayer from vesicles on SiO2.* Phys Rev E Stat Nonlin Soft Matter Phys, 2002. **66**(5 Pt 1): p. 051905.

9. Keller, C.A., et al., *Formation of supported membranes from vesicles.* Phys Rev Lett, 2000. **84**(23): p. 5443-6.

10. Keller, C.A. and B. Kasemo, *Surface specific kinetics of lipid vesicle adsorption measured with a quartz crystal microbalance.* Biophys J, 1998. **75**(3): p. 1397-1402.

11. Cui, H., M.J. Webber, and S.I. Stupp, *Self-assembly of peptide amphiphiles: From molecules to nanostructures to biomaterials.* Peptide Science, 2010. **94**(1): p. 1-18.

12. Reimhult, E., F. Hook, and B. Kasemo, *Vesicle adsorption on SiO2 and TiO2: Dependence on vesicle size.* Journal of Chemical Physics, 2002. **117**(16): p. 7401-7404.

13. Hope, M.J., et al., *Generation of multilamellar and unilamellar phospholipid vesicles.* Chemistry and Physics of Lipids, 1986. **40**(2-4): p. 89-107.

14. Weiner, N., *Phospholipid Liposomes: Properties and Potential Use in Flavor Encapsulation*, in *Flavor Technology*. 1997, American Chemical Society. p. 210-218.

15. Oliger, P., et al., *Preparation and Properties of Vesicles Formed from Phospholipid Analogues of N-(Phosphonoacetyl)-L-aspartate (PALA) by Sonication or Extrusion: Transition Temperature, Particle Size, Glucose Entrapment, and 31P NMR.* Langmuir, 2001. **17**(21): p. 6426-6432.

16. Lasic, D.D., *The mechanism of vesicle formation.* Biochem. J., 1988. **256**(1): p. 1-11.

17. Reguera, G., et al., *Extracellular electron transfer via microbial nanowires.* Nature, 2005. **435**(7045): p. 1098-101.

18. Collinson, S.K., et al., *Purification and characterization of thin, aggregative fimbriae from Salmonella enteritidis.* J. Bacteriol., 1991. **173**(15): p. 4773-4781.

19. Craig, L. and J. Li, *Type IV pili: paradoxes in form and function.* Curr Opin Struct Biol, 2008. **18**(2): p. 267-77.

20. Craig, L., et al., *Type IV Pilus Structure by Cryo-Electron Microscopy and Crystallography: Implications for Pilus Assembly and Functions.* Molecular Cell, 2006. **23**(5): p. 651-662.

21. Malvankar, N.S., et al., *Tunable metallic-like conductivity in microbial nanowire networks.* Nat Nano, 2011. **6**(9): p. 573-579.

22. Reguera, G., et al., *Biofilm and nanowire production leads to increased current in Geobacter sulfurreducens fuel cells.* Appl Environ Microbiol, 2006. **72**(11): p. 7345-8.

23. Dieckelmann, M., L.F. Roddam, and M.P. Jennings, *Purification of post-translationally modified proteins from bacteria: homologous expression and purification of histidine-tagged pilin from Neisseria meningitidis.* Protein Expr Purif, 2003. **30**(1): p. 69-77.

24. Reimhult, E., F. Höök, and B. Kasemo, *Intact Vesicle Adsorption and Supported Biomembrane Formation from Vesicles in Solution: Influence of Surface Chemistry, Vesicle Size, Temperature, and Osmotic Pressure.* Langmuir, 2002. **19**(5): p. 1681-1691.

25. Seantier, B., et al., *Dissipation-enhanced quartz crystal microbalance studies on the experimental parameters controlling the formation of supported lipid bilayers.* J Phys Chem B, 2005. **109**(46): p. 21755-65.

26. Boxer, S.G., *Molecular transport and organization in supported lipid membranes.* Current Opinion in Chemical Biology, 2000. **4**(6): p. 704-709.

27. Schonherr, H., et al., *Vesicle adsorption and lipid bilayer formation on glass studied by atomic force microscopy.* Langmuir, 2004. **20**(26): p. 11600-6.

28. Richter, R.P. and A.R. Brisson, *Following the formation of supported lipid bilayers on mica: a study combining AFM, QCM-D, and ellipsometry.* Biophys J, 2005. **88**(5): p. 3422-33.

29. Reimhult, E., et al., *A multitechnique study of liposome adsorption on Au and lipid bilayer formation on SiO2.* Langmuir, 2006. **22**(7): p. 3313-3319.

30. *Liposomes methodos and protocols*. 1st edition ed. Methods in molecular biology, ed. S.C. Basu and M. Basu. Vol. 199. 2002, Totawa, NJ: Humana Press Inc.

31. Moon, M.H. and J.C. Giddings, *Size distribution of liposomes by flow field-flow fractionation.* Journal of Pharmaceutical and Biomedical Analysis, 1993. **11**(10): p. 911-920.

32. Carrozzino, J.M., et al., *Characterization of small unilamellar vesicles using solvatochromic π* indicators and particle sizing.* Journal of Biochemical and Biophysical Methods, 2004. **60**(2): p. 97-115.

33. Ma, Z., et al., *Improved method of preparation of supported planar lipid bilayers as artificial membranes for antigen presentation.* Microscopy Research and Technique, 2011. **74**(12): p. 1174-1185.

34. Richter, R., A. Mukhopadhyay, and A. Brisson, *Pathways of lipid vesicle deposition on solid surfaces: A combined QCM-D and AFM study.* Biophysical Journal, 2003. **85**(5): p. 3035-3047.

35. Lovley, D.R., *Cleaning up with genomics: applying molecular biology to bioremediation.* Nat Rev Micro, 2003. **1**(1): p. 35-44.

36. Methe, B.A., et al., *Genome of Geobacter sulfurreducens: Metal Reduction in Subsurface Environments.* Science, 2003. **302**(5652): p. 1967-1969.

37. Juarez, K., et al., *PilR, a Transcriptional Regulator for Pilin and Other Genes Required for Fe(III) Reduction in Geobacter sulfurreducens.* Journal of Molecular Microbiology and Biotechnology, 2009. **16**(3-4): p. 146-158.

38. Reguera, G., et al., *Possible nonconductive role of Geobacter sulfurreducens pilus nanowires in biofilm formation.* J Bacteriol, 2007. **189**(5): p. 2125-7.

39. Juarez, K., et al., *PilR, a transcriptional regulator for pilin and other genes required for Fe(III) reduction in Geobacter sulfurreducens.* J Mol Microbiol Biotechnol, 2009. **16**(3-4): p. 146-58.

40. Sharma, V. and P.P. Kundu, *Biocatalysts in microbial fuel cells.* Enzyme and Microbial Technology, 2011. **47**(5): p. 179-188.

41. Srikanth, S., et al., *Electrochemical characterization of Geobacter sulfurreducens cells immobilized on graphite paper electrodes.* Biotechnology and Bioengineering, 2008. **99**(5): p. 1065-1073.

42. Law, N., et al., *Formation of Nanoscale Elemental Silver Particles via Enzymatic Reduction by Geobacter sulfurreducens.* Appl. Environ. Microbiol., 2008. **74**(22): p. 7090-7093.

43. Cologgi, D.L., et al., *Extracellular reduction of uranium via Geobacter conductive pili as a protective cellular mechanism.* Proceedings of the National Academy of Sciences of the United States of America, 2011. **108**(37): p. 15248-15252.

44. Gregory, K.B. and D.R. Lovley, *Remediation and Recovery of Uranium from Contaminated Subsurface Environments with Electrodes.* Environmental Science & Technology, 2005. **39**(22): p. 8943-8947.

45. Debabov, V., *Electricity from microorganisms.* Microbiology, 2008. **77**(2): p. 123-131.

46. Klimes, A., et al., *Production of pilus-like filaments in Geobacter sulfurreducens in the absence of the type IV pilin protein PilA*. Fems Microbiology Letters, 2010. **310**(1): p. 62-68.

47. Craig, L., M.E. Pique, and J.A. Tainer, *Type IV pilus structure and bacterial pathogenicity.* Nat Rev Micro, 2004. **2**(5): p. 363-378.

48. Audette, G.F., et al., *DNA-Binding Protein Nanotubes: Learning from Nature's Nanotech Examples.* Nano Letters, 2004. **4**(10): p. 1897-1902.

49. Craig, L., et al., *Type IV pilin structure and assembly: X-ray and EM analyses of Vibrio cholerae toxin-coregulated pilus and Pseudomonas aeruginosa PAK pilin.* Molecular Cell, 2003. **11**(5): p. 1139-1150.

50. Szeto, T.H., A. Dessen, and V. Pelicic, *Structure/Function Analysis of Neisseria meningitidis PilW, a Conserved Protein That Plays Multiple Roles in Type IV Pilus Biology.* Infection and Immunity. **79**(8): p. 3028-3035.

51. Burrows, L.L., *Weapons of mass retraction.* Mol Microbiol, 2005. **57**(4): p. 878-88.

52. Reguera, G., R.M. Worden, and S.D. Kelly, *Elucidate mechanism of electron transfer of uranium mediated by Geobacter nanowires*. 2006, NIEHS: Michigan State University.

53. Boudard, S., et al., *Controlling the pathway of formation of supported lipid bilayers of DMPC by varying the sodium chloride concentration.* Thin Solid Films, 2006. **495**(1-2): p. 246-251.

54. Cornell, B.A., et al., *The lower limit to the size of small sonicated phospholipid vesicles.* Biochimica et Biophysica Acta (BBA) - Biomembranes, 1982. **690**(1): p. 15-19.

55. Woodbury, D.J., et al., *Reducing liposome size with ultrasound: Bimodal size distributions.* Journal of Liposome Research, 2006. **16**(1): p. 57-80.

56. DeWitt, L., et al., *Determination of ground- and excited-state isomerization barriers for the oligothiophene 3',4'-dibutyl-2,2':5',2''-terthiophene.* Journal of the American Chemical Society, 1993. **115**(25): p. 12158-12164.

57. DelaCruz, J.L. and G.J. Blanchard, *Understanding the Balance between Ionic and Dispersion Interactions in Aqueous Micellar Media.* The Journal of Physical Chemistry B, 2003. **107**(29): p. 7102-7108.

58. Gajraj, A. and R.Y. Ofoli, *Quantitative Technique for Investigating Macromolecular Adsorption and Interactions at the Liquid-Liquid Interface.* Langmuir, 2000. **16**(9): p. 4279-4285.

59. Smith, B.A. and H.M. McConnell, *Determination of molecular motion in membranes using periodic pattern photobleaching.* Proc Natl Acad Sci U S A, 1978. **75**(6): p. 2759-63.

60. Chen, Y., et al., *Methods to measure the lateral diffusion of membrane lipids and proteins.* Methods, 2006. **39**(2): p. 147-53.

61. Lanni, F. and B.R. Ware, *Modulation detection of fluorescence photobleaching recovery.* Review of Scientific Instruments, 1982. **53**(6): p. 905-908.

62. Sprague, B.L. and J.G. McNally, *FRAP analysis of binding: proper and fitting.* Trends Cell Biol, 2005. **15**(2): p. 84-91.

63. Kinosita, K., Jr., S. Kawato, and A. Ikegami, *A theory of fluorescence polarization decay in membranes.* Biophys J, 1977. **20**(3): p. 289-305.

64. Kreiter, M., et al., *Orientation dependence of fluorescence lifetimes near an interface.* The Journal of Chemical Physics, 2002. **117**(20): p. 9430-9433.

65. Steiner, R.F., *Fluorescence Anisotropy: Theory and Applications*, in *Topics in fluorescence spectroscopu*, J.R. Lakowicz, Editor. 1991, Plenum Press: New York, NY. p. 1-52.

66. Blanchard, G.J., *Picosecond spectroscopic measurement of a solvent dependent change of rotational diffusion rotor shape.* The Journal of Chemical Physics, 1987. **87**(12): p. 6802-6808.

67. Lipari, G. and A. Szabo, *Effect of vibrational motion on fluorescence depolarization and nuclear magnetic resonance relaxation in macromolecules and membranes.* Biophysical Journal, 1980. **30**(3): p. 489-506.

68. Lipari, G. and A. Szabo, *Effect of librational motion on fluorescence depolarization and nuclear magnetic resonance relaxation in macromolecules and membranes.* Biophysical Journal, 1980. **30**(3): p. 489-506.

69. Kinosita Jr, K., A. Ikegami, and S. Kawato, *On the wobbling-in-cone analysis of fluorescence anisotropy decay.* Biophysical Journal, 1982. **37**(2): p. 461-464.

70. Szabo, A., *Theory of fluorescence depolarization in macromolecules and membranes.* The Journal of Chemical Physics, 1984. **81**(1): p. 150-167.

71. Fery-Forgues, S., J.-P. Fayet, and A. Lopez, *Drastic changes in the fluorescence properties of NBD probes with the polarity of the medium: involvement of a TICT state?* Journal of Photochemistry and Photobiology A: Chemistry, 1993. **70**(3): p. 229-243.

72. Mazères, S., et al., *7-nitrobenz-2-oxa-1,3-diazole-4-yl-labeled phospholipids in lipid membranes: differences in fluorescence behavior.* Biophysical Journal, 1996. **71**(1): p. 327-335.

73. Greenough, K.P. and G.J. Blanchard, *Evaluating the Role of Chromophore Side Group Identity in Mediating Solution-Phase Rotational Motion.* The Journal of Physical Chemistry A, 2006. **111**(4): p. 558-566.

74. Starr, T.E. and N.L. Thompson, *Formation and characterization of planar phospholipid bilayers supported on TiO2 and SrTiO3 single crystals.* Langmuir, 2000. **16**(26): p. 10301-10308.

75. Starr, T.E. and N.L. Thompson, *Fluorescence pattern photobleaching recovery for samples with multi-component diffusion.* Biophysical Chemistry, 2002. **97**(1): p. 29-44.

76. Starr, T.E. and N.L. Thompson, *Fluorescence pattern photobleaching recovery for samples with multi-component diffusion.* Biophys Chem, 2002. **97**(1): p. 29-44.

77. Kasotakis, E., et al., *Design of metal-binding sites onto self-assembled peptide fibrils.* Biopolymers, 2009. **92**(3): p. 164-72.

78. Kumara, M.T., S. Muralidharan, and B.C. Tripp, *Generation and characterization of inorganic and organic nanotubes on bioengineered flagella of mesophilic bacteria.* J Nanosci Nanotechnol, 2007. **7**(7): p. 2260-72.

79. Audette, G.F., R.T. Irvin, and B. Hazes, *Purification, crystallization and preliminary diffraction studies of the Pseudomonas aeruginosa strain K122-4 monomeric pilin.* Acta Crystallogr D Biol Crystallogr, 2003. **59**(Pt 9): p. 1665-7.

80. Audette, G.F. and B. Hazes, *Development of protein nanotubes from a multi-purpose biological structure.* J Nanosci Nanotechnol, 2007. **7**(7): p. 2222-9.

81. Menzella, H.G., E.A. Ceccarelli, and H.C. Gramajo, *Novel escherichia coli strain allows efficient recombinant protein production using lactose as inducer.* Biotechnology and Bioengineering, 2003. **82**(7): p. 809-817.

82. Li, K., et al., *Fed-batch fermentor synthesis of 3-dehydroshikimic acid using recombinant Escherichia coli.* Biotechnology and Bioengineering, 1999. **64**(1): p. 61-73.

83. Wallace, B.A. and R.W. Janes, eds. *Modern technices for circular dichroism and synchrotron radiation circular dichroism spectroscopy*. Advances in Biomedical Spectroscopy, ed. P.I. H. 2009, IOS Press Amsterdam. 256.

84. Greenfield, N.J., *Using circular dichroism spectra to estimate protein secondary structure.* Nat. Protocols, 2007. **1**(6): p. 2876-2890.

85. Mihalyi, E., *Numerical values of the absorbances of the aromatic amino acids in acid, neutral, and alkaline solutions.* Journal of Chemical & Engineering Data, 1968. **13**(2): p. 179-182.

86. Veazey, J.P., *Scanning probe studies of the pilus nanowires in Geobacter sulfurreducens*, in *Physics*. 2011, Michigan State University: East Lansing. p. 149.

87. Kyte, J. and R.F. Doolittle, *A simple method for displaying the hydropathic character of a protein.* Journal of Molecular Biology, 1982. **157**(1): p. 105-132.

88. Malhotra, A., R.B. Richard, and P.D. Murray, *Chapter 16 Tagging for Protein Expression*, in *Methods in Enzymology*. 2009, Academic Press. p. 239-258.

89. Gentz, R., et al., *Association of degradation and secretion of three chimeric polypeptides in Escherichia coli.* J. Bacteriol., 1988. **170**(5): p. 2212-2220.

90. Fong, B.A., W.-Y. Wu, and D.W. Wood, *The potential role of self-cleaving purification tags in commercial-scale processes.* Trends in Biotechnology, 2010. **28**(5): p. 272-279.

91. Xu, M.-Q. and T.C. Evans Jr., *Purification of Recombinant Proteins from E. coli by Engineered Inteins*, in *E. coli Gene Expression Protocols*, P.E. Vaillancourt, Editor. 2003, Humana Press: Totowa, New Jersey. p. 43-68.

92. Switzer, R.L. and L.F. Garrity, *Experimental Biochemistry*. 3rd edition ed. 1999, New York, NY: W. H. Freeman and Company. 450.

93. Matsuo, K., H. Watanabe, and K. Gekko, *Improved sequence-based prediction of protein secondary structures by combining vacuum-ultraviolet circular dichroism spectroscopy with neural network.* Proteins: Structure, Function, and Bioinformatics, 2008. **73**(1): p. 104-112.

94. Davis, A.M., S.A. St-Gallay, and G.J. Kleywegt, *Limitations and lessons in the use of X-ray structural information in drug design.* Drug Discovery Today, 2008. **13**(19-20): p. 831-841.

95. Montserret, R., et al., *Involvement of Electrostatic Interactions in the Mechanism of Peptide Folding Induced by Sodium Dodecyl Sulfate Binding.* Biochemistry, 2000. **39**(29): p. 8362-8373.

96. Watts, T.H., D.G. Scraba, and W. Paranchych, *Formation of 9-nm filaments from pilin monomers obtained by octyl-glucoside dissociation of Pseudomonas aeruginosa pili.* Journal of Bacteriology, 1982. **151**(3): p. 1508-1513.

97. Hjelmeland, L.M., A. Chrambach, and B.J. William, *[16] Solubilization of functional membrane proteins*, in *Methods in Enzymology*. 1984, Academic Press. p. 305-318.

98. le Maire, M., P. Champeil, and J.V. Møller, *Interaction of membrane proteins and lipids with solubilizing detergents.* Biochimica et Biophysica Acta (BBA) - Biomembranes, 2000. **1508**(1-2): p. 86-111.

99. Whitmore, L. and B.A. Wallace, *DICHROWEB, an online server for protein secondary structure analyses from circular dichroism spectroscopic data.* Nucleic Acids Research, 2004. **32**(suppl 2): p. W668-W673.

100. Whitmore, L. and B.A. Wallace, *Protein secondary structure analyses from circular dichroism spectroscopy: Methods and reference databases.* Biopolymers, 2008. **89**(5): p. 392-400.

101. Provencher, S.W. and J. Gloeckner, *Estimation of globular protein secondary structure from circular dichroism.* Biochemistry, 1981. **20**(1): p. 33-37.

102. van Stokkum, I.H.M., et al., *Estimation of protein secondary structure and error analysis from circular dichroism spectra.* Analytical Biochemistry, 1990. **191**(1): p. 110-118.

103. Sreerama, N. and R.W. Woody, *Estimation of Protein Secondary Structure from Circular Dichroism Spectra: Comparison of CONTIN, SELCON, and CDSSTR Methods with an Expanded Reference Set.* Analytical Biochemistry, 2000. **287**(2): p. 252-260.

104. *Scanning tunneling microscopy and spectroscopy: theory, techniques and applications*, ed. D.A. Bonell. 2001, New Yoork: Wiley-VCH.

105. Chen, C.J., *Introduction to scanning tunneling microscopy*. 2nd ed. Oxford series in optical and imaging sciences. 2008, New York: Oxford University Press.

106. Howorka, S., *Rationally engineering natural protein assemblies in nanobiotechnology.* Current Opinion in Biotechnology, 2011. **22**(4): p. 485-491.

107. Honda, M. and et al., *Metal-molecular interface of sulfur-containing amino acid and thiophene on gold surface.* Journal of Physics: Conference Series, 2008. **100**(5): p. 052071.

108. Bard, A.J. and L.R. Faulkner, *Electrochemical Methods: Fundamentals and Applications*. 1st ed. 1980, New York: John Wiley & Sons, Inc.

109. Johannsmann, D., I. Reviakine, and R.P. Richter, *Dissipation in Films of Adsorbed Nanospheres Studied by Quartz Crystal Microbalance (QCM).* Analytical Chemistry, 2009. **81**(19): p. 8167-8176.

110. Kotarek, J.A., K.C. Johnson, and M.A. Moss, *Quartz crystal microbalance analysis of growth kinetics for aggregation intermediates of the amyloid-beta protein.* Analytical Biochemistry, 2008. **378**(1): p. 15-24.

111. Bradford, D.C., et al., *Surface-Enhanced Infrared Ellipsometry of Self-Assembled Undecanethiol and Dodecanethiol Monolayers on Disordered Gold Nanoisland Substrates.* The Journal of Physical Chemistry B, 2005. **109**(44): p. 20914-20922.

112. Manne, S., et al., *Direct Visualization of Surfactant Hemimicelles by Force Microscopy of the Electrical Double Layer.* Langmuir, 1994. **10**(12): p. 4409-4413.

113. Levchenko, A.A., et al., *Kinetics of Sodium Dodecyl Sulfate Adsorption on and Desorption from Self-Assembled Monolayers Measured by Surface Plasmon Resonance.* Langmuir, 2002. **18**(22): p. 8464-8471.

114. Sek, S., K. Swiatek, and A. Misicka, *Electrical Behavior of Molecular Junctions Incorporating Alpha-Helical Peptide.* The Journal of Physical Chemistry B, 2005. **109**(49): p. 23121-23124.

115. Wu, J.-C., et al., *Controlled growth of aligned alpha-helical-polypeptide brushes for tunable electrical conductivity.* Applied Physics Letters, 2011. **98**(13): p. 133304.